The Hong Kong Polytechnic University

Department of Computing

Online Multispectral Palmprint Recognition

GUO Zhenhua

A thesis submitted in partial fulfillment of the requirement for the Degree of Doctor of Philosophy

October 2009

CERTIFICATE OF ORIGINALITY

I hereby declare that this thesis is my own work and that, to the best of my knowledge and belief, it reproduces no material previously published or written, nor material that has been accepted for the award of any other degree of diploma, except where due acknowledgement has been made in the text.

_________________ (Signed)

GUO Zhenhua (Name of Student)

Abstract

Palmprint, as a new member of biometrics family, has attracted much of research attention in the past decade. Many different algorithms and systems have been proposed and built. Although, great success has been achieved in palmprint research, palmprint recognition could be further improved in two aspects: higher accuracy and robustness against spoof attack. Multispectral imaging, a method to collect a series of images by different spectra, is a good technique to address the issues mentioned above. In this thesis, different aspects of multispectral palmprint recognition were investigated and discussed.

First, the issues of multispectral palmprint recognition were addressed. A well developed and accurate multispectral palmprint prototype with high speed was proposed. There are four different kinds of illumination in the device developed, blue illumination, green illumination, red illumination, and near infrared illumination. The former three are the primary colors well known in visible spectrum, and they could compose other lights. A large multispectral palmprint database was built by this device. Multispectral palmprint recognition can be regarded as a kind of special multimodal biometrics and there are three popular schemes regarding multimodal fusion: image level, feature level and matching score level. In this thesis, the three levels of fusion were studied and compared. The shortcomings and advantages of each method make them applicable for different applications.

Then, a critical issue for palmprint recognition was studied. Illumination which is used to enhance the palmprint feature is a key component in palmprint recognition system design. Although there are some rules or guidances on the selection of cameras, light types, lens etc. There is no work systematically evaluating whether the white light source, which is the dominant light color in palmprint recognition, and which is the optimal light. Based on the multispectral palmprint image acquisition and additive color theory, seven kinds of palmprint images are acquired by red, green, blue, cyan, yellow, magenta and white lighting. The question which light is optimal for palmprint was studied empirically through three kinds of palmprint recognition algorithms.

After that, although a multispectral palmprint acquisition device was developed, the underlying design principles were not well studied. In general, more feature bands could provide more features and thus get higher accuracy. However, more feature bands may contain redundant information and require too much cost on computation. Thus, the

optimal number of feature bands in terms of accuracy and computation cost is a key issue in multispectral imaging. In this thesis, a feature band clustering algorithm was proposed to determine the optimal feature band number. After determining the number, an exhaustive searching could find the optimal combination.

Finally, CompCode, one of state-of-the-art algorithms for palmprint recognition was analyzed and used in this thesis. It is the first algorithm for extracting orientation information for palmprint image with good accuracy and less computation cost on matching. It is mainly composed of three parts: filter design, feature extraction and matching. Although some work has been done on proposing novel filters, little work has been done on feature extraction and matching. A novel feature extraction scheme, Binary Orientation Co-occurrence Vector, was proposed in this thesis. It showed robustness to rotation effect and got better results than CompCode did on public databases. There are two widely used distances for fast orientation feature comparison. They are SUM_XOR and OR_XOR. No one empirically analyzed which one is more appropriate for palmprint recognition, and their relationship is left open for analyzing. In this thesis, a unified distance measurement was proposed. There is one parameter to control the proposed distance, and SUM_XOR and OR_XOR are special cases of the proposed distance with suitable parameter value. It also empirically showed when a suitable parameter was selected, better accuracy could be achieved comparing with the two distances.

List of Publications

The following technical papers have been published or are currently under review based on the result generated from this work.

1. Zhenhua Guo, David Zhang, Lei Zhang, and Wangmeng Zuo, Palmprint Verification using Binary Orientation Co-occurrence Vector, *Pattern Recognition Letters*, vol. 30, no. 13, pp. 1219-1227, 2009.
2. David Zhang, Zhenhua Guo, Guangming Lu, Lei Zhang, and Wangmeng Zuo, An Online System of Multi-spectral Palmprint Verification, *IEEE Transactions on Instrumentation and Measurement*, vol. 59, no. 2, pp. 480-490, 2010.
3. Zhenhua Guo, Lei Zhang, and David Zhang, Rotation Invariant Texture Classification Using LBP Variance (LBPV) with Global Matching, *Pattern Recognition*, vol. 43, no. 3, pp. 706-719, 2010.
4. Zhenhua Guo, Wangmeng Zuo, Lei Zhang, and David Zhang, A Unified Distance Measurement for Orientation Coding in Palmprint Verification, *Neurocomputing*, vol. 73, no. 4-6, pp. 944-950, 2010.
5. Zhenhua Guo, Wangmeng Zuo, Lei Zhang, and David Zhang, Palmprint Verification Using Consistent Orientation Coding, *International Conference on Image Processing*, 2009.
6. Zhenhua Guo, Lei Zhang, and David Zhang, Rotation Invariant Texture Classification Using Binary Filter Response Pattern (BFRP), *International Conference on Computer Analysis of Images and Patterns*, pp. 1130-1137, 2009.
7. Zhenhua Guo, David Zhang, and Lei Zhang, Is White Light the Best Illumination for Palmprint Recognition, *International Conference on Computer Analysis of Images and Patterns*, pp. 50-57, 2009.
8. Dong Han, Zhenhua Guo, and David Zhang, Multispectral Palmprint Recognition using wavelet-based Image Fusion, *International Conference on Signal Processing*, pp. 2074-2077, 2008.
9. David Zhang, Zhenhua Guo, Guangming Lu, Lei Zhang, Yahui Liu, and Wangmeng Zuo, Online Joint Palmprint and Palmvein Verification, submitted to *Expert Systems with Applications*.
10. Zhenhua Guo, David Zhang, Lei Zhang, Wangmeng Zuo, and Guangming Lu, Empirical Study of Light Source Selection for Palmprint Recognition, submitted to *Pattern Recognition Letters*.

Acknowledgements

I would like to take this opportunity to express my sincere thanks to everyone who generously gave me their care and support.

Firstly, I would like to give special thanks to my supervisor, Prof. David Zhang. My Ph.D studies would have never been completed without his endless patient guidance and support throughout my several years of studies in Hong Kong. I learned a lot not only from our discussion, but also from his work attitude. The discussion with him contributed significantly to this work, many research ideas were generated or corrected after the discussion. His enthusiasm for research motivates us to improve our academic research and develop practical applications and systems.

Secondly, I would like to give many thanks to Dr. Lei Zhang, Dr. Jane You, Dr. Wangmeng Zuo, Dr. Guangming Lu, Dr. Jian Yang, Dr. Dacheng Tao, and Dr. Ajay Kumar. Especially, I would like to thank Dr. Zhang and Dr. Zuo for their constructive comments and helpful discussion.

Thridly, I would like to thanks to the examiners of my thesis, Prof. David Feng, Prof. Bir Bhanu, and Prof. Zhi-Qiang Liu. They provided many constructive suggestions and comments to improve the thesis.

Fourthly, I would like to thanks to my classmates and colleagues, Qijun Zhao, Xingzheng Wang, Qin Li, Nan Luo, Xiaofeng Qu, Li Liu, Feng Liu and Vivek. We share our knowledge, experience and happiness. I will miss the live life with them.

Finally, I would like to dedicate this work to my parents, and especially my wife. Their kindly support and encouragement help me overcome difficulties and problems. Without them, I can not finish my Ph. D study.

Table of Content

List of Figures

List of Tables

Chapter 1. Introduction

1.1 Introduction of Biometrics

Nowadays, traditional token or key based personal authentication could not meet some applications, especially high secure orientated ones. Automatic authentication using biometric characteristics as the substitution or complement technology is becoming more and more popular. It is the study of methods for uniquely recognizing humans based up one or more intrinsic physical or behavioral traits [111-112], including the extensively studied fingerprint, facial features, iris, speech, hand geometry, palmprint etc. Fig. 1.1 shows a typical framework of a biometric system.

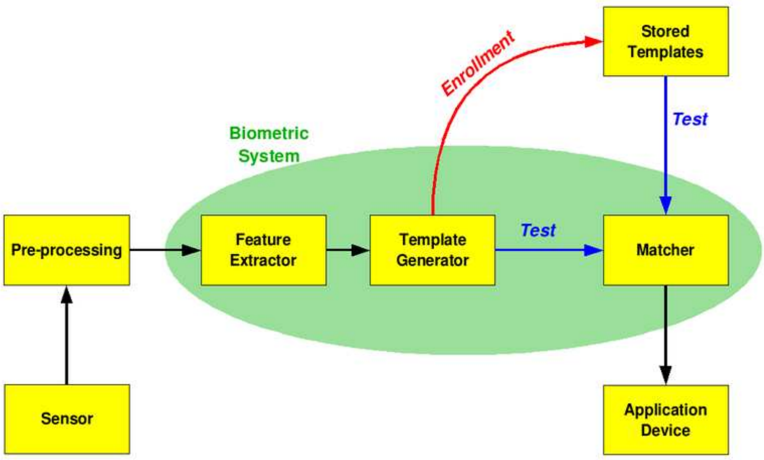

Figure 1.1 A typical framework of a biometric system. [115]

Among these traits, fingerprint has the longest history [113]. However some reasons such as age or the dryness of finger caused that around 2% of the population could not provide clear fingerprint images [114]. Iris is a popular and reliable trait [50], but its devices are more expensive, and some persons are reluctant to accept it because of worrying potential damage to their eyes. Other features, such as the face [116], voice [117] and hand geometry [118] are as yet not sufficiently accurate.

Compared with other features, palmprint has many advantages. It is composed of three kinds of features [12]: principal lines (usually three dominant lines on the palm), wrinkles (weaker than principal and more irregular lines) and minutia (ridge and valley which are similar to fingerprint). The principal and wrinkle could be captured under low resolution, for example <100dpi, so the on-line palmprint authentication could utilize CCD camera as the input sensor which makes the device much cheaper. Meanwhile, palmprint capture device is more user friendly than iris devices. Fig. 1.2 shows the comparison among various biometric traits.

Biometric identifier	Universality	Distinctiveness	Permanence	Collectability	Performance	Acceptability	Circumvention
DNA	H	H	H	L	H	L	L
Ear	M	M	H	M	M	H	M
Face	H	L	M	H	L	H	H
Facial thermogram	H	H	L	H	M	H	L
Fingerprint	M	H	H	M	H	M	M
Gait	M	L	L	H	L	H	M
Hand geometry	M	M	M	H	M	M	M
Hand vein	M	M	M	M	M	M	L
Iris	H	H	H	M	H	L	L
Keystroke	L	L	L	M	L	M	M
Odor	H	H	H	L	L	M	L
Palmprint	M	H	H	M	H	M	M
Retina	H	H	M	L	H	L	L
Signature	L	L	L	H	L	H	H
Voice	M	L	L	M	L	H	H

Figure 1.2 Comparison of various biometrics traits. (High, Medium and Low are denoted by H, M and L) [119]

1.2 Motivation and Summary of the Work

Great breakthrough has been made in palmprint recognition in the past decade, many systems and methods have been proposed. However, the accuracy is limited in some cases as the palmprint feature may be similar for a given spectral illumination. Furthermore, it is not difficult to fake a palmprint image [86]. Although 3-D imaging could be used to address these issues, the expensive and bulky device makes it difficult to be applied for real applications [100-102]. One solution to these problems can be multispectral imaging, which captures an image in a variety of spectral bands. Each spectral band highlights specific features of the palm, making it possible to collect more information to improve the accuracy and anti-spoofing capability of palmprint systems. This thesis investigated different aspects of multispectral palmprint recognitions, including system design and recognition methods.

There is no public available multispectral palmprint image acquisition device. A specially designed multispectral palmprint scanner was proposed. It could collect palmprint images in visible (blue, green and red) and near infrared spectra in a very short time. Constructing a semi-closed environment and using several pegs to control the position, high quality multispectral palmprint images could be acquired. Based on this device, a large multispectral palmprint database was built. Regarding multispectral palmprint as a special multimodal, different fusion techniques, image level, feature level and matching score level, were investigated and discussed. Their cons and pros were compared empirically.

Different palmprint systems were proposed in the past, among them, using active illumination to enhance the palmprint feature was a popular one. Although all of them use white light as the illumination source, there is no work systematically evaluating whether white light color illumination is the optimal choice for palmprint recognition. To address this issue, using the proposed multispectral palmprint acquisition device and additive color theory, seven kinds of palmprint images were collected by different simulated colors, blue, green, red, cyan, yellow, magenta, and white. To get unbiased results, three popular palmprint recognition methods were chosen and tested on many different kinds of settings. The experimental results show that white color may not be the optimal color, while yellow or magenta may be more appropriate for palmprint recognition.

Although multispectral palmprint recognition is not a new topic and several multispectral palmprint systems have been proposed. The question how to select feature bands for the system design has not been addressed. The random selection will cumber the wide acceptance of multispectral palmprint recognition. Here, a hyperspectral palmprint collecting environment is set up and a large hyperspectral palmprint database was built to address this issue. The hyperspectral cube includes 69 palmprint images from 420nm to 1100nm with 10 nm interval. A modified mean cluster algorithm was proposed to find the optimal number of feature bands. 3 distinctive clusters was discovered in our data and it was empirically validated that 3 bands may be enough for multispectral palmprint recognition.

In addition to using well developed palmprint recognition methods on multispectral palmprint recognition, the improvement of traditional palmprint recognition[*] is also important. Competitive Code (CompCode), one of the state-of-the-art algorithms on traditional palmprint recognition, was utilized in this thesis. Thus, if CompCode is improved, better performance on multispectral palmprint recognition could be obtained. After investigating the framework of CompCode, a new feature extraction and a unified distance measurement were proposed. Using the same filter, the proposed feature extraction, Binary Orientation Co-occurrence Vector (BOCV), could get better result and is more robust to rotation effect than CompCode. A unified distance measurement was

[*] In this thesis, traditional palmprint recognition represents the palmprint recognition by 2D image and unispectral lighting.

proposed to combine two widely used distances, SUM_XOR and OR_XOR, for fast feature comparison. There is one parameter to control the proposed distance, and SUM_XOR and OR_XOR are special cases of the proposed distance with suitable parameter value. Experimental results showed that better accuracy could be achieved compared with the two distances, if the parameter is selected suitably.

1.3 Organization of the Thesis

The following of the thesis is organized as follows. Chapter 2 reviews different aspects of palmprint recognition and several novel directions of palmprint recognition, including multispectral palmprint recognition, fusion, 3D palmprint, system protection and acceleration of identification. Chapter 3 presents the proposed multispectral palmprint acquisition device and investigates different fusion schemes: image level, feature level and matching score level, for online recognition. Chapter 4 empirically studies the light source for traditional palmprint recognition using the designed multispectral palmprint device. Chapter 5 investigates the feature band selection for multispectral palmprint recognition based one a self collected hyperspectral palmprint database. Chapter 6 discusses the improvement of traditional (unispectral) palmprint recognition from two aspects, a novel feature extraction and a unified distance. Fig. 1.3 shows the illustration of the organization.

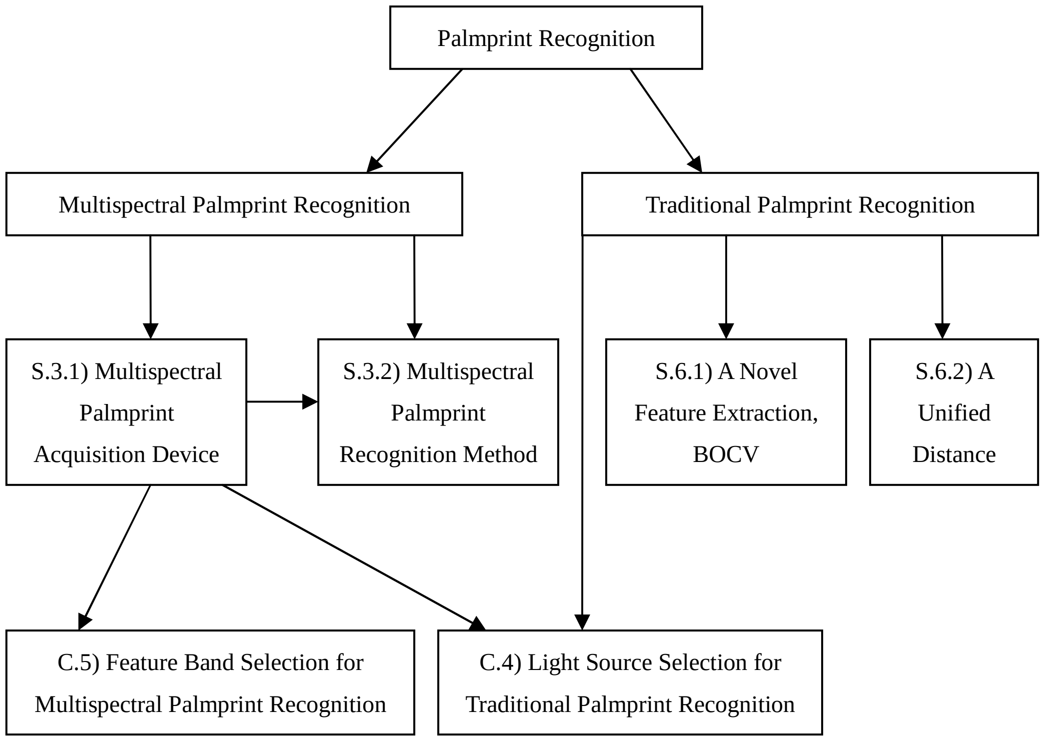

Figure 1.3 The organization of the thesis. (The links show the relationship between chapters or sections. S stands for Section while C represents Chapter.)

1.4 Palmprint Database to Be Used in the Thesis

In this study, six different kinds of palmprint database were used to test the system accuracy or algorithm performance.

1.4.1 PolyU Multispectral Palmprint Database (PUMPD)

A large multispectral palmprint images from 250 individuals using the developed multispectral acquisition device (described in Section 3.1) was collected. The subjects were mainly volunteers from our institute. In the database, 195 people are male and the age distribution is from 20 to 60 years old. We collected the multispectral palmprint images on two separate sessions. The average time interval between the two occasions is 9 days. On each session, the subject was asked to provide 6 samples of each of his/her left and right palms. So the database contains 6,000 images for each band from 500 different palms. For each shot, the device collected 4 images from the four bands (Red, Green, Blue and NIR) in less than one second. In palmprint acquisition, the users are asked to keep their palms stable on the device. The resolution of the images is 352 by 288 (<100 dpi).

1.4.2 PolyU Multispectral Motion Blur Palmprint Database (PUMMBPD)

The PUMPD was acquired under supervision. The image quality is controlled and good. However, in real applications, the supervision may not exist, and some users may not familiar with the system, so motion blur may occur during image acquisition. This may cause some poor quality images. A new database which is used to investigate motion blur effect was built. 1000 images were randomly selected from each feature band. Then these images were converted to simulated motion blur images by the described method (described in Section 3.2). Finally, these images were put to the original database to replace the original images.

1.4.3 PolyU Additive Color Palmprint Database (PUACPD)

We collected multispectral palmprint images from 250 subjects using the developed data acquisition device (described in Section 3.1). The subjects were mainly volunteers from our institutes. In the database, 195 subjects are male and the age distribution is from 20 to 60 years old. We collected the multispectral palmprint images on two separate sessions. The average time interval between the two occasions is 9 days. On each session, the subject was asked to provide 6 samples of each of his/her left and right palms. So our database contains 6,000 images for each band from 500 different palms. For each shot, the device collected 7 images from different bands (red, green, blue, cyan, yellow, magenta, and white) in less than two seconds. In palmprint acquisition, the users are asked to keep their palms stable on the device. The resolution of the images is 352*288 (<100 DPI).

1.4.4 PolyU Hyperspectral Palmprint Database (PUHPD)

A large hyperpsectral palmprint cube from 190 individuals using the developed data acquisition system (described in Section 5.1) is built. The subjects were mainly volunteers from our institute. In the database, the age distribution is from 20 to 60 years old. The multispectral palmprint cubes were collected by two separate sessions. The average time interval between the two occasions is around 1 month. On each session, the subject was asked to provide around 7 cubes of each of his/her left and right palms. So the database contains 5,240 images for each band from 380 different palms. Among them, 2608 cubes were collected by the first session, while 2632 by the second session.

1.4.5 PolyU Palmprint Database (PUPD)

The public database includes 7752 palmprint images from 193 individuals [127]. The database is collected in two sessions. Each time, the subject was asked to collect around 10 palmprint images from his left and right palms. Altogether, each person provided around 40 images. The average time interval between the two sessions is 69 days.

1.4.6 CASIA Palmprint Database (CASIAPD)

The public database contains 5,239 palmprint images from 301 individuals [146]. To the best of our knowledge, this database is the largest public available database in terms of the number of subjects. Most of the samples were collected in one session only. The subject was asked to provide about 8 palmprint images from his/her left and right palms.

1.5 Introduction of CompCode

CompCode, one of the state-of-the-art palmprint verification algorithms, is widely used in the thesis. It is a kind of texture-based coding, which extracts an orientation feature for each pixel. It owns many advantages, such as robust to illumination and fast for matching, thus it is more suitable for online system.

By viewing the line features in palmprint images as dark lines, we apply six Gabor filters along different directions ($\theta_j = j\pi/6$, where j={0,1,2,3,4,5}) to the palmprint images for orientation feature extraction. For each pixel, the orientation corresponding to the minimal response is taken as the feature at this pixel [52]. The employed Gabor filter is as:

$$\psi(x,y,\omega,\theta)=\frac{\omega}{\sqrt{2\pi\kappa}}e^{-\frac{\omega^2}{8\kappa^2}(4x'^2+y'^2)}\left(e^{i\omega x'}-e^{-\frac{\kappa^2}{2}}\right) \tag{1-1}$$

where $x'=(x-x_0)\cos\theta+(y-y_0)\sin\theta, y'=-(x-x_0)\sin\theta+(y-y_0)\cos\theta$, ($x_0, y_0$) is the center of the function, ω is the radial frequency in radians per unit length, θ is the orientation of the Gabor functions in radians, $\kappa=\sqrt{2\ln 2}\left(\frac{2^\phi+1}{2^\phi-1}\right)$ and ϕ is the half-amplitude bandwidth of the frequency response. To reduce the influence of illumination, the DC (direct current) is removed from the filter.

Table 1.1 Bit Representation of the Orientation Coding.

Orientation Value	Bit 0	Bit 1	Bit 2
0	0	0	0
π/6	0	0	1
π/3	0	1	1
π/2	1	1	1
2π/3	1	1	0
5π/6	1	0	0

Since there are totally 6 different orientations, we can code them by using 3 bits as listed in Table 1.1. This coding scheme is to make the bit-wise difference proportional to the angular difference [52]. So the difference between two orientation maps could be measured by using the bitwise Hamming distance:

$$D(P,Q)=\frac{\sum_{y=1}^{M}\sum_{x=1}^{N}\sum_{i=1}^{3}(P_i^b(x,y)\otimes Q_i^b(x,y))}{3*M*N} \tag{1-2}$$

where *P* and *Q* represent two palmprint orientation feature maps, P_i^b and Q_i^b are the i^{th} bit plane of *P* and *Q*, respectively. Symbol "$\otimes$" represents bitwise exclusive OR.

Obviously, D is between 0 and 1, and for a perfect matching the distance will be 0. The feature map is down-sampled from 128*128 to 32*32 [103].

Chapter 2. Literature Review

In this chapter, the general concepts and methods of palmprint recognition is introduced first. Then, some palmprint recognition methods and systems are introduced. The research and analysis of multispectral palmprint, a new direction of palmprint recognition, are reviewed. Finally, other directions of palmprint recognition are discussed and compared.

2.1 Introduction of Palmprint Recognition

2.1.1 Introduction of Palmprint

A palm is defined as the inner surface of a hand between the wrist and the root of fingers [1]. It is rich in features: principal lines, winkles, ridges, singular points and minutiae points, as shown in Fig. 2.1, make up the palmprint. The area of it is much larger than a finger tip, but is covered with the same kind of skin.

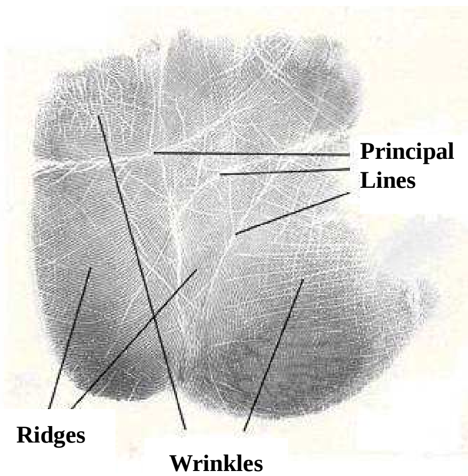

Figure 2.1 Typical Features from Palmprint. [1]

The main features of palmprint, including principal lines and wrinkles, are formed between 3 and 5 months after conception, and the other features appear after birth [2]. There is a long history of palmistry, using palm lines for fortune telling [3]. In palmistry, different lines are defined for different functions as shown in Fig. 2.2. It is also found that palmprint is related with human diseases [4].

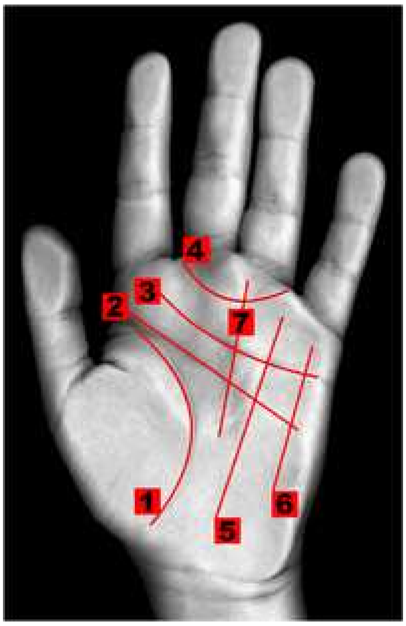

Figure 2.2 Some of the lines of the hand in Palmistry. 1: Life line - 2: Head line - 3: Heart line - 4: Girdle of Venus - 5: Sun line - 6: Mercury line - 7: Fate line. [3]

From the acquisition point of view, there are mainly two types of palmprint recognition, offline and online.

2.1.2 Offline Palmprint Recognition

In the early stage, due to the limitation of digital image acquisition, researchers could not get palmprint images instantly and their work focused on offline images only [5-7, 38]. They had to put their palms on a paper with ink, then the inked paper was digitalized by a scanner. Usually, the image quality is good and the resolution is high. However, because of the shape of palm, part of palmprint feature, especially the central part, is missed as shown in Fig. 2.3. Furthermore, its acquisition time is much longer and is more suitable for forensic applications, not for civil and commercial applications.

Figure 2.3 An offline palmprint image. [7]

2.1.3 Online Palmprint Recognition

There are two types of palmprint images, high resolution and low resolution. High resolution palmprint images (usually above 500 dpi to meet the requirement of NIST [8]) could provide clear minutia features which are exclusively collected by high resolution imaging. These minutia features are very important for forensic applications [9-11]. Because of the large area, the computation cost of high resolution image is high. The high computation make high resolution palmprint recognition fail to meet the requirement of many civil and commercial applications.

As low resolution (usually below 100 dpi [12]) could contain most of lines of palm and texture information, the discriminant information is enough for most of civil and commercial applications such as access control and time attendance. In this thesis, low resolution palmprint recognition is the main focus.

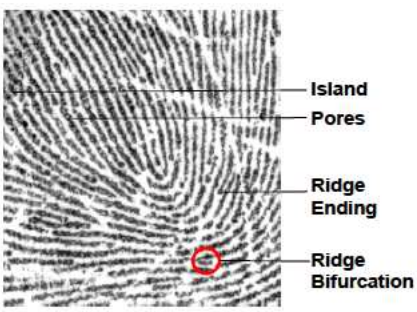

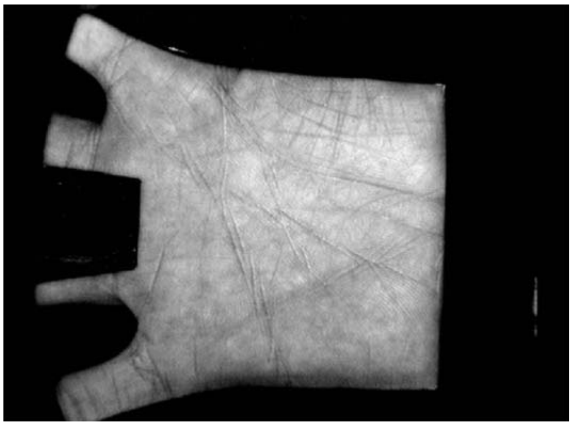

(a) (b)

Figure 2.4 High resolution vs low resolution palmprint images. a) High resolution palmprint image [10]; b) low resolution palmprint image [12].

2.2 Review of Palmprint Recognition

For an online palmprint recognition system, it is mainly composed of four parts: acquisition device, Region of Interest (ROI) extraction, feature extraction and matching. This section discusses the research results of each part.

2.2.1 Palmprint Image Acquisition Device

According to the types of sensors, there are mainly four kinds of devices [13]: digital scanners [14-21], video cameras [22-24], CCD (Charge Coupled Device) based palmprint scanner [12, 25-26] and digital cameras [27-31].

It is easier and convenient to get palmprint images by digital scanner with different image resolution. The scanner does not require any consideration of light source, lens and focus issues. But it suffers two main disadvantages during collection. First, the speed is usually slow. It requires warm-up procedure and may take several seconds to collect the palmprint. Second, during collections, the user is asked to put his/her palm wholly on the scanner, so it may bring sanitary issues. Fig. 2.5a shows a typical palmprint image by a scanner.

Digital cameras could get good quality of palmprint images. It could quickly get a palmprint image without the worry of hygienic problems. Although it could get online palmprint image, to my best knowledge, no one developed an online palmprint recognition system using digital cameras. Probably because it is difficult to control the digital camera with a computer, thus it requires human intervention for data collection which limits its applications. Fig. 2.5b shows a typical palmprint image by a digital camera.

CCD based palmprint scanner is a specifically designed device for data collection. The image quality is very high and the central part of palm is collect by touchless way usually. The image is collected by a semi-closed environment usually. There are many issues to be addressed during device design, such as illumination shape, lens and A/D converter [32]. Fig. 2.4b shows a typical palmprint image by a CCD based scanner.

Video camera, usually web camera, draws attention recently. Web cameras and embedded camera are becoming more and more popular. The cost of camera is usually low and it is much easier to collect palmprint images. Furthermore, it is easy to design a wholly touchless system. The only drawback is the camera may not provide very high quality image as the signal-to-noise ratio is relative low. Fig. 2.5c shows a typical palmprint image by a web camera.

(a) [14] (b) [28] (c) [24]

Figure 2.5 Palmprint images by different devices. (a) a palmprint image by scanner; (b) a palmprint image by digital camera; (c) a palmprint image by web camera.

2.2.2 ROI Extraction

After getting palmprint images, it is necessary to crop part of palm for feature extraction and matching. It is because of two reasons. First, the area of processing is reduced. For example, Zhang et al. extracted a 128*128 region from a 384*284 image [12]. The computation and storage cost could be reduced by using ROI only. Second, the palm position is aligned. It is difficult, even impossible, to put a user’s palm on the same position. Thus rotation, translation and scale variation may occur during data collection. Some works were proposed to use a fixed area [31] or ROI free method [27], but it required long time for recognition or failed to get higher accuracy. The most popular method detects some key points in the image, then sets a coordinate from these key points and finally extract a rectangle region from the original image. There are different methods on detecting key points including tangent line [12], wavelet analysis [17], bisector method [34], middle of fingers [25], valley line [16], and maximal rectangle [28], etc. Other ROI extraction methods include extracting a circular region [35, 48] and elliptical regions [36]. Fig. 2.6 shows an illustration of ROI extraction. Usually, the ROI is extracted from one single image. Han et al. [23] proposed to use one extra camera to address the ROI issue in uncontrolled scene. Two images are collected by two cameras simultaneously, one for ROI extraction only and the other for recognition.

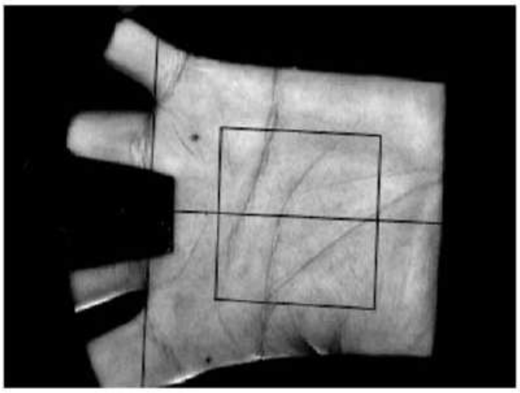

(a) (b)

Figure 2.6 An illustration of ROI extraction. (a) Coordinate built by tangent line; (b) extracted region. [12]

2.2.3 Feature Extraction

Before feature extraction, to remove intensity variation, normalization methods could be chosen such as histogram equalization [37], and a pre-specified mean and standard deviation [28]. There are four kinds of popular methods for feature extraction, line detection, coding schemes, subspace learning, and statistical method. And there are some methods which are difficult to be classified to any groups.

2.2.3.1 Line Detection

Palm lines are most apparent features in images. Thus, it is very intuitive to detect palm lines and use the extracted feature for recognition. At the early stage, some well known line detection operators were applied on palmprint images directly, such as Sobel operator [14, 17-18, 30, 34] and Canny operator [39]. After that, many modified operators or specific designed operators were proposed, including first-order and second-order derivative of Gaussian function [40, 43], line-based Hough transform [41], Steerable filter [42], modified finite Radon transform [44], wide line detector [45-47] and self designed directional structure [49]. Fig. 2.7 shows an example of line detection. However, line detection method may lose some information of palmprint and itself is still an open issue in image processing.

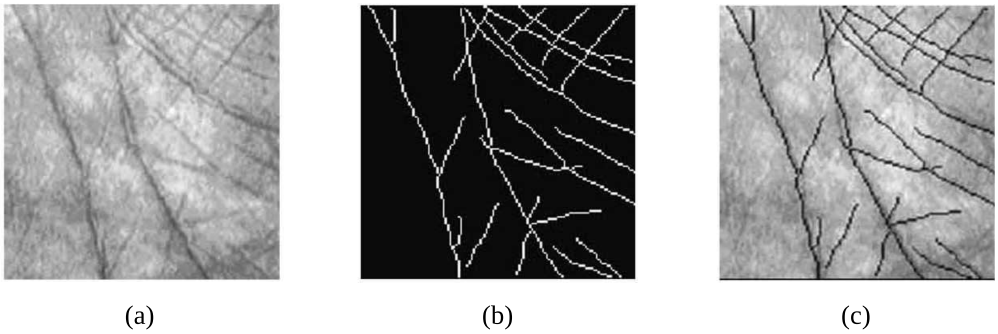

Figure 2.7 An example of line detection [40]. (a) Original image; (b) Detected lines. (c) Original image overlapped with the extracted lines.

2.2.3.2 Coding Scheme

Regarded palmprint image as a texture image and derived from successful IrisCode [50], Palmprint Code (PalmCode) [12] is the first coding scheme encoded Gabor phase information. Then an improved version, Fusion Code (Fusion Code) [51] was proposed to reduce the similar streak effect. Competitive Code (CompCode) [52] was the first algorithm to encode orientation feature for palmprint image. After the success of CompCode, several orientation based coding schemes have been proposed such as Palmprint Orientation Code (POC) [53], Robust Line Orientation Code (RLOC) [23, 31, 54]. Recently, other codes schemes, including Orthogonal Line Ordinal Features (OLOF) [55], derivative of Gaussian code (DoGCode) [57] and Binary Orientation Co-occurrence Vector (BOCV) [56], were proposed. Fig. 2.8 shows an example of extracted codes. Because coding scheme could utilize all information of palmprint image and can compare different features in a short time, it is suitable for identification in large databases [13].

Figure 2.8 An example of code. (a) Original Image; (b) CompCode Feature (different gray level represent different orientation). [52]

2.2.3.3 Subspace Learning

Taking palmprint images as a high dimensional vector or a 2D matrix, many different subspace learning methods have been applied on palmprint recognition. Some works applied classical or new developed subspace learning algorithms, such as principal component analysis (PCA) [15, 16, 37, 58, 64, 70, 74], linear discriminant analysis

(LDA) [59], independent component analysis (ICA) [60, 65], locality preserving projection (LPP) [21, 61], unsupervised discriminant projection (UDP) [62] and discriminant projection embedding (DPE) [63], on palmprint images directly. Other works applied subspace learning algorithms on filtered images or feature maps instead of original images, such as Gabor+PCA [20, 67, 69, 73], Gabor+LDA [66], Gabor+discriminative common vectors (DCV) [68], principal lines+LPP [71], line profile+PCA [25], and RLOC+LPP[72]. Fig. 2.9 shows an example of extracted feature by PCA.

(a) (b)

Figure 2.9 An example of extracted feature. (a) Original Image; (b) Eigenpalm. [58]

2.2.3.4 Statistical Method

There are mainly two kinds of statistical methods, local and global statistical approaches. For local statistical methods, a palmprint image is divided into many overlapped or non-overlapped regions and statistical values are extracted from each region. The local statistical methods include mean and/or standard value of original images or filtered images [28, 35, 75, 81, 82], energy features [33], and Local Binary Pattern (LBP) histogram [19, 22, 76]. The idea of global statistical methods is similar with local statistical methods, but features are extracted from the whole image, such as moment [48, 78-79] and gravity center [77]. Fig. 2.10 shows an example of extracting statistical features.

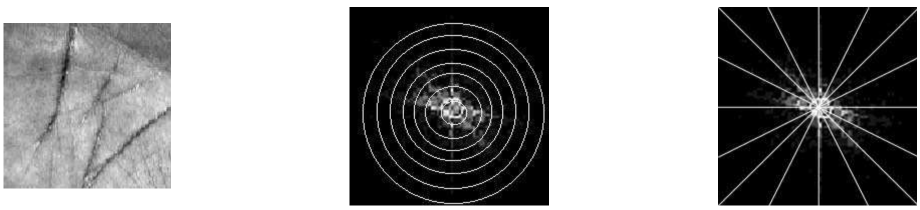

(a) (b) (c)

Figure 2.10 An example of extracting statistical features. (a) Original Image; (b) Fourier transform partition by radius; (c) Fourier transform partition by angle. (Energy feature are computed from different regions.) [33]

2.2.3.5 Other Methods

There are some methods difficult to be classified into previous mentioned methods [24, 27, 29, 80, 83]. For example, Doublet et al. proposed to decompose and estimate a grayscale distribution from the image [24]. Su generated characteristic matrix using ring rotation invariant transform [29]. Hennings-Yeomans et al. designed correlation filter for palmprint recognition [80]. Ito et al. applied phase-based correlation to compute the similarity of two images [83]. Zhang et al. proposed to use complex wavelet for palmprint image matching [120]. The method was derived from image similarity structure [121-122] and can get good results even with small translation, rotation and scale variation. Wu et al. built feature vectors from centroid coordinates of different regions, as illustrated in Fig. 2.11 [27].

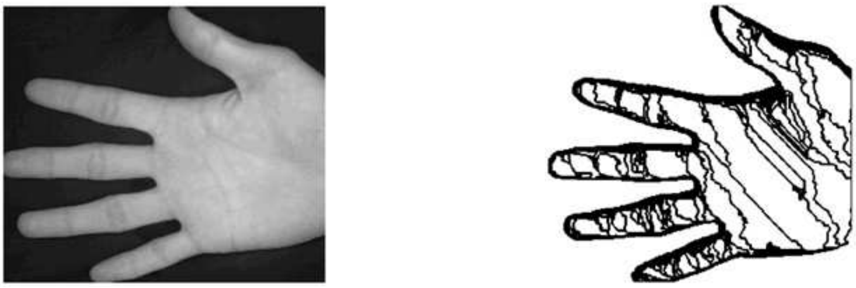

(a) (b)

Figure 2.11 An image with its segmentation. (a) Original image; (b) The segmentation of (a). [27]

2.2.4 Feature Matching

Feature matching is usually related with feature extraction, for example, Hamming distance is commonly used for coding scheme and Euclidean distance is widely utilized for subspace learning. Many advanced classification technique, such as neural network [17, 63], support vector machine (SVM) [24], hidden Markov model [34] and correlation filter [80], have been applied on palmprint matching. And many different dissimilarity measurements with simple nearest neighborhood classifiers, such as Euclidean distance [58-59], Hamming distance [12, 54-57], correlation [83] and cosine distance [16], have been tested on palmprint features. Compared with feature extraction, fewer researches explored new distances or classifiers [37, 84]. Yu and Leung proposed a curve segment Hausdorff distance to measure line edge map. Zuo et al. [37] developed a new distance metric for image matching.

2.3 Review of Multispectral Palmprint Recognition

Although great successes have been achieved for palmprint recognition, there is room for improvement of online palmprint recognition, particularly in the area of accuracy and its vulnerability to spoof attacks [86]. In palmprint, each spectral image will highlight a different feature of the palm, making it possible to collect more information to improve the accuracy [87-89, 152-153]. The correlations between different spectra [89] can then be used for anti-spoof measures. Multispectral imaging has shown its superiority in many biometric researches, such as face recognition [88, 153, 162-167], iris recognition [152, 89] and fingerprint recognition [87, 168-169].

Multispectral analysis has been used in palm related authentication [26, 90-93]. Rowe et al. [90] proposed a multispectral whole-hand biometric system. The object of this system was to collect palmprint information with clear fingerprint features and the imaging resolution was set to 500dpi. However, the low speed of feature extraction and feature matching makes it unsuitable for real-time applications. Likforman-Sulem et al. [91] used multispectral images in a multimodal authentication system; however, their system used an optical desktop scanner and a thermal camera which make the system very costly. The imaging resolution is also too high (600dpi, the FBI fingerprint standard) to meet the real-time requirement in practical biometric systems. Wang et al. [26] proposed a palmprint and palm vein fusion system, which could acquire two kinds of images simultaneously. The system uses one color camera and one near infrared camera and requires a registration procedure of about 9 seconds. Hao et al. [92-93] developed a contact-free multispectral palm sensor. However, the image quality is limited and hence the recognition accuracy is not very high. Overall, multispectral palmprint scanning is a relatively new topic and the works mentioned above stand for the state-of-the-art work. And, to our best knowledge, how to select the feature bands is not addressed yet.

2.4 Review of Other Directions of Palmprint Recognition

To improve the system accuracy and enhance the anti-spoof ability, except multispectral palmprint, some works on fusion and 3D palmprint recognition have been proposed and will be discussed in the following section. After that, other issues, besides accuracy and anti-spoof, need to be addressed for system implementation, for example, how to protect privacy, templates and communication, are reviewed. Finally, how to accelerate palmprint matching in large scale identification are surveyed.

2.4.1 Fusion

Fusion is a good way to increase the system accuracy and robustness [94]. Generally speaking, there are two kinds of fusion. The first kind is fusion of multiple features [18-19, 75] from one palmprint image. As the different features from the same image are correlated, the improvement will be limited [95]. The other kind is multimodal, fusion of palmprint with other biometrics traits [15, 28, 35, 67-68, 74, 81, 96]. In the past decade, many different multimodal systems have been proposed, including, finger surface+palmprint [15], hand geometry+palmprint [28, 35, 81], face+palmprint [67, 68], fingerprint+palmprint [74], and iris+palmprint [96].

2.4.2 3D Palmprint Recognition

3D information is robust to illumination change and it is difficult to fake a high resolution 3D object, so 3D biometrics has been studied for face [97], ear [98] and finger biometrics [99]. Recently, Zhang et al. proposed to acquire 3D palmprint information by a structure light method for personal authentication [100-102, 131]. Fig. 2.12 shows an example of 3D palmprint.

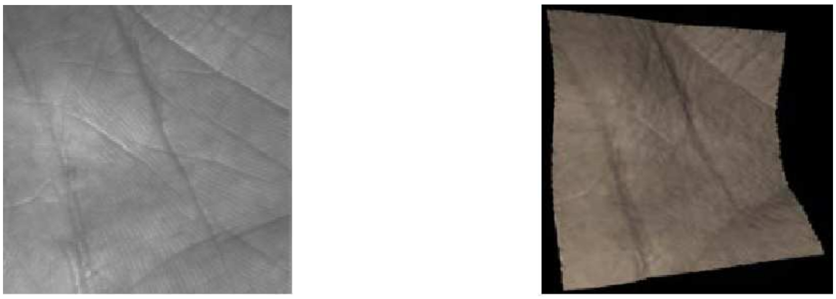

(a) (b)

Figure 2.12 Partial of palm. (a) 2D; (b) 3D. [100]

2.4.3 System Protection

As shown in Fig. 2.13, a biometric system is vulnerable to different attacks. Kong et al. analyzed the vulnerable points and proposed corresponding measurements to replay attacks, database attacks [103]. Kong et al. analyzed the success probability of brute-force attack [105]. Palmprint template re-issuance has been analyzed and discussed [103-104, 106]. Palmprints could also be used for cryptosystem [107-108]. Compared with palmprint feature extraction and matching, the research on system protection is less.

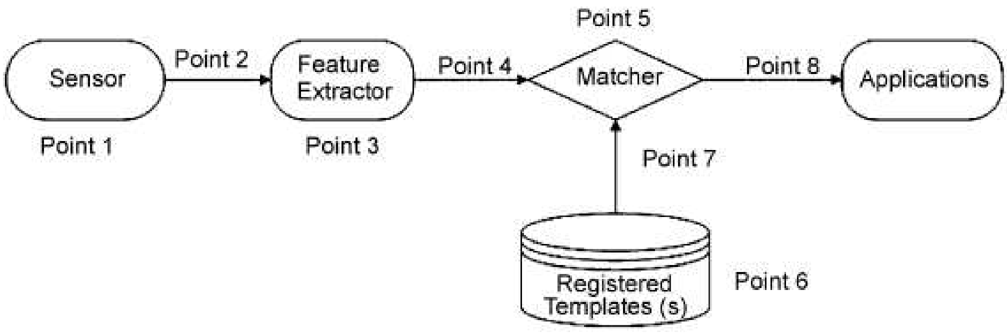

Figure 2.13 Vulnerable points in a typical biometric system. [103]

2.4.4 Acceleration of Identification

There are usually two ways, hierarchies and palmprint classification, to speed up to find a similar palmprint in a large scale database. Hierarchical methods first find a subset from a large database. Then further findings are implemented on the selected candidates only [14, 27, 41, 85]. Fig. 2.14 illustrates an example of hierarchical search scheme.

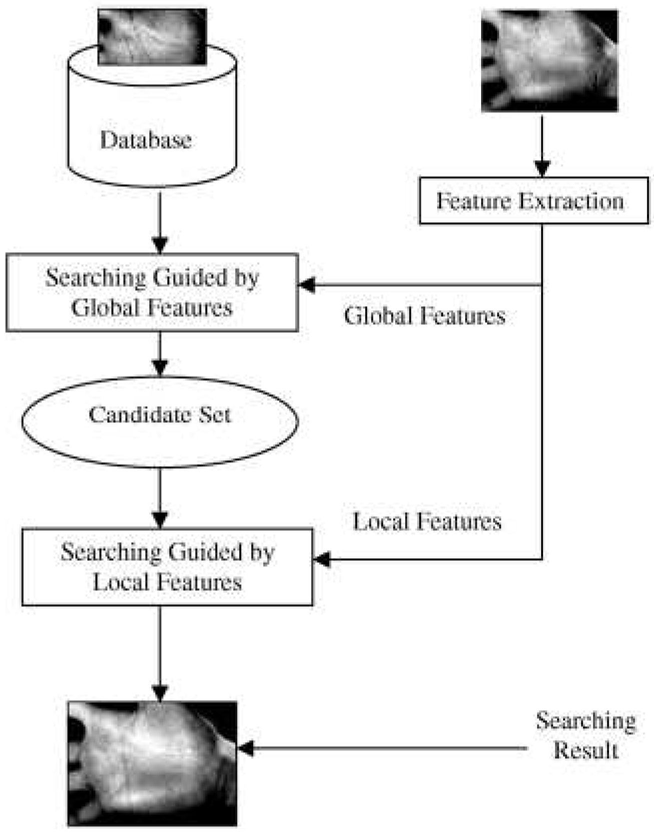

Figure 2.14 Process of hierarchical search scheme. [85]

However, there is a balance between accuracy and speed; selecting a small subset in the first step can get quick responses but may fail to find the correct sample, while selecting too many candidates could not improve the searching speed. Wu [109] proposed six classes of palmprint images according to the principal lines. Fig. 2.15

shows the six classes of palmprint defined by Wu. However, the partition is unbalanced. For example, more than 78% samples belong to one class (Fig. 2.15e), which attenuates the advantage of classification. So a further classification is needed to break the unbalanced situation [110].

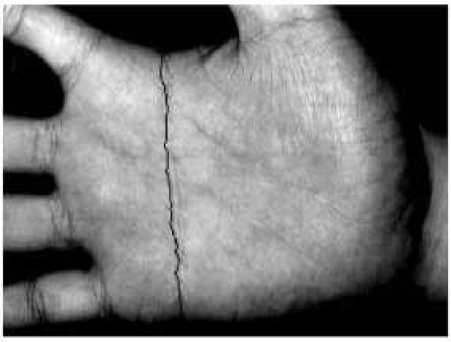

(a) Category 1

(b) Category 2

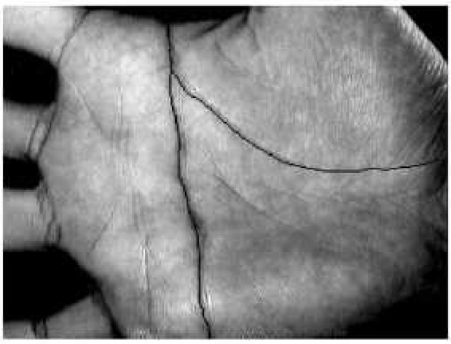

(c) Category 3

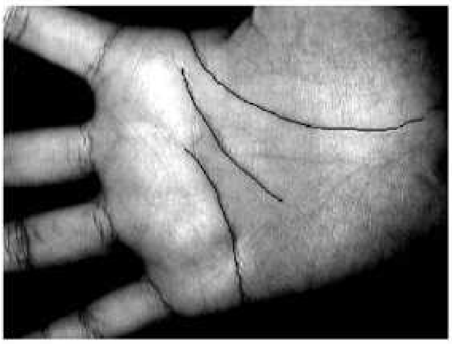

(d) Category 4

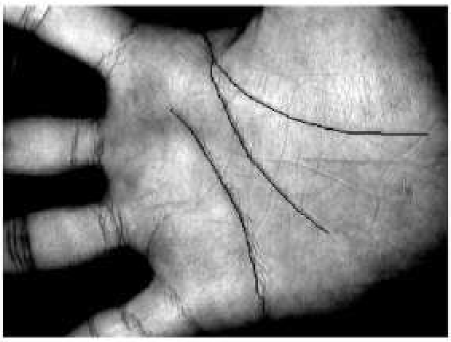

(e) Category 5

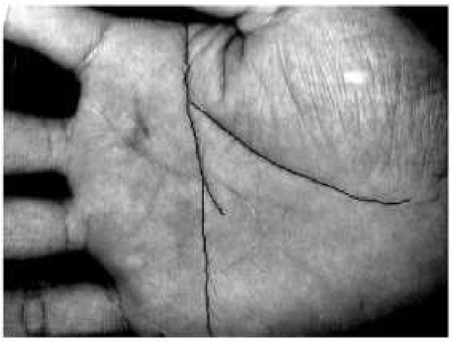

(f) Category 6

Figure 2.15 Examples of six classes of palmprint classified by principal lines. [109]

Chapter 3. An Apparatus and Methods for Online Multispectral Palmprint Recognition

There is no commercial available multispectral palmprint recognition acquisition device. This chapter will introduce the device design principle and the proposed apparatus. Based on a self collected large multispectral database, different multispectral recognition methods, including image level fusion, feature level fusion and score level fusion will be investigated and discussed.

3.1 An Apparatus for Online Multispectral Palmprint Recognition

To get multispectral palmprint images with high quality and short acquisition time, a low cost multispectral palmprint apparatus device was proposed. In this section we describe the components of our proposed device and its parameters. Two basic considerations in the design of a multispectral palmprint device are the color-absorptive and color-reflective characteristics of human skin and the light spectra to be used when acquiring images. Human skin is made up of three layers: the epidermis, dermis, and subcutis as shown in Fig. 3.1. Each layer contains a different proportion of blood and fat. The epidermis also contains melanin, while the subcutis contains veins [123]. Different light wavelengths will penetrate to different skin layers and illuminate in different spectra. Near Infrared (NIR) light penetrates human tissues further than visible light, and blood absorbs more NIR energy than surrounding tissues (e.g. fat or melanin) [124]. The device acquires spectral information from all the three dermal layers by using both visible bands and the NIR band. In the visible spectrum, a three mono-color LED (Light Emitting Diode) array is used with Red peaking at 660nm, Green peaking at 525nm and Blue peaking at 470nm. In the NIR spectrum, an NIR LED array peaking at 880nm is used. It has been shown that light in the 700-1000nm range can penetrate human skin while 880-930nm provides a good contrast of subcutaneous veins [124].

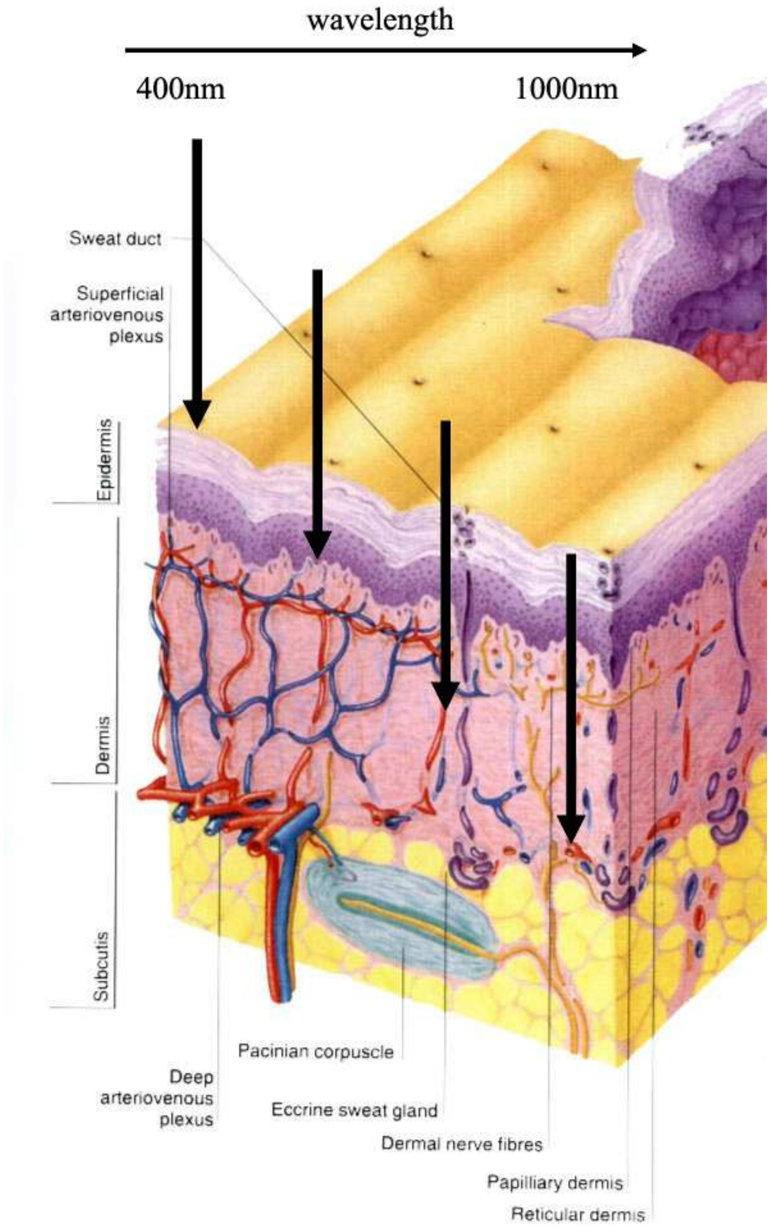

Figure 3.1 Cross-section anatomy of the skin.

Fig. 3.2 shows the structure of the designed multispectral palmprint image acquisition device and Fig. 3.3 shows the prototype of our device. It is composed of a CCD (charge-coupled device) camera, lens, an A/D (analogue-to-digital) converter, a multispectral light source and a light controller. A monochromatic CCD is placed at the bottom of the device. The A/D converter connects the CCD and the computer. The light controller is used to control the multispectral light. The camera, A/D converter and lens are selected based on our previous work [12, 32].

The device can capture palmprint images in a resolution of either 352 by 288 or 704 by 576. A user is asked to put his/her palm on the platform. Several pegs serve as control points for the placement of the user's hands. Four palmprint images of the palm are collected under different spectral lights. The switching time between the two consecutive lights is very short and the four images can be captured in a very short time (<1 second).

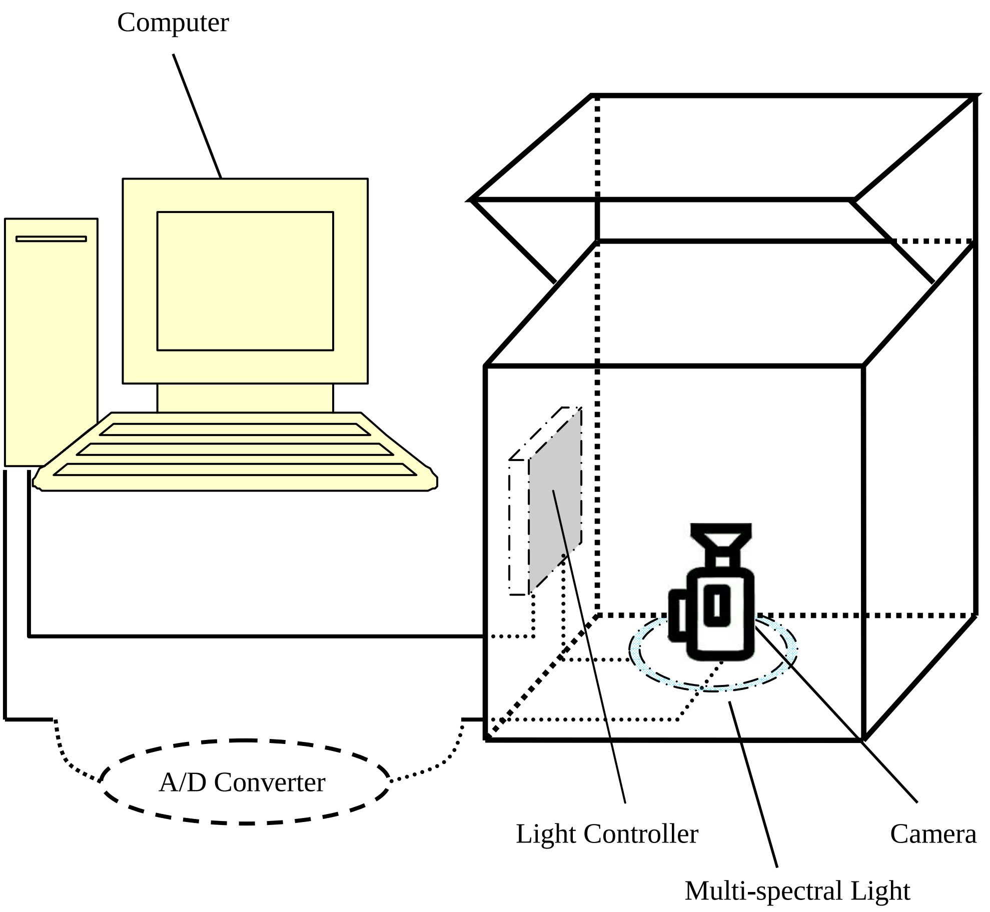

Figure 3.2 The structure of the multi-spectral palmprint acquisition device.

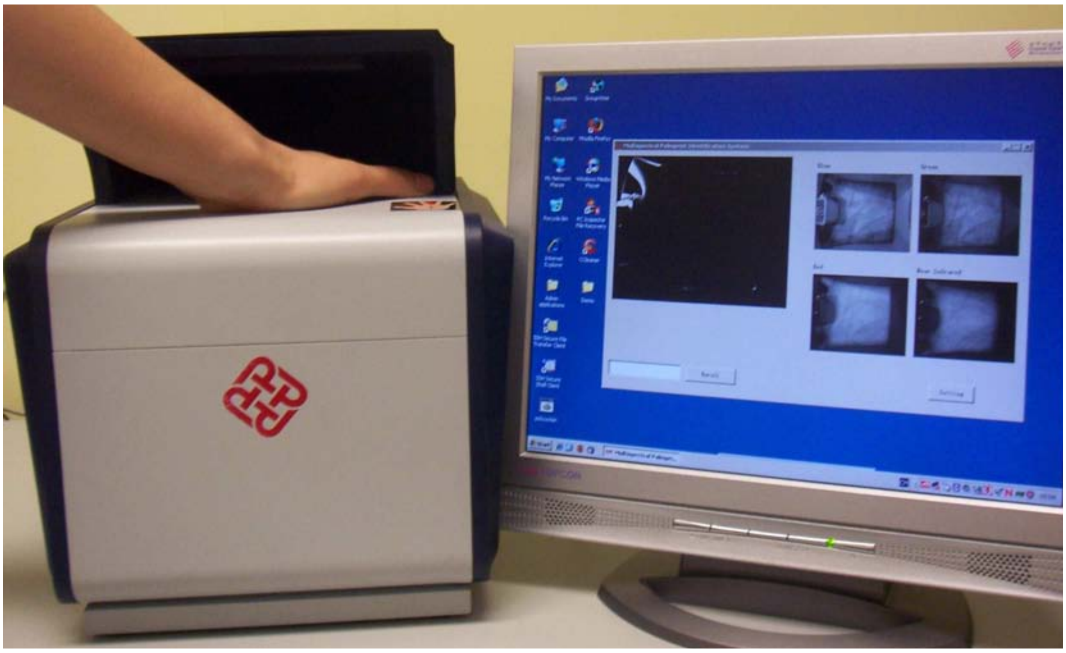

Figure 3.3 Prototype of the proposed multispectral palmprint system.

Fig. 3.4 shows a typical multispectral palmprint sample in the a) Blue, b) Green; c)

Red; and d) NIR bands. It can be observed that line features are clearer in the Blue and Green bands than in the Red and NIR bands. While the Red band can reveal some vein structures, the NIR band can show palm vein structures as well as partial line information. In our device, the palm vein structure acquired in the NIR band is not as clear as that reported in [124] because the CCD in our system is a standard CCTV (Closed Circuit Television) camera, instead of a near-infrared sensitive camera, to reduce cost. Moreover, we do not add an infrared filter in front of the CCD because the infrared filter would cut off the visible light and affect the acquisition of clear palmprint images under the visible spectrum.

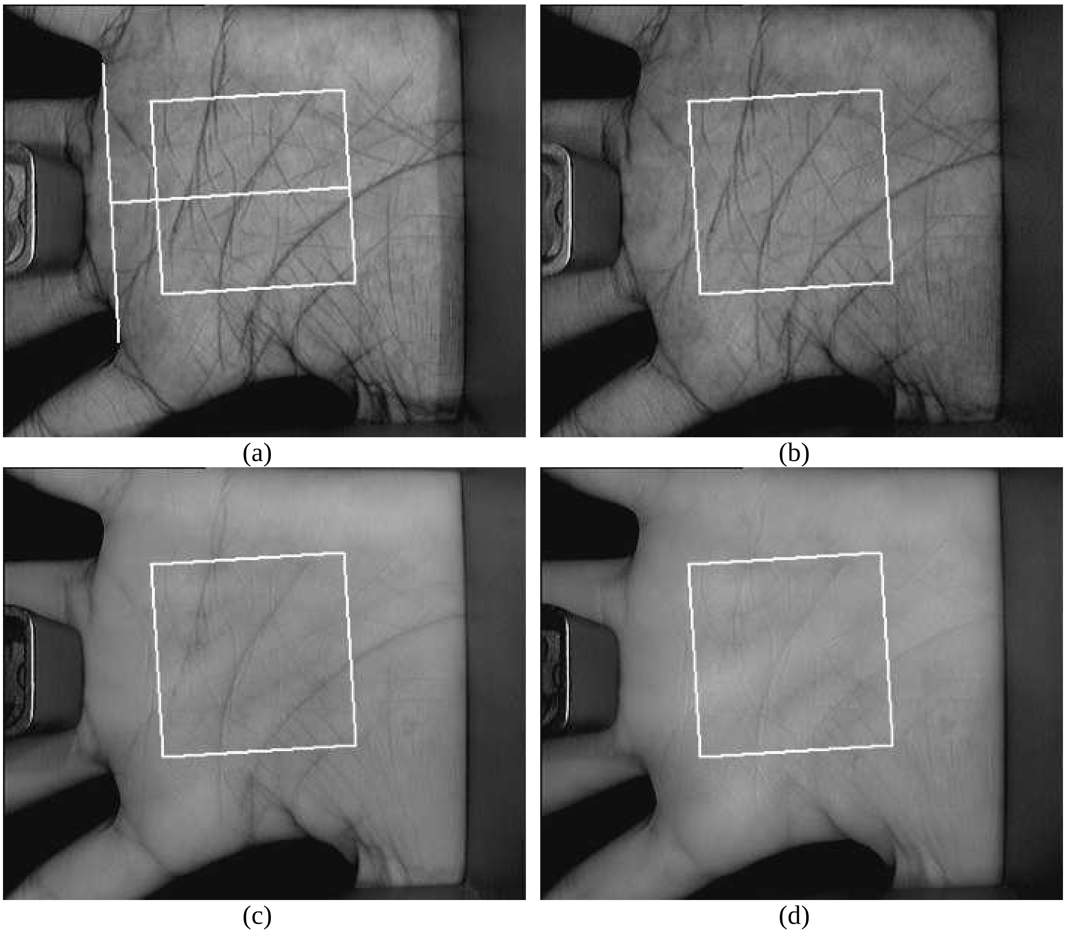

Figure 3.4 A typical multispectral palmprint sample. a) Blue; b) Green; c) Red; d) NIR. The white square is the ROI of the image.

A ROI will be extracted from the palmprint image for further feature extraction and matching. This can reduce the data amount in feature extraction and matching and reduce the influence of rotation and translation of the palm. In this paper, the ROI extraction algorithm in [12] is used and applied to the blue band (the ROI extraction accuracy on the other three bands is similar to blue band) to find the ROI coordinate system. After ROI extraction, the translation or rotation is usually small between two images. Thus no more registration procedure is necessary. Fig. 3.4 shows the ROI of the palmprint image and Fig. 3.5 shows the cropped ROI images.

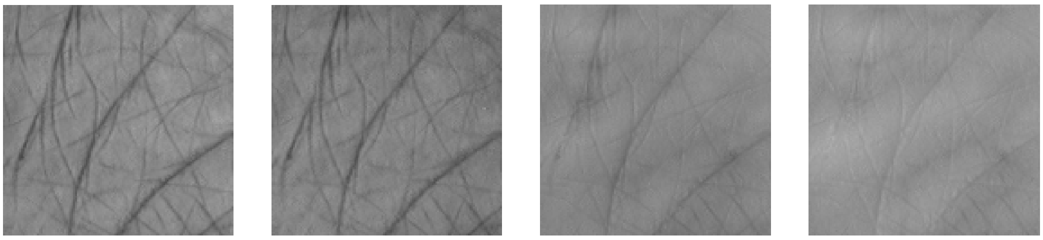

(a) (b) (c) (d)

Figure 3.5 ROI of Fig. 4. a) Blue; b) Green; c) Red; d) NIR.

3.2 Methods for Online Multispectral Palmprint Recognition

The experimental results on each feature band, which could be regarded as the baseline for multispectral palmprint recognition, is first investigated and discussed. Multispectral palmprint images could be regarded as a special case of multimodal. There are different ways to consolidate the information presented by multiple biometric measures. In this study, three kinds of widely used techniques [94], image level fusion, feature level fusion and matching score level fusion, are investigated. Here, we do not study decision level fusion as it may fail to reduce FRR and FAR simultaneously [170].

3.2.1 Verification Accuracy on Single Feature Band

CompCode [52] (refer to Section 1.5 for detail) is used for single feature band as the baseline. To further reduce the influence of imperfect ROI extraction, in matching we translate one of the two feature maps vertically and horizontally from -3 to 3. The minimal distance obtained by translated matching is treated as the final distance.

In this chapter, verification accuracy, equal error rate (EER, when false acceptance rate (FAR) equals to false rejection rate (FRR)), is used to evaluate the accuracy. The verification test is implemented on the PUMPD (refer to Section 1.4.1 for detail). Each image is compared with the remaining images in the database. If the two images come from the same palm, this comparison is counted as a genuine match; otherwise, it is counted as an impostor match. The numbers of genuine matching and impostor matching are 33,000 and 17,964,000 respectively.

The receiver operating characteristic (ROC) curves for different spectral bands are shown in Fig. 3.6. The accuracy values are listed in Table 3.1. The accuracy on each single band is comparable to those of state-of-the-art (EER: 0.024%) [128] on the public palmprint database [127] collected under white illumination.

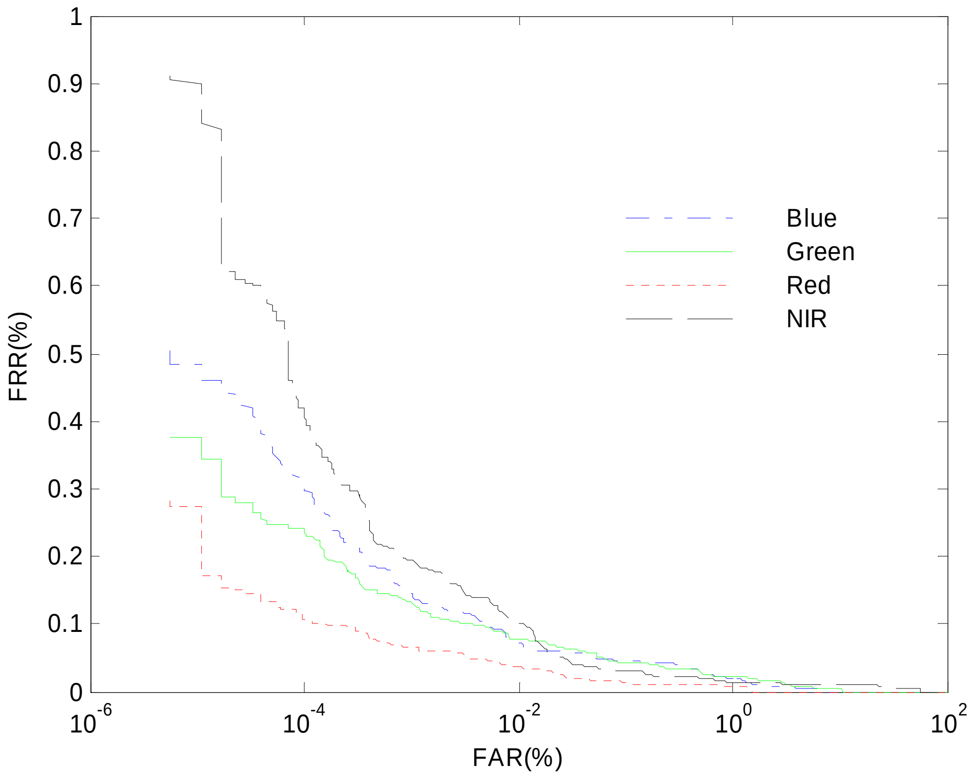

Figure 3.6 ROC curves of each spectral band.

Table 3.1 Accuracy value for different bands on PUMPD.

Feature Band	EER (%)
Blue	0.0515
Green	0.0529
Red	0.0248
NIR	0.0396

Several findings could be found from the experimental results. Firstly, Red and NIR bands have better EER than Blue and Green bands. This is mainly because Red and NIR could not only capture most of palm line information, but also capture some palm vein structures. This additional palm vein information helps classify those palms with similar palm lines. Fig. 3.7 shows an example, the two multispectral images of different palms have small distance under Blue ((a) and (e)) or Green ((b) and (f)) bands, which may lead to a false match; however, their distance under Red ((c) and (g)) or NIR ((d) and (h)) bands is large, which will lead to a correct match.

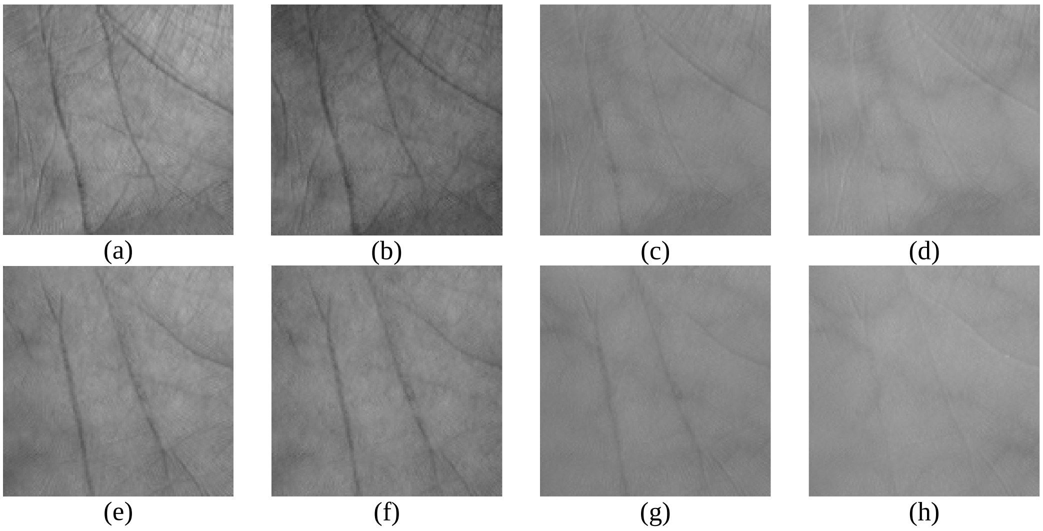

Figure 3.7 Multispectral images of two different palms which are wrongly recognized under Blue or Green spectrum, but can be correctly recognized under Red or NIR spectrum. From a-b) or e-h), the four images correspond to Blue, Green, Red and NIR respectively.

Secondly, the EER of NIR is higher than that of Red. There are mainly two reasons. First, the palm lines in NIR band is not as strong as those in the Red band because NIR light can penetrate deeper the palm skin than Red light, which attenuates the reflectance. Second, some people, especially females, have very weak vein structures under NIR light because their skin is a little thicker [129]. Fig. 3.8 shows an example. Figs. 3.8 (b) and (d) are the NIR images of a palm. The line structure in the two images is very weak compared with Figs. 3.8 (a) and (c), which are the Red images of the palm. Meanwhile, the vein structure in Figs. 3.8 (b) and (d) is not strong enough. Thus the palm will be falsely recognized in the NIR band, while it can be recognized in the Red band. Finally, the performance of Blue and Green bands is very similar. As can be seen in Fig. 3.4 and Fig. 3.5, the palm lines in Blue and Green bands look very similar.

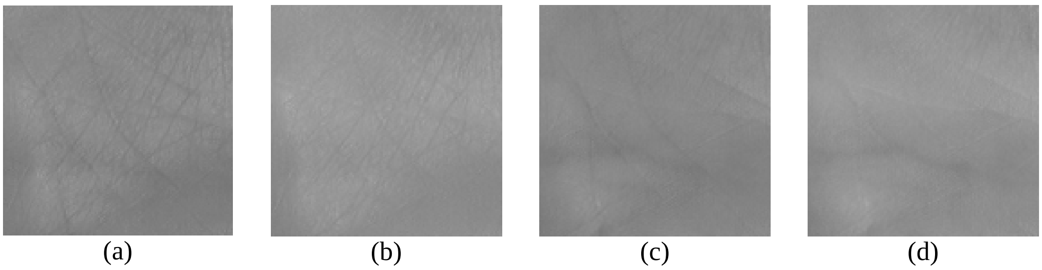

Figure 3.8 An example of palm which is falsely recognized in NIR band but can be correctly recognized in Red band. a) and c) are collected under Red light while b) and d) are collected under NIR light.

In this chapter, the robustness to motion blur is evaluated. Motion blur [133] could be simulated by mathematics motion model. Supposing the image exposition time is *T*, in this time duration, the palmprint image could be expressed by:

$$g(x,y)=\int_0^T f\left[x-x_0(t),y-y_0(t)\right]dt \tag{3-1}$$

where $g(x,y)$ is the simulated motion blur image, $f(x,y)$ is the original image. The image translation in T duration could be expressed by $x_0(t) = a\frac{t}{T}, y_0(t) = b\frac{t}{T}$, here a and b are two parameters to control the degree of motion. The Fourier transform of Eq.3-1 is:

$$G(u,v) = H(u,v)F(u,v) \tag{3-2}$$

where $G(u,v)$ and $F(u,v)$ is the Fourier transform of $g(x,y)$ and $f(x,y)$, respectively. $H(u,v)$ could be computed by:

$$H(u,v) = \frac{T}{\pi(ua+vb)}\sin[\pi(ua+vb)]e^{-j\pi(ua+vb)} \tag{3-3}$$

As shown in Eq. 3-1-3.3, there are totally three parameters, *T*, *a*, and *b*, to control the degree of motion. In the simulation test, *T* is fixed to 1, *a* and *b* are randomly selected from [10^{-4}, 10^{-3}]. Fig. 3.9 shows an example of blurred image.

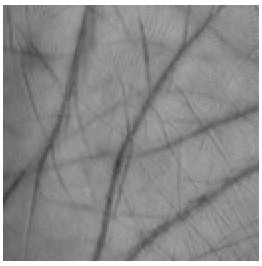

(a)

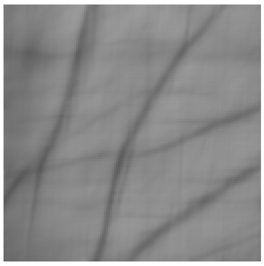

(b)

Figure 3.9 An example motion blur. a) Original image; b) Simulation of blurred image.

Table 3.2 Accuracy values for different bands on PUMMBPD.

Fusion Combination	EER (%)
Blue	0.2087
Green	0.1675
Red	0.1488
NIR	0.1455

The verification results on single band of PUMMBPD (refer to Section 1.4.2 for detail) are listed in Table 3.2. Compared with Table 3.1, Table 3.2 shows that the verification accuracy drops very quickly when the database includes blurred images.

3.2.2 Image Level Fusion

The image fusion method tries to solve the problem of combining information from several images taken from the same object to get a new fused image. The wavelet-based approach is a widely used technique in image fusion [125]. In this section, Haar wavelet, a kind of discrete wavelet transform (DWT), is selected to fuse multispectral palmprint images. The framework is shown in Fig. 3. 10.

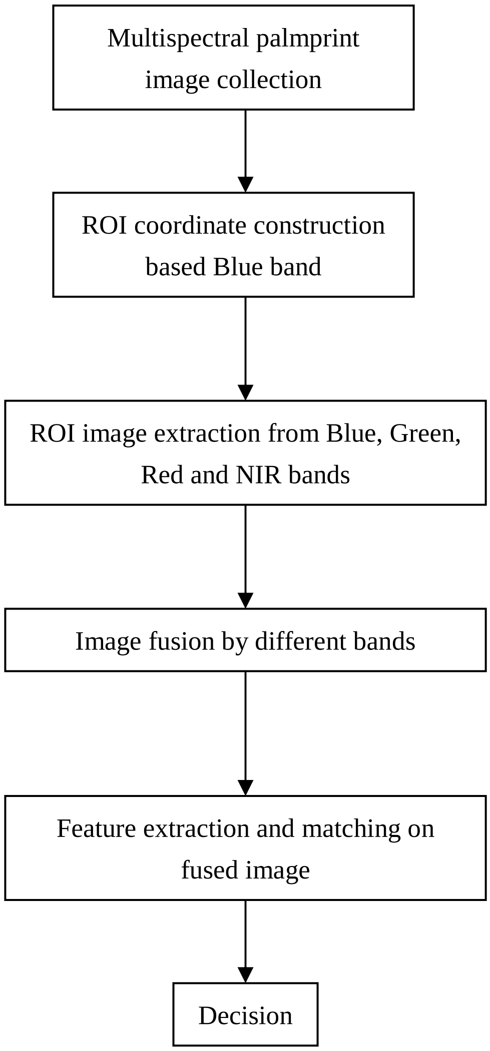

Figure 3.10 Framework of image level fusion.

3.2.1.1 Fusion Algorithm

Haar wavelet, a well known wavelet function, is applied in this section. It is composed of two orthogonal functions:

$$\phi(x) = \begin{cases} 1 & \text{for } 0 \le x < 1, \\ 0 & \text{otherwise.} \end{cases} \tag{3-4}$$

$$\psi(x) = \begin{cases} 1 & \text{for } 0 \le x < 0.5, \\ -1 & \text{for } 0.5 \le x < 1, \\ 0 & \text{otherwise.} \end{cases}$$

For a 2D image *I(x,y)*, it could be decomposed by four parts, one approximation coefficients matrix, A, and three detail coefficient matrixes, D_H, D_V, and D_D in horizontal, vertical and diagonal directions:

$$
\begin{aligned}
A &=< I(x,y), \phi(x)\phi(y) > \\
D_H &=< I(x,y), \psi(x)\phi(y) > \\
D_V &=< I(x,y), \phi(x)\psi(y) > \\
D_D &=< I(x,y), \psi(x)\psi(y) >
\end{aligned}
\tag{3-5}
$$

To get non redundant information and perfect reconstruction, A, D_H, D_V and D_D are down-sampled to half size in both horizontal and vertical directions.

Based on image decomposition and reconstruction theory, Mallat proposed a fast multiscale wavelet algorithm [126]. The approximate coefficients on scale *j* could be further decomposed into four parts:

$$
\begin{aligned}
A^{j+1} &=< A^j(x,y), \phi(x)\phi(y) > \\
D_H^{j+1} &=< A^j(x,y), \psi(x)\phi(y) > \\
D_V^{j+1} &=< A^j(x,y), \phi(x)\psi(y) > \\
D_D^{j+1} &=< A^j(x,y), \psi(x)\psi(y) >
\end{aligned}
\tag{3-6}
$$

Similarly, down-sampling is applied in the next *j*+1 sacle. Fig 3.11 illustrates the multiscale wavelet decomposition. Fig 3.12 shows a sample of palmprint image decomposition.

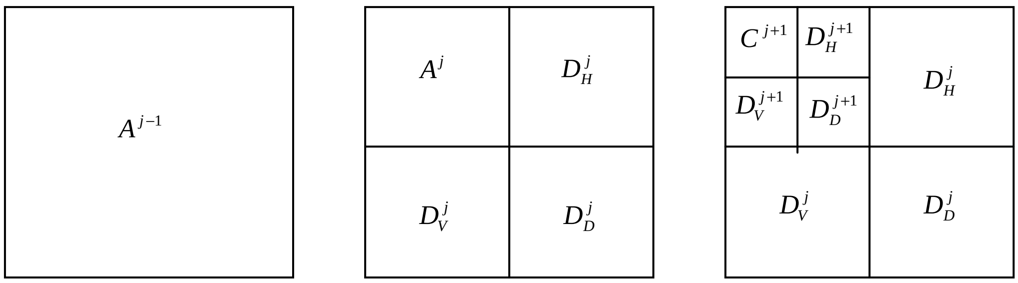

Figure 3.11 Illustration of multiscale wavelet decomposition.

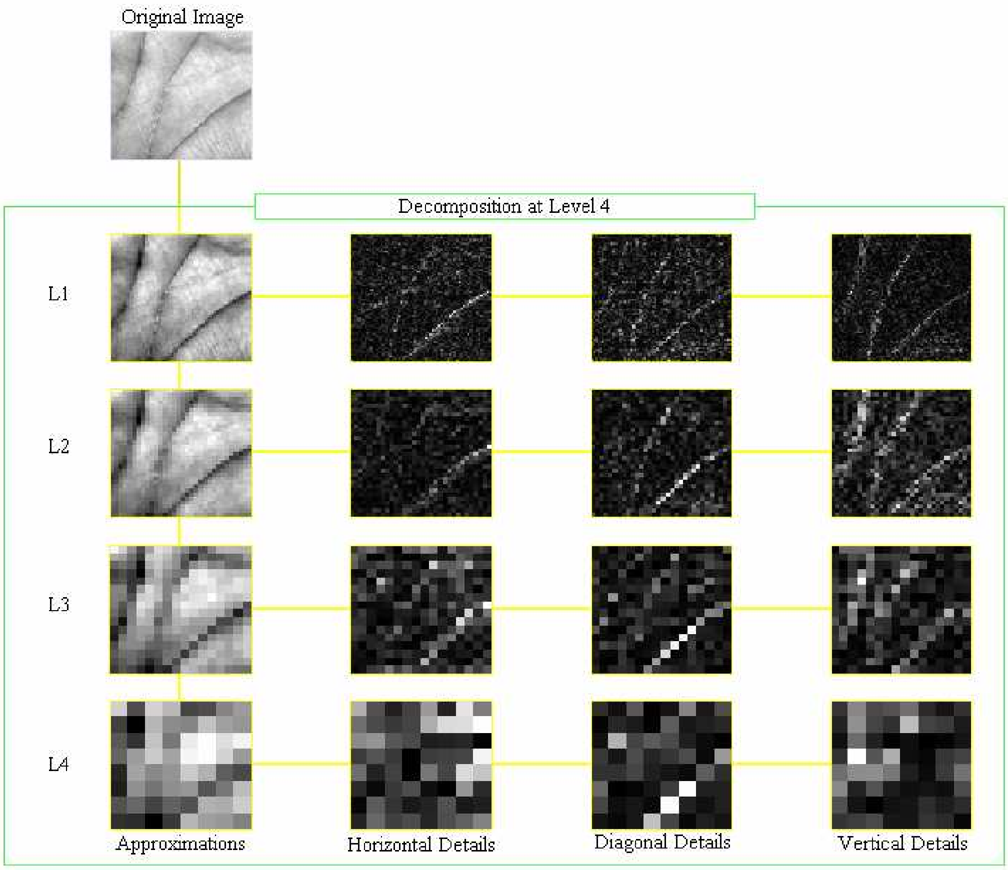

Figure 3.12 4 level palmprint image decomposition.

After wavelet decomposition, coarse scale keeps structure information, while fine scale contains detail features. According to different requirement of applications, structures and detail features could be processed separately. Thus, wavelet decomposition has been applied to many image processing fields, such as, compression, edge detection and noise reduction.

Image fusion is an important application in wavelet analysis. Multiple images can be combined into one image while represent many important features. To keep image structure while maintain high frequency information, a wavelet based image fusion algorithm is proposed, the pseudocode is as follows:

1) By applying Haar wavelet on each spectral palmprint image, the image is decomposed into three levels;

2) A new coefficient matrix of a fused image is computed. For low frequency part, mean strategy is used. The average coefficients of low frequency from different images are gotten for the new coefficient matrix;

3) For high frequency part, max strategy is applied. The maximal coefficients of high frequency from different images are computed for the new coefficient matrix;

4) Inverse wavelet is applied on the new coefficient matrix to get the fused image.

Fig. 3.13 shows an illustration of the procedure and Fig. 3.14 gives an example.

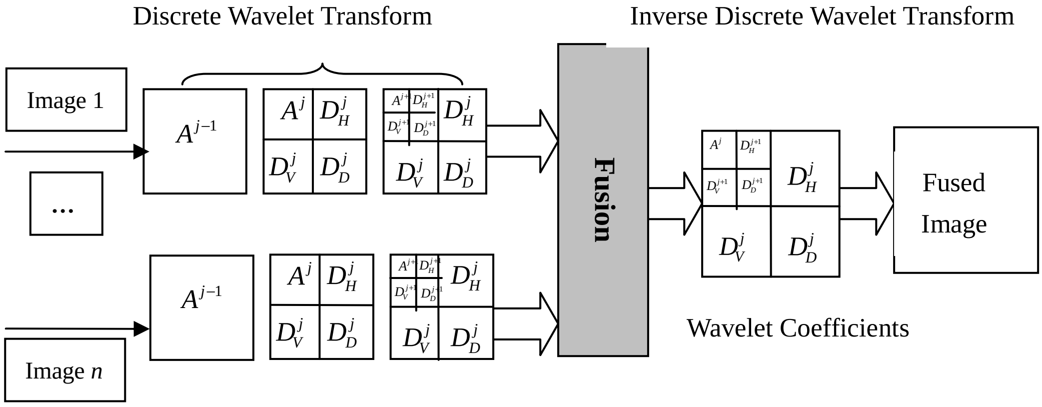

Figure 3.13 Illustration of image fusion.

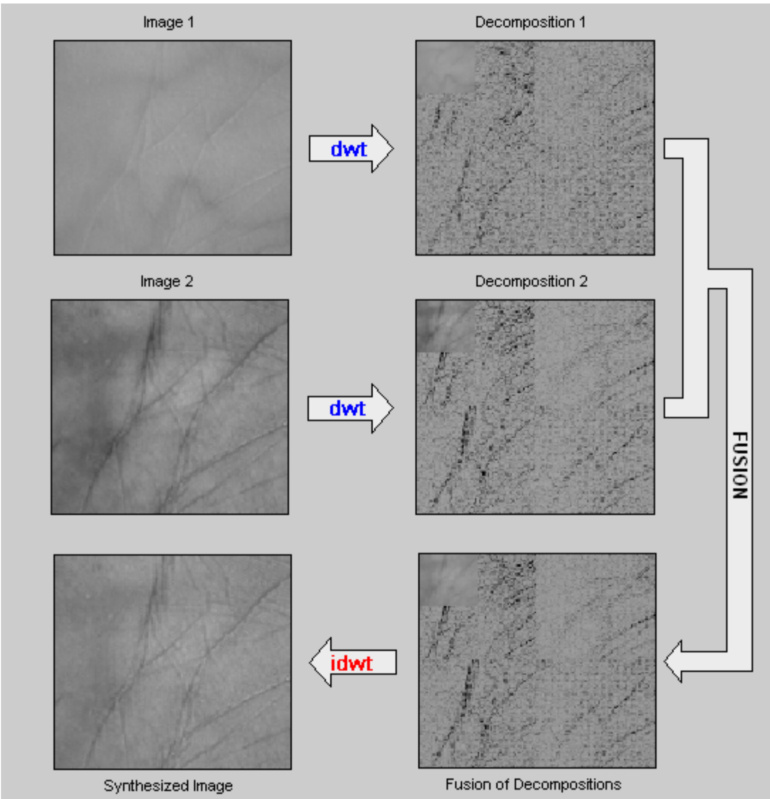

Figure 3.14 An example of image fusion.

3.2.1.2 Experimental Results

Using the fusion algorithm discussed in above section, different kinds of fusion images were generated. Then, CompCode, described in Section 3.2.1, is used for feature extraction and Hamming distance is employed for feature comparison. By using the same test protocol as mentioned above, the acquired accuracy is listed in Table 3.3.

Table 3.3 Accuracy values for different fusions on PUMPD.

Fusion Combination	EER (%)
Blue, Green	0.0576
Blue, Red	0.0577
Blue, NIR	0.0607
Green, Red	0.0454
Green, NIR	0.0568
Red, NIR	0.0286
Blue, Green, Red	0.0605
Blue, Green, NIR	0.0665
Blue, Red, NIR	0.0679
Green, Red, NIR	0.0576
Blue, Green, Red, NIR	0.0696

Compared with Table 3.1, fusion method could not improve accuracy. It is mainly because wavelet based image fusion may bring artificial artifacts sometimes. As CompCode extracted an orientation feature for each pixel, these artifacts may bring wrong orientation or fake feature.

Although image level fusion may fail to improve accuracy, it owns two merits. First, it is robust to motion blur which may occur in real situations. Second, it could be applied for liveness detection.

Table 3.4 shows the accuracy on motion blur database. Except fusion of Blue and NIR, Table 3.4 illustrates that fusion could get better result than single feature band. It also shows that fusing more feature bands can improve accuracy usually, which is different from Table 3.2. It is because motion blur may occur on some bands, not all bands, in most cases. It is close to real situations, as an unfamiliar user may withdraw his/her palm before the device finishes data collection. Although, image registration is not applied before image fusion, motion blur effect could be reduced somewhat by image level fusion technique.

Table 3.4 Accuracy values for different fusions on PUMMBPD.

Fusion Combination	EER (%)
Blue, Green	0.1030
Blue, Red	0.1029
Blue, NIR	0.1936
Green, Red	0.0788
Green, NIR	0.1181
Red, NIR	0.0969
Blue, Green, Red	0.0700
Blue, Green, NIR	0.1061
Blue, Red, NIR	0.1182
Green, Red, NIR	0.0943
Blue, Green, Red, NIR	0.0757

Antispoof [130] ability is an important property in a real system. Traditional palmprint recognition acquires reflectance information by one light only, so it is not difficult to spoof the system, sometime, a printed palmprint image may be falsely accepted [131]. However, the reflectance of human skin is related with spectral wavelength [132], as shown in Fig. 3.15. A true palm, which is composed of different layers, will show varied spectral property under different feature bands, while a fake palm has same reflectance rate in different spectra. As the image acquisition procedure is fast, it is very difficult to provide several fake palms in such a short time. Since image level fusion could consolidate different features into one image, much distinctive feature from each spectral is maintained. Thus, the fused image will be different from any single spectral palmprint image and fake fused image.

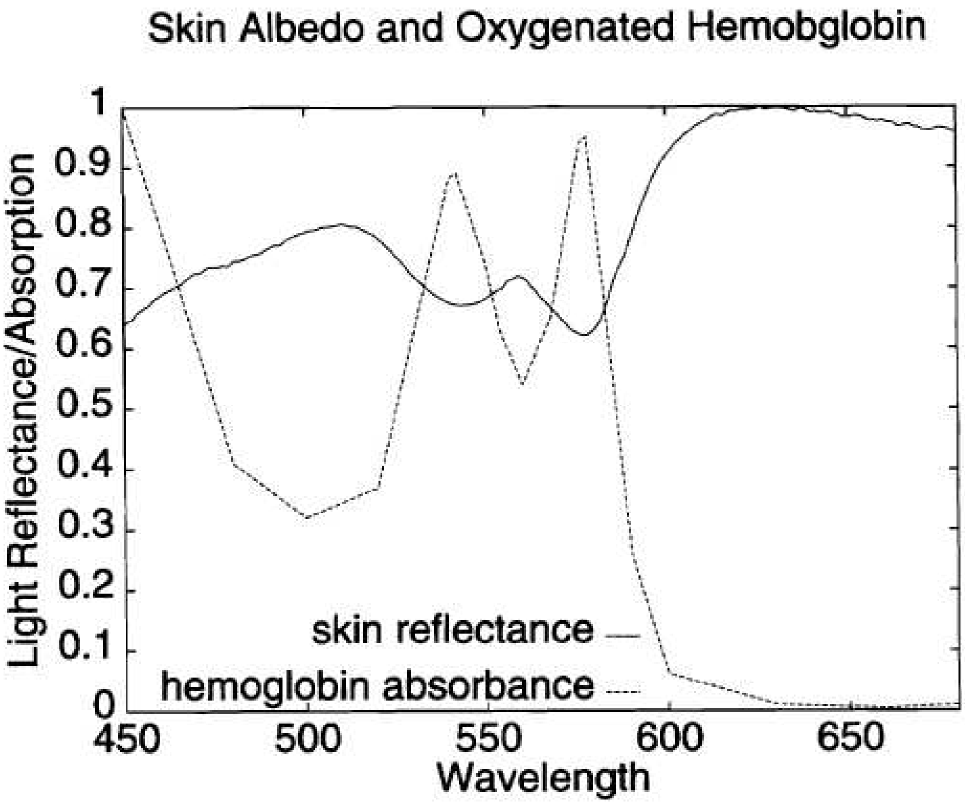

Figure 3.15 Skin reflectance vs hemoglobin absorption. [132]

A simple experiment shows the robustness of the multispectral palmprint recognition system. Fig. 3.16 shows an example of faked multispectral palmprint which is captured from a printed paper and an example of true multispectral palmprint. Their fused images by four channels are also shown in Fig. 3.16. As shown in it, a true palm has different image characteristics by different spectra, while the difference between different spectra in fake palm is very small.

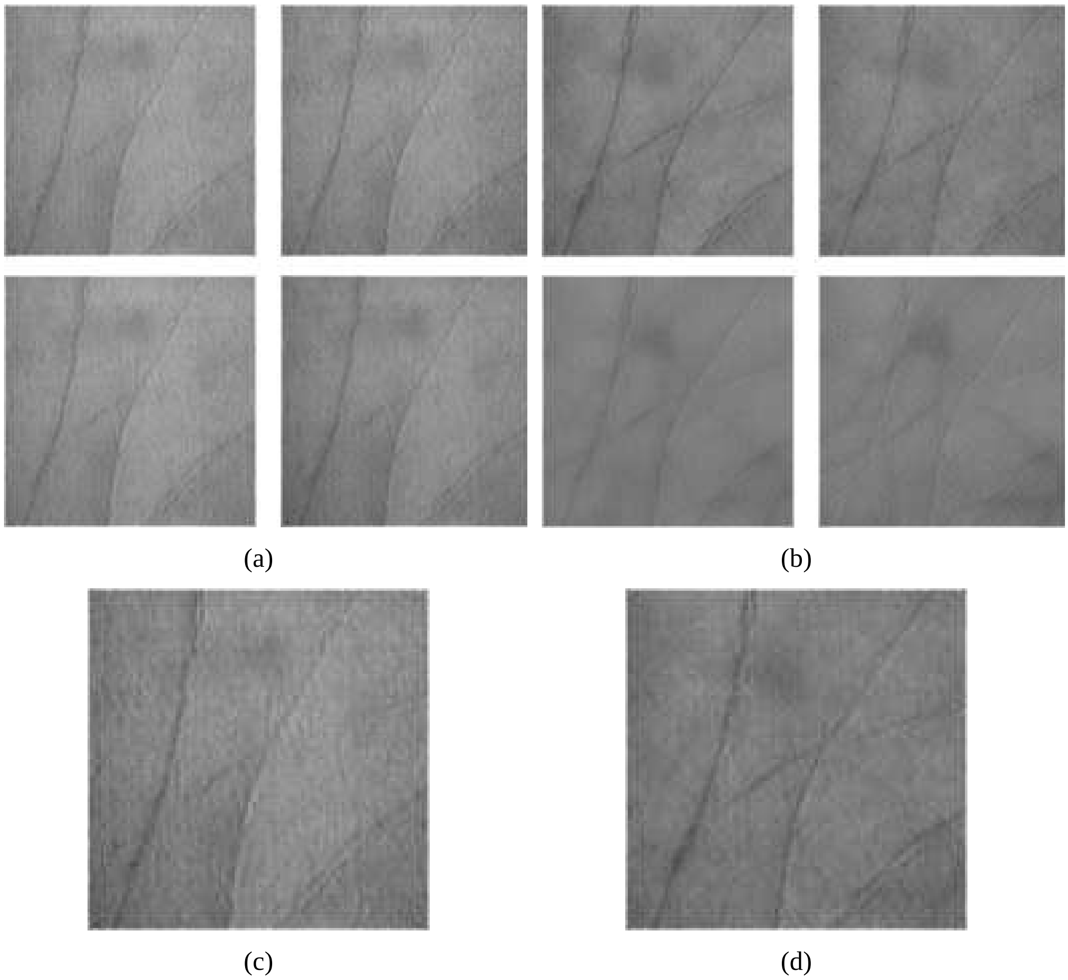

Figure 3.16 An example of fake and true multispectral palmprint images with their fused images. a) faked palmprint by four channels; b) true palmprint by four channels; c) fused fake palmprint; d) fuse true palmprint

Three groups of faked multispectral palmprint images and three groups of true images were collected. The fused images by four channels were constructed and compared using CompCode. Table 3.5 lists the Hamming distance between true and fake palms and Table 3.6 shows the distance between true palms.

Table 3.5 Distance between true and fake palms.

Distance	True I	True II	True III
Fake I	0.4083	0.4128	0.4137
Fake II	0.3947	0.4034	0.4197
Fake III	0.3986	0.3982	0.4157

Table 3.6 Distance between true palms.

Distance	True I	True II	True III
True I	0	0.2473	0.3125
True II		0	0.3440
True III			0

As shown in Table 3.5 and Table 3.6, the distance between true palms is much smaller than that of fake and true palms. For example, the maximal distance between true palms is 0.3440 while the minimal distance between true and fake palms is 0.3986. Usually, 0.39 is the threshold corresponding to EER. Thus, fake palms could be rejected correctly.

3.2.3 Feature Level Fusion

Although image level fusion could reduce the possible feature size as only one image is kept, some of discriminant information may be lost, so the recognition accuracy may not be increased. This section will investigate feature level fusion with which we could consider the correlation between different feature bands and get better results than single spectrum alone. Fig. 3.17 illustrates the framework of feature level fusion.

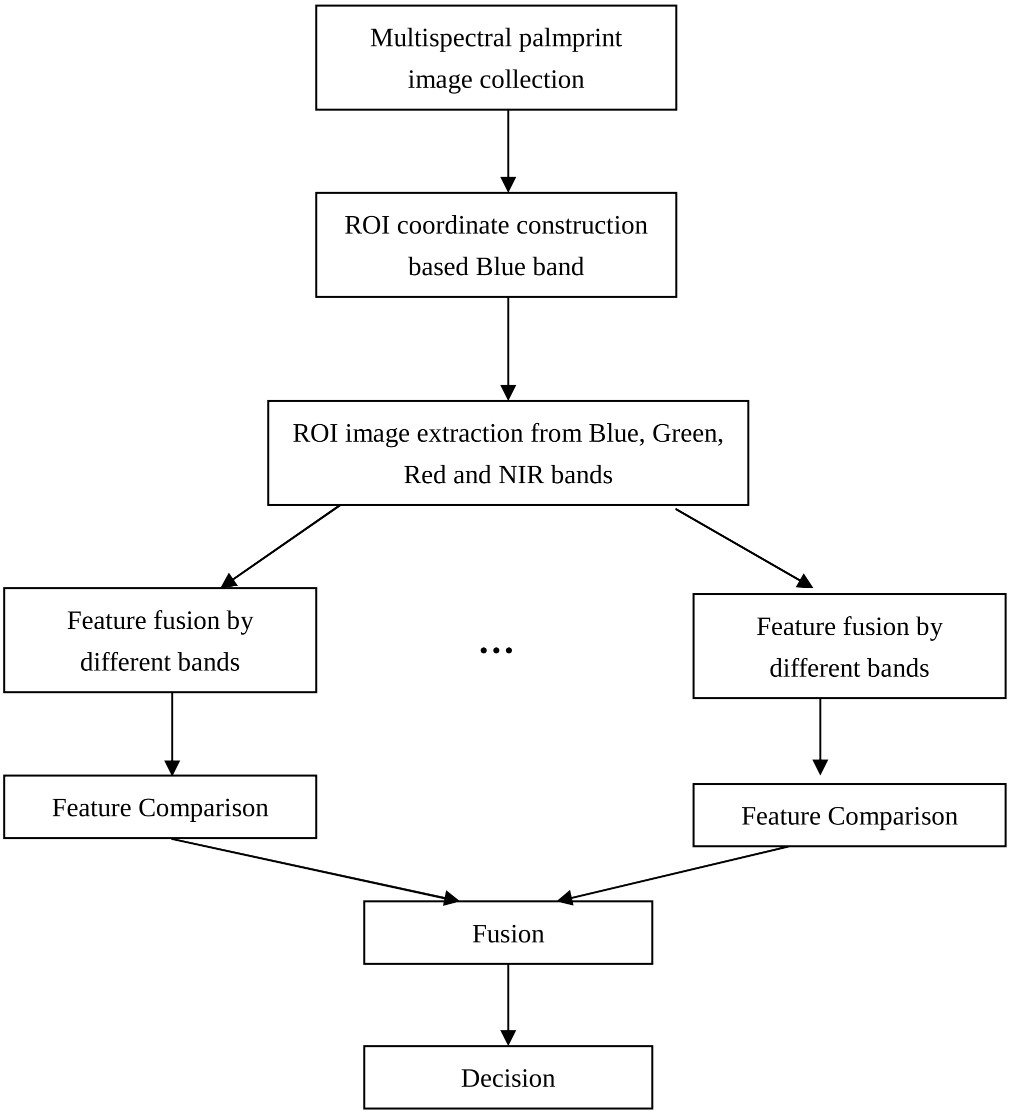

Figure 3.17 Framework of feature level fusion.

3.2.3.1 Min-Min Fusion Scheme

As CompCode extracts orientation feature from each pixel, so the most intuitive and simplest way is to create joint feature from two feature bands for each pixel:

$$O^f(x,y) = O^i(x,y)*6 + O^j(x,y) \tag{3-7}$$

where $O^i(x,y),\ O^j(x,y) \in \{0,1,2,3,4,5\}$, $i, j \in \{\text{Blue,Green,Red,NIR}\}$ and $i \neq j$. (x, y) indicate the position of a pixel. This kind of joint representation could use the least number of bits for binary representation. In the following, this kind of fusion is named as, Min-Min Fusion. It has limitation as it is difficult to extend to three or four feature bands, as the possible feature space will be huge and the length of binary string will be too long. In a real situation, instead of extracting joint feature from all spectra, hybrid technique could be used. Such as, partition the four spectra into two groups, each group has two feature bands, then extract fused feature from each group and finally apply score level fusion.

For the fused feature, there are totally 36 kinds of possible values, integer value from 0 to 35. Each joint value is represented by its binary representation. The distance between two features could be compared by:

$$\begin{aligned} D(P,Q) &= \frac{\sum_{y=1}^{M}\sum_{x=1}^{N} P^b(x,y) != Q^b(x,y)}{M*N} \\ &= \frac{\sum_{y=1}^{M}\sum_{x=1}^{N} (P_1^b(x,y) \otimes Q_1^b(x,y)) \cup \ldots \cup ((P_6^b(x,y) \otimes Q_6^b(x,y)))}{M*N} \end{aligned} \tag{3-8}$$

where *P* and *Q* represent two palmprint orientation feature maps, P_i^b and Q_i^b are the i^{th} bit plane of *P* and *Q*, respectively. Symbol "$\otimes$" represents bitwise exclusive OR.

However, the verification accuracy of this method is not promising as shown in Table 3.7. It shows that fusion of Blue and NIR could get better accuracy. Fusion of Green and NIR is better than Green, but a little inferior than NIR. The remaining fails to improve the accuracy than single spectrum.

Table 3.7 Accuracy values for Min-Min Fusion on PUMPD.

Fusion Combination	EER (%)
Blue, Green	0.1484
Blue, Red	0.2817
Blue, NIR	0.0313
Green, Red	0.2668
Green, NIR	0.0423
Red, NIR	0.2442

This is probably because the strong correlation between different images by different spectrum. Fig. 3.18 plots the cross-section profile of different palmprint images.

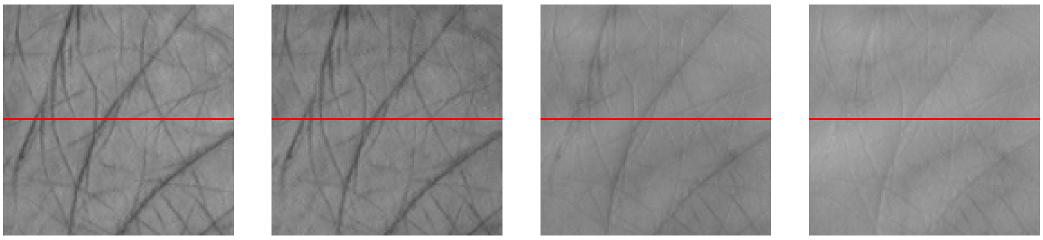

(a) (b) (c) (d)

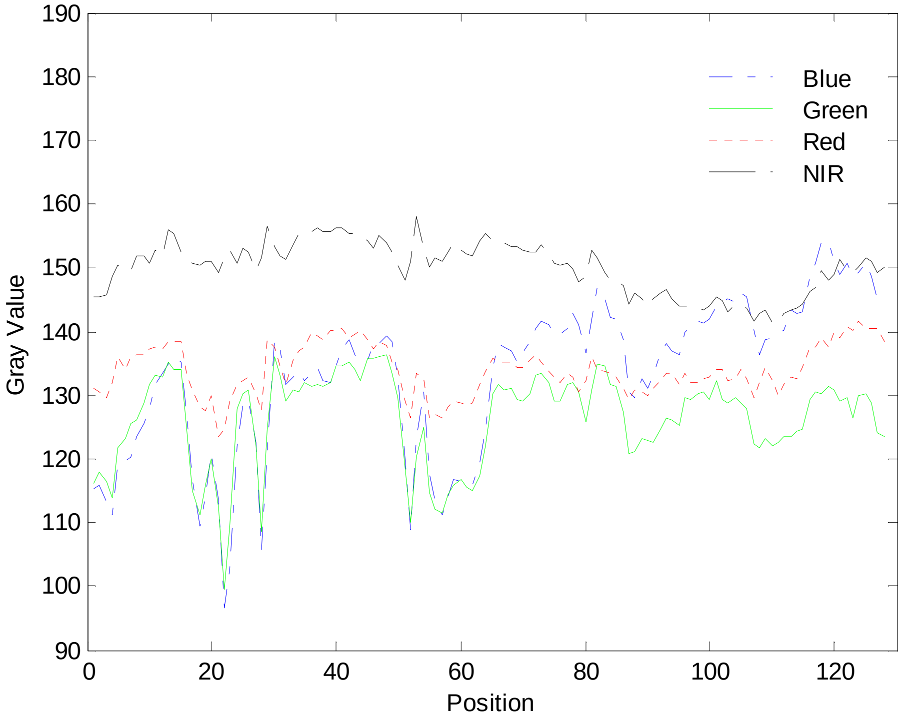

(e)

Figure 3.18 An example of profile of image. (a)-(d) original image of Blue, Green, Red and NIR channel. (e) Profile of (a)-(b).

As shown in Fig. 3.18, Blue and Green channel get more similar intensity distribution, while the similarity between NIR and Blue, or NIR and Green is small. To further validate it, an identical CompCode map is plotted in Fig. 3.19. Usually, the higher percentage of identical orientation indicates higher correlation between two spectra. The quantitive value is shown in Table 3.8.

Table 3.7 and Table 3.8 show the proposed feature level fusion is not suitable for high correlated spectra. Fig. 3.20 shows the relationship between correlation and fusion accuracy. Since Blue and NIR, and Green and NIR have less correlation, so their fusion could get better results than other combination. Blue and Red, Green and Red, and Red and NIR have medium correlation, their fusion gets worse result. Blue and Green has the large correlation while medium fusion accuracy. Thus, a less correlated fusion strategy is preferred and is proposed in the following.

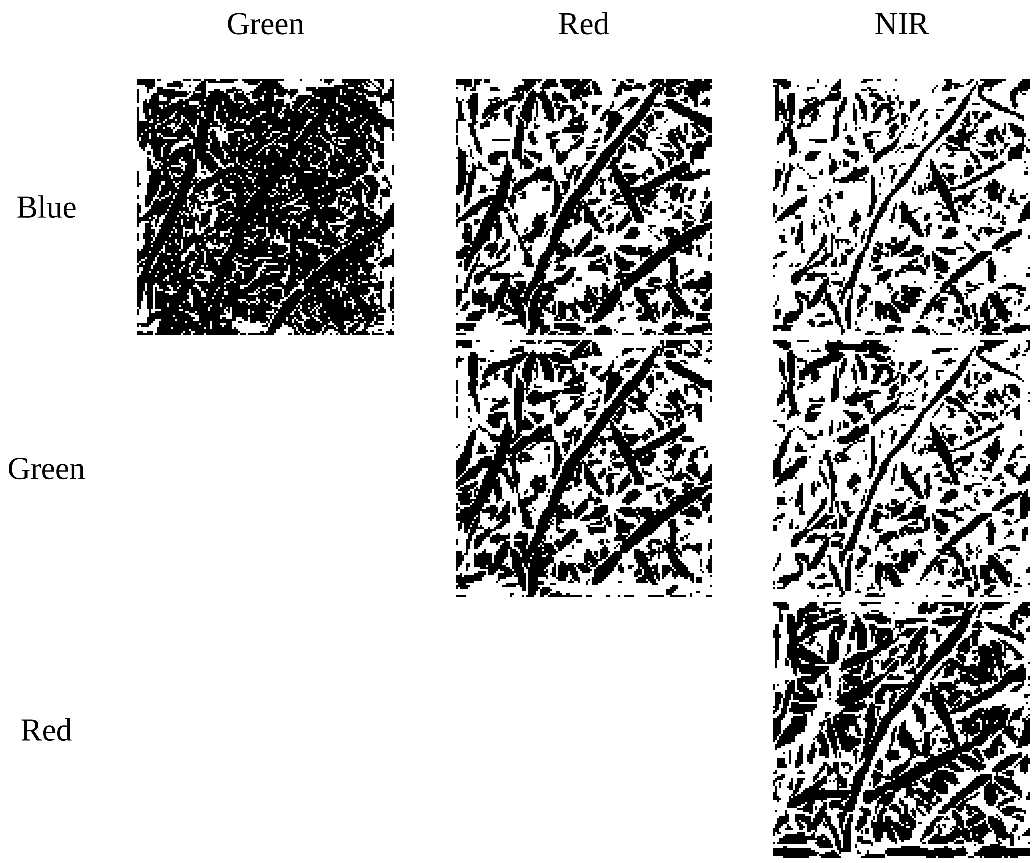

Figure 3.19 Identical features between different spectra. (Black pixels represent pixels with identical orientation while white pixels represent pixels with different orientation.)

Table 3.8 The average percentage (%) of identical orientation features between different spectral bands in PUMPD.

Fusion Combination	Average Percentage (%)
Blue, Green	77.1441
Blue, Red	52.4086
Blue, NIR	33.9168
Green, Red	55.3237
Green, NIR	35.7150
Red, NIR	55.6474

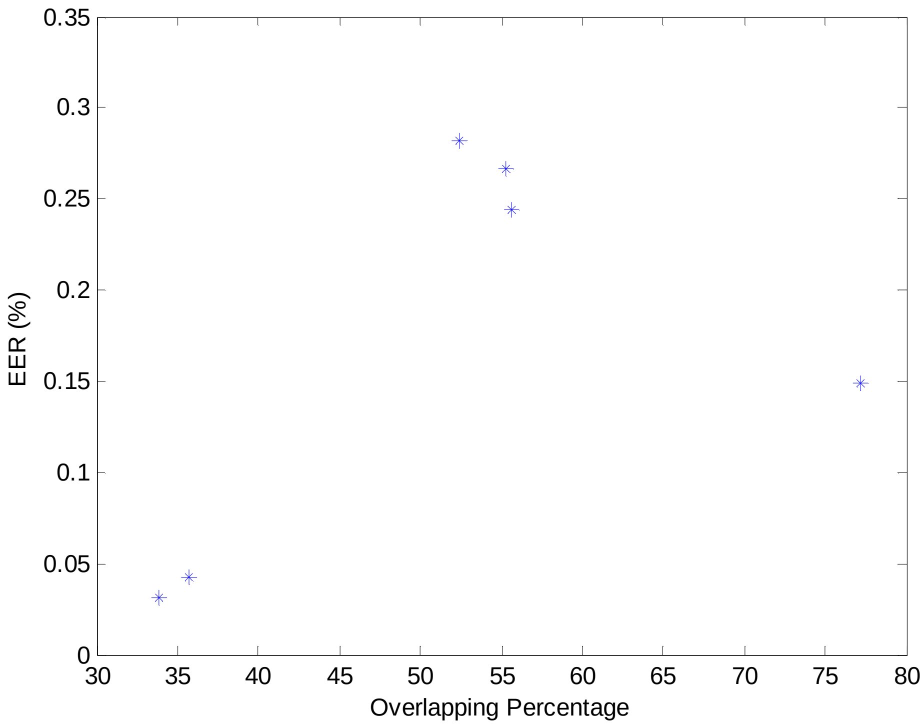

Figure 3.20 Percentage of identical orientation vs fusion accuracy.

3.2.3.2 Min-Max Fusion Scheme

First, CompCode is inspected. The original CompCode extracts the orientation for the minimal responses from six orientations. Is minimal response's orientation the best among six orientations and does any other orientation provide useful information? To address this issue, instead of extract the orientation of the minimal response, other orientation is extracted and compared. The achieved EER is shown in Table 3.9.

Table 3.9 The recognition accuracy of different orientation extraction scheme.

EER (%)	1st Minimal	2nd Minimal	3rd Minimal	4th Minimal	5th Minimal	6th Minimal
Blue	0.0515	0.4673	3.3755	3.0062	0.4231	0.1206
Green	0.0529	0.3950	3.4180	2.8299	0.3632	0.1089
Red	0.0248	0.2159	1.8748	1.4614	0.2306	0.0880
NIR	0.0396	0.2838	2.9110	2.6411	0.2964	0.0850

As shown in Table 3.9, orientation corresponding to minimal response is the most robust and could get better accuracy. While orientation corresponds to maximal response could get sound results. It can be regarded as a kind of bright line orientation extractor.

Ideally, orientation corresponds to maximal response should be orthogonal to orientation with minimal response. However, palmprint image is composed of complex structures, thus this rule may not be met. To investigate the correlation between minimal and maximal response, a co-occurrence matrix for same spectral samples is shown in Table 3.10.

Table 3.10 Co-occurrence percentage (%) of minimal and maximal orientation index for same spectral.

Max\Min Orientation Index	0	1	2	3	4	5
0	0	3.63	4.36	3.13	4.29	3.64
1	1.92	0	3.02	2.86	3.65	3.67
2	2.46	3.12	0	2.44	3.61	3.61
3	2.98	4.85	4.04	0	3.72	4.89
4	2.39	3.51	3.77	2.26	0	2.92
5	1.89	3.53	3.67	2.85	3.20	0

Table 3.10 shows that there is no strong correlation between orientation with minimal response and maximal response, for the same spectral. Thus, the correlation between different spectral should be small, too. A new feature level scheme, Min-Max Fusion, is proposed:

$$O^f(x,y) = O^i_{\min imal}(x,y) * 6 + O^j_{\max imal}(x,y) \tag{3-9}$$

where $O^i_{\min imal}(x,y), O^j_{\max imal}(x,y) \in \{0,1,2,3,4,5\}$. Eq. 3-8 is used for dissimilarity measurement.

Based on Min-Max Fusion scheme, the verification accuracy is listed in Table 3.11. As defined in Eq. 3-9, the sequence of fusion will affect the accuracy, such as when Blue channel is used to extract orientation with minimal response while Green channel is used to extract orientation with maximal response, it is different with fusion of Green and Blue. Compared with Table 3.7, Min-Max Fusion could get better results. Sometimes, the proposed fusion could get better results than single spectrum, such as Green and Blue, Green and NIR, Blue and NIR, and NIR and Green.

Table 3.11 Verification Accuracy of Min-Max Fusion for PUMPD.

Fusion Combination	EER (%)
Blue, Green	0.0541
Blue, Red	0.1459
Blue, NIR	0.0266
Green, Blue	0.0484
Green, Red	0.1791
Green, NIR	0.0335
Red, Blue	0.1840
Red, Green	0.1838
Red, NIR	0.0967
NIR, Blue	0.0393
NIR, Green	0.0301
NIR, Red	0.0934

For Min-Max Fusion, same as Min-Min Fusion, there are totally 36 kinds of values, integer from 0 to 35. However, some values, such as $O^f(x,y) = O^i_{\min imal}(x,y) * 6 + O^j_{\max imal}(x,y)$ when $O^i_{\min imal}(x,y) = O^j_{\max imal}(x,y)$ has less probability. Furthermore, these values show conflict situations. In one channel, there is a dark line while in the other channel, there is a bright line. As shown in Table 3.12, such kind of occurrence is neglectable and the percentage is higher as spectra difference increases, such as the percentage of Blue and Green is much smaller than that of Blue and NIR.

Table 3.12 Percentage (%) of pixels for $O^i_{\min imal}(x,y)=O^j_{\max imal}(x,y)$.

Fusion Combination	Percentage (%)
Blue, Green	0.086
Blue, Red	1.818
Blue, NIR	7.166
Green, Blue	0.096
Green, Red	1.433
Green, NIR	6.653
Red, Blue	2.140
Red, Green	1.545
Red, NIR	2.339
NIR, Blue	7.288
NIR, Green	6.482
NIR, Red	1.888

If the situations $O^i_{\min imal}(x,y)=O^j_{\max imal}(x,y)$ are removed, the possible number of integer value is reduced to 30, which could be represented by 5 bits only. Hamming distance similar as Eq. 3-9 is selected for distance measurement. In the following, this fusion scheme is named as Min-Max-Refined Fusion. The verification accuracy of this scheme on the database is shown in Table 3.13. Compared with Table 3.11, Table 3.13 shows that better accuracy is gotten after some pixels are removed. The best accuracy is gotten by fusion of Blue and NIR, 0.0182% EER.

Table 3.13 Verification Accuracy of Min-Max-Refined Fusion for PUMPD.

Fusion Combination	EER (%)
Blue, Green	0.0553
Blue, Red	0.0701
Blue, NIR	0.0182
Green, Blue	0.0484
Green, Red	0.0907
Green, NIR	0.0242
Red, Blue	0.1090
Red, Green	0.1089
Red, NIR	0.0510
NIR, Blue	0.0424
NIR, Green	0.0242
NIR, Red	0.0275

As discussed before, the proposed feature level scheme is difficult to apply for four bands, thus a hybrid fusion method is chosen: the feature level fusion, Min-Max-Refined, is applied on two spectra first, then score level fusion, sum, is used to fuse four channels. The accuracy achieved is listed in Table 3.14. It shows that hybrid fusion could improve the verification accuracy in most cases.

Table 3.14 Verification Accuracy of Hybrid Min-Max-Refined Fusion on PUMPD.

Fusion Combination	EER (%)
(Blue, Green)+(Red, NIR)	0.0151
(Blue, Green)+(NIR, Red)	0.0213
(Green, Blue)+(Red, NIR)	0.0212
(Green, Blue)+(NIR, Red)	0.0212
(Blue, Red)+(Green, NIR)	0.0302
(Blue, Red)+(NIR, Green)	0.0303
(Red, Blue)+(Green, NIR)	0.0333
(Red, Blue)+(NIR, Green)	0.0310
(Blue, NIR)+(Red, Green)	0.0212
(Blue, NIR)+(Green, Red)	0.0212
(NIR, Blue)+(Red, Green)	0.0304
(NIR, Blue)+(Green, Red)	0.0357

For anti-spoof attack, as faked palm has small difference between different spectra, the fused feature will be different with true palm, similar as the example shown in liveness detection by image level fusion.

Similar as Section 3.2.1.2, motion blur robustness is investigated. The accuracy achieved of feature level and hybrid fusion is listed in Table 3.15 and Table 3. 16. As shown in Table 3.15 and Table 3.5, the proposed feature level fusion could get better results than single spectrum on the motion blur database. Similarly, hybrid fusion gets better results than feature level fusion in most of cases.

Table 3.15 Verification Accuracy of Min-Max-Refined Fusion on PUMMBPD.

Fusion Combination	EER (%)
Blue, Green	0.1161
Blue, Red	0.1244
Blue, NIR	0.0484
Green, Blue	0.1212
Green, Red	0.1330
Green, NIR	0.0334
Red, Blue	0.1275
Red, Green	0.1301
Red, NIR	0.0826
NIR, Blue	0.0726
NIR, Green	0.0485
NIR, Red	0.0993

Table 3.16 Verification Accuracy of Hybrid Min-Max-Refined Fusion on PUMMBPD.

Fusion Combination	EER (%)
(Blue, Green)+(Red, NIR)	0.0332
(Blue, Green)+(NIR, Red)	0.0364
(Green, Blue)+(Red, NIR)	0.0334
(Green, Blue)+(NIR, Red)	0.0424
(Blue, Red)+(Green, NIR)	0.0424
(Blue, Red)+(NIR, Green)	0.0480
(Red, Blue)+(Green, NIR)	0.0364
(Red, Blue)+(NIR, Green)	0.0517
(Blue, NIR)+(Red, Green)	0.0395
(Blue, NIR)+(Green, Red)	0.0364
(NIR, Blue)+(Red, Green)	0.0483
(NIR, Blue)+(Green, Red)	0.0453

3.2.4 Matching Score Level Fusion

3.2.4.1 Score Level Fusion Scheme

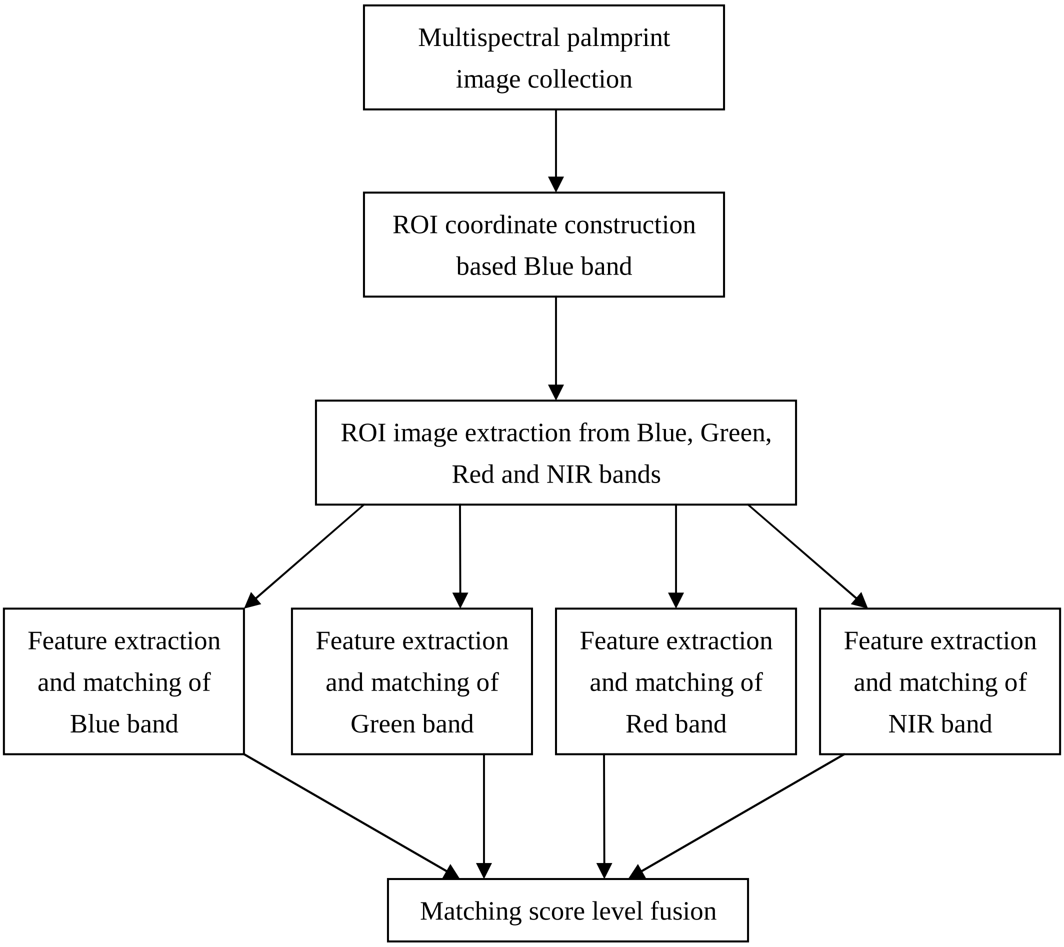

Figure 3.21 Framework of score level fusion.

The framework of score level fusion is illustrated in Fig. 3.21. Generally, more information is used, better performance could be achieved. However, since there is some overlapping of the discriminating information between different bands, simple sum of the matching scores of all bands may not improve much the final accuracy. Suppose there are k kinds of features (F_i^X, $i=\{1,2,...,k\}$). For two samples X and Y, the distance using simple sum rule is defined as:

$$d_{Sum}(X,Y)=\sum_{i=1}^{k} d(F_i^X, F_i^Y) \tag{3-10}$$

where $d(F_i^X, F_i^Y)$ is the distance for the i^{th} feature.

$$\begin{array}{l} F_1^{X_1}\ 1\ 1\ 1\ 1\ 1\ 0\ 1\ 0 \\ \qquad\quad 1\ 0\ 1\ 0\ 0\ 0\ 0\ 0\ F_2^{X_1} \end{array} \xrightarrow{F_1 \cup F_2} 1\ 1\ 1\ 1\ 1\ 0\ 1\ 0\ 0\ 0\ 0\ 0$$

$$\begin{array}{l} F_1^{X_2}\ 1\ 1\ 1\ 0\ 0\ 1\ 0\ 1 \\ \qquad\quad 0\ 1\ 0\ 1\ 0\ 0\ 0\ 0\ F_2^{X_2} \end{array} \xrightarrow{F_1 \cup F_2} 1\ 1\ 1\ 0\ 0\ 1\ 0\ 1\ 0\ 0\ 0\ 0$$

$$\begin{array}{l} F_1^{Y_1}\ 1\ 1\ 0\ 0\ 1\ 1\ 1\ 1 \\ \qquad\quad 1\ 1\ 1\ 1\ 0\ 0\ 1\ 1\ F_2^{Y_1} \end{array} \xrightarrow{F_1 \cup F_2} 1\ 1\ 0\ 0\ 1\ 1\ 1\ 1\ 0\ 0\ 1\ 1$$

Figure 3.22 An example of sum score fusion.

Fig. 3.22 shows an example of score level fusion by summation. There are two kinds of features ($F_i^X, i = \{1,2\}$) for three samples $\{X_1, X_2, Y_1\}$, where X_1 and X_2 belonging to the same class and Y_1 belongs to another class. By Eq. 3-10, we can get $d_{Sum}(X_1, X_2)$=9 and $d_{Sum}(X_1, Y_1)$=8. In fact, the true distances between X_1 and X_2, and X_1 and Y_1 without information overlapping should be 5 and 6, respectively. Because there is an overlapping part between the two features, it will be counted twice by using the sum rule (Eq. 3-10). Sometimes, such kind of over-computing may make the simple score level fusion fail as shown in the above example. For multispectral palmprint images, most of the overlapping features between two spectral bands locate on the principal lines as shown in Fig. 3.19. By using the sum rule (Eq. 3-10), those line features will be over-counted so that it may fail to classify two palms with similar principal lines.

From the above analysis, when a score level fusion strategy could reduce the overlapping effect, better verification results can be expected. The "U" operator in the set theory gives us a good hint, which is defined as follows:

$$X \cup Y = X + Y - X \cap Y \tag{3-11}$$

Based on Eq. 3-11, a score level fusion rule is defined which tends to minimize the overlapping effect on the fused score:

$$\begin{aligned} d_{F_1 \cup F_2}(X,Y) &= d(F_1) + d(F_2) - d(F_1 \cap F_2) \\ &= d(F_1^X, F_1^Y) + d(F_2^X, F_2^Y) - \frac{(d(F_1^X, F_1^Y) + d(F_2^X, F_2^Y))}{2} * P_{OP}(F_1, F_2) \end{aligned} \tag{3-12}$$

where $P_{OP}(F_1, F_2)$ is the overlapping percentage between two feature maps. Here two assumptions are made. First we assume that the overlapping percentage of two feature maps is nearly the same for different palms. There are two reasons for us to make this assumption. One is that the difference of overlapping percentage between different palms is relatively small, as can be seen in Table 3.17. The other one is that although $P_{OP}(F_1,F_2)$ can be computed for any given two feature maps, it will spend some computational cost and hence may be a burden in time demanding applications. Thus, to improve the processing speed, we fix $P_{OP}(F_1,F_2)$ as the average value computed from half of the database. The second assumption we made is that the overlapping is uniformly distributed across the feature map. Thus we can use $\frac{(d(F_1^X,F_1^Y)+d(F_2^X,F_2^Y))}{2}*P_{OP}(F_1,F_2)$ as an approximation distance in the overlapping part.

Table 3.17 The statistical percentage (%) of overlapping features between and among different spectral bands on half of the PUMPD.

Spectra	Mean Percentage	Standard Percentage
Blue and Green	77.1441	4.2342
Blue and Red	52.4086	6.0750
Blue and NIR	33.9168	5.0745
Green and Red	55.3237	5.6668
Green and NIR	35.7150	4.8323
Red and NIR	55.6474	5.6270
Blue, Green and Red	46.1191	5.9856
Blue, Green and NIR	28.7881	4.4930
Blue, Red and NIR	28.4338	4.7187
Green, Red and NIR	30.4006	4.7396
Blue, Green, Red and NIR	25.1862	4.4144

By using Eq. 3-12, the distances between X_1 and X_2, and X_1 and Y become 6.75 and 6, respectively. It is much closer to the true distance than using Eq. 3-10. Similarly, we could extend the fusion scheme to fuse more bands, e.g. 3 spectral bands as in Eq. 3-13:

$$\begin{aligned} d_{F_1\cup F_2\cup F_3}(X,Y) &= d(F_1^X,F_1^Y)+d(F_2^X,F_2^Y)+d(F_3^X,F_3^Y) \\ &-\frac{(d(F_1^X,F_1^Y)+d(F_2^X,F_2^Y))}{2}*P_{OP}(F_1,F_2) \\ &-\frac{(d(F_1^X,F_1^Y)+d(F_3^X,F_3^Y))}{2}*P_{OP}(F_1,F_3) \\ &-\frac{(d(F_2^X,F_2^Y)+d(F_3^X,F_3^Y))}{2}*P_{OP}(F_2,F_3) \\ &+\frac{(d(F_1^X,F_1^Y)+d(F_2^X,F_2^Y)+d(F_3^X,F_3^Y))}{3}*P_{OP}(F_1,F_2,F_3) \end{aligned} \tag{3-13}$$

Because different bands highlight different features of the palm, these features may provide different discriminate capabilities. It is intuitive to use weighted sum:

$$d_{Weight\,\mathrm{Sum}} = \sum_{i=1}^{n} w_i d_i \tag{3-14}$$

where w_i is the weight on d_i, the distance in the i^{th} band, and n is the number of total bands. Eq. 3-10 can be regarded as a special case of Eq. 3-14 when the weight is 1 for each spectrum.

Using the reciprocal of EER as weight is widely used in Biometric Systems [134]. If we take $d_i^{'} = w_i d_i$ as the normalized distance for band *i*, we can extend our proposed score level fusion scheme to weighted sum: multiply original distance with the weight for normalization, and then substitute the new distance into Eq. 3-12 or Eq. 3-13.

3.2.4.2 Experimental Results

Table 3.18 lists the accuracy results by four different fusion schemes, original weighted sum (w=1), proposed weighted sum (w=1), original weighted sum (w=1/EER) and proposed weighted sum (w=1/EER). Some findings could be obtained. Firstly, all fusion schemes can result in smaller EER than a single band except the fusion of Blue and Green (this is because the feature overlapping between them is very high), which validates the effectiveness of multispectral palmprint authentication. Secondly, using the reciprocal of EER as weight usually leads to better results than the equal weight scheme. Thirdly, the proposed fusion scheme, which could reduce the feature overlapping effect, achieves better results than the original weighted sum method. It can be verified that Eq. 3-12 can be rewritten as Eq. 3-15 and it is actually a weighted ($(1-P_{OP}(F_1,F_2))$) distance of Eq. 3-10.

$$\begin{aligned} d_{F_1 \cup F_2}(X,Y) &= d(F_1) + d(F_2) - d(F_1 \cap F_2) \\ &= d(F_1^X, F_1^Y)(1-P_{OP}(F_1,F_2)) + d(F_2^X, F_2^Y)(1-P_{OP}(F_1,F_2)) \\ &= (d(F_1^X, F_1^Y) + d(F_2^X, F_2^Y))(1-P_{OP}(F_1,F_2)) \end{aligned} \quad (3\text{-}15)$$

Table 3.18 Accuracy measurement comparison by different fusion schemes on PUMPD.

EER (%)	Original Weighted Sum (w=1)	Proposed Weighted Sum (w=1)	Original Weighted Sum (w=1/EER)	Proposed Weighted Sum (w=1/EER)
Blue, Green	0.0485	0.0485	0.0485	0.0485
Blue, Red	0.0243	0.0243	0.0212	0.0212
Blue, NIR	0.0151	0.0151	0.0152	0.0152
Green, Red	0.0272	0.0272	0.0212	0.0212
Green, NIR	0.0213	0.0213	0.0182	0.0182
Red, NIR	0.0151	0.0151	0.0152	0.0152
Blue, Green, Red	0.0272	0.0272	0.0236	0.0212
Blue, Green, NIR	0.0213	0.0182	0.0181	0.0151
Blue, Red, NIR	0.0151	0.0151	0.0152	0.0152
Green, Red, NIR	0.0152	0.0159	0.0152	0.0151
Blue, Green, Red, NIR	0.0182	0.0152	0.0152	0.0152

The best result is EER as low as 0.0151%. To the best of our knowledge, our multispectral palmprint database (250 subjects) is the largest database so far. The numbers of subjects in the databases of Ref. [93], Ref. [90], Ref. [91], Ref. [26] and Ref.

[92] are 7, 50, 100, 120 and 165, respectively. Among them, only the size of the database by Hao et. al. [92] is close with ours. However the best EER of their work is 0.50%, which is much worse than ours (0.0151%).

Although our fusion scheme verifies that the accuracy could be improved by fusing the features across spectral bands, sometimes the fusion of 3 or 4 bands is not better than the fusion of 2 bands. Certainly, it is possible that a better fusion scheme could be developed to more efficiently fuse the different features in different bands.

Table 3.19 lists the accuracy of the proposed fusion scheme on motion blur simulation database.

Table 3.19 Accuracy measurement comparison of the proposed fusion scheme on PUMMBPD.

EER (%)	Proposed Weighted Sum (w=1/EER)
Blue, Green	0.1030
Blue, Red	0.0601
Blue, NIR	0.0364
Green, Red	0.0429
Green, NIR	0.0272
Red, NIR	0.0394
Blue, Green, Red	0.0454
Blue, Green, NIR	0.0272
Blue, Red, NIR	0.0212
Green, Red, NIR	0.0182
Blue, Green, Red, NIR	0.0212

A good biometric system should be robust to spoof attacks. To test the anti-spoofing ability, a simple test is implemented. Here the test is based on inter-spectral distance, which is different from Section 3.2.1.2. A palmprint image in Blue band is printed on a paper, and then this paper is used as a fake palm to attack the system. For comparison, we apply this test to both the single-spectral (i.e. the Blue channel) system and multispectral system. For easy comparison, Table 3.20 lists the statistical value of genuine and impostor distance for each spectrum from the whole database and Table 3.21 lists the inter-spectral distance.

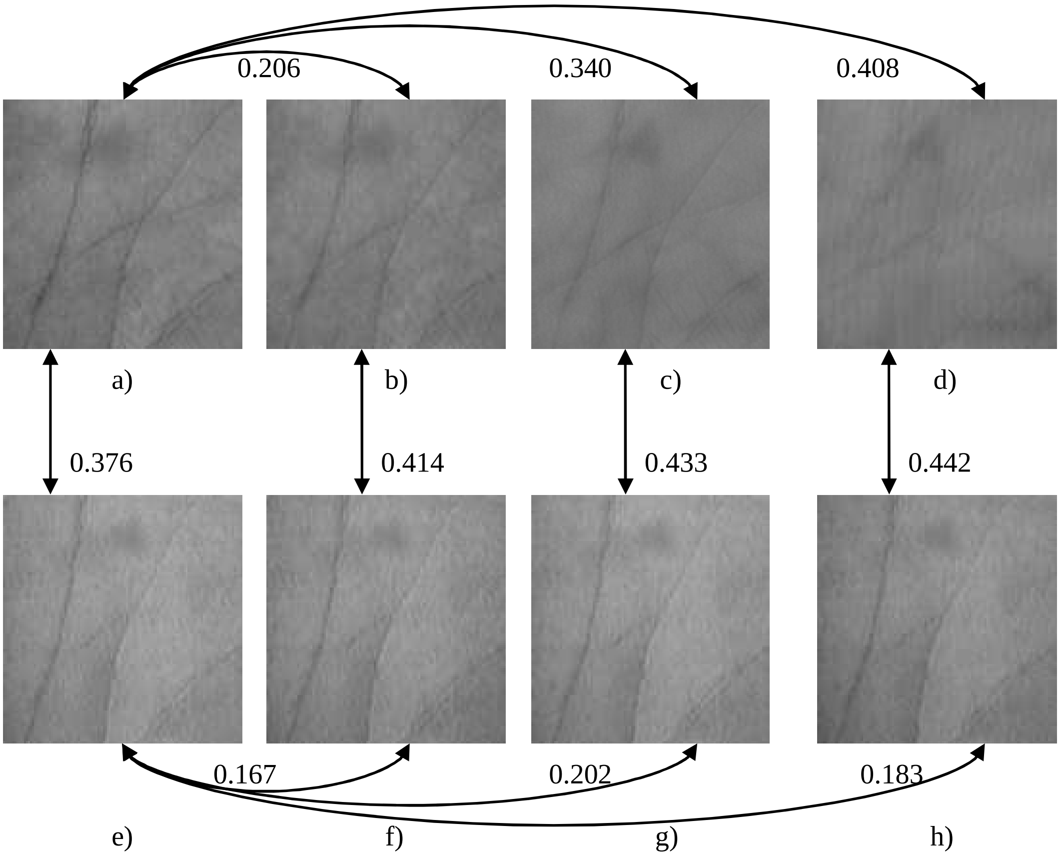

Figure 3.23 An example of anti-spoof test. a-d) are images of a true palm taken under Blue, Green, Red and NIR. e-h) are images of a fake palm taken under Blue, Green, Red and NIR. The distance between two images is showed on or near a double arrow curve.

As shown in Fig. 3.23, the faked palmprint is easy to pass the single-spectral system, the distance (0.376) between (a) and (e) is smaller than the mean impostor distance (0.459, refer to Table 3.20 please) and close to the verification threshold in our system. But it is hard to pass the multispectral system because the distances in other bands are big. For example, the distance (0.442) between (d) and (h) is close to the mean impostor distance (0.460) and far away from the verification threshold. Moreover, because the reflectance of the fake material (paper in this example) is different from that of the skin, the distance between Blue and NIR bands of the faked palm is very small compared with that of the true palm (refer to Table 3.21 please). Thus, this feature can be used for liveness detection to improve the robustness of our system.

Table 3.20 Statistic of intra-spectra distance of whole PUMMPD.

Spectrum	Mean of Genuine	Mean of Impostor
Blue	0.234	0.459
Green	0.237	0.459
Red	0.221	0.457
NIR	0.237	0.460

Table 3.21 Statistic of inter-spectral distance of whole PUMMPD.

Mean/ Minimal/ Maximal of Distance	Blue	Green	Red	NIR
Blue	0	0.126/ 0.069/ 0.302	0.269/ 0.129/ 0.404	0.384/ 0.273/ 0.470
Green		0	0.252/ 0.127/ 0.431	0.371/ 0.264/ 0.466
Red			0	0.246/ 0.148/ 0.384
NIR				0

3.2.5 Discussion and Conclusion

In the above sections, three different kinds of fusion methods have been discussed separately. Their pros and cons are discussed in this section. Some key values for original multispectral database and motion blur simulated database are listed in Table 3.22.

Table 3.22 Key values for three kinds of fusion.

	Image Level Fusion	Feature Level Fusion (Min-Max-Refined Fusion)	Score Level Fusion (Proposed Weighted Sum (w=1/EER))
Lowest EER for Two Spectra in Original Database (%)	0.0286	0.0182	0.0152
Lowest EER for Two Spectra in Motion Blur Database (%)	0.0788	0.0484	0.0272
Feature Size for Two Spectra Fusion (bits)	3072 (3*32*32)	5120 (5*32*32)	6144 (6*32*32)
(Best) EER for Four Spectra Fusion in Original Database (%)	0.0696	0.0151	0.0151
(Best) EER for Four Spectra Fusion in Motion Blur Database (%)	0.0757	0.0332	0.0212
Feature Size for Four Spectra Fusion (bits)	3072 (3*32*32)	10240 (5*2*32*32)	12288 (3*4*32*32)

From Table 3.22, several findings could be found. First, verification accuracy is related with feature length. Score level fusion has the longest feature size with best accuracy. Image level fusion has the shortest feature size and worse performance. Second, the score level fusion considers different features independently, it is more robust to the motion blur effect. Although image level fusion is sensitive to motion blur when the image sources are few, such as for two bands fusion, the accuracy drops from 0.0288% to 0.0788. This is mainly because the possibility of both images blur is high, thus the fused image is blur usually. While as the number of feature band increases, the probability of fused images blurred is low, the fused image could reduce the blur effect. Thus the accuracy does not change too much, for example, it drops from 0.0696% to 0.0757%. Third, as mentioned before, the proposed feature level fusion is difficult to extend to odd number of feature bands. There are two possible ways to address this kind of situation. Taking three bands, Blue, Green and Red, fusion as example, the first way is to use hybrid fusion scheme, first compute distance by feature level fusion on Blue and Green, and compute the distance by Red channel, then normalize the two distance by a given rule [94], finally fuse the two normalized distances; the second way is to over use a channel, compute distance by feature level fusion on Blue and Green, and Green and Red, then fuse the two distances.

In summary, score level fusion is more suitable for high security oriented applications. It does not have strict time limitation (time spending is related with feature length directly), image level fusion is more appropriated for real time application with fewer requirements on accuracy, and feature level fusion is applicable to applications with medium requirement on security and time spending.

Chapter 4. Empirical Study of Light Source for Palmprint Recognition

As an important member of the biometric characteristics, palmprint has merits such as robustness, user-friendliness, high accuracy, and cost-effectiveness. Because of these good properties, palmprint recognition has received a lot of research attention and many systems have been proposed. In the early stage, most works focus on offline palmprint images [5-7]. With the development of digital image acquisition devices, many online palmprint systems have been proposed. Based on the sensors used, there are mainly four types of online palmprint image acquisition systems [13]: digital scanners [14-21], video cameras [22-24], CCD (Charge Coupled Device) based palmprint scanner [12, 25-26] and digital cameras [27-31]. On the other hand, according to imaging conditions, these systems could be classified into three classes: digital scanners [14-21], camera with passive illumination [23-24 26, 28-31], and camera with active illumination [12, 22, 25, 27].

Desktop scanner could provide high quality palmprint images [14-21] under different resolutions. However, it suffers from the slow scanning speed [13] and it requires the full touch of whole hand, which may bring sanitary issues during data collection. Using camera with uncontrolled ambient lighting [23-24, 26, 28-31] does not have the above problems. However, the image quality may not be very good as the illumination lighting may change much so that the recognition accuracy may not be high enough. Because camera mounted with active light could collect image data quickly with good image quality and it does not require the full touch with the device, this kind of systems have been widely adopted [12, 22, 25, 27]. In these systems, the light source is a key component and there are some principles on the setting of lighting scheme [32]. However, to the best of our knowledge, no work has been done to systematically validate whether white light is the optimal light for palmprint recognition, in spite of the fact that all of these studies [12, 22, 25, 27] use white light source for palmprint imaging. To this end, this chapter discusses this problem through extensive experiments on a large multispectral palmprint database we established by the proposed multispectral palmprint acquisition device, as illustrated in Fig. 3.3.

As discussed in Section 2.2.3, there are five kinds of popular approaches on palmprint recognition: structural, statistical, texture coding, subspace learning and other methods. Different approaches focus on different kinds of features, for example, structural methods pay attention to principal lines and wrinkles [12], subspace learning methods use holistic expression for palmprint recognition [58], and texture coding schemes assign a feature code for each pixel in the palmprint [12]. Different illumination may enhance different palmprint features as the reflectance and absorbance of human skin relative to spectrum, for example, short wavelength light could enhance the line feature of palms, while long wavelength light could acquire some subcutaneous vein structure [132]. Thus, to get unbiased result for different illuminations, this chapter employs three different kinds of feature extraction methods, i.e. CompCode [52] (texture coding), wide line detection [45, 135] (structural method), $(2D)^2$PCA [136-137] (subspace learning method) and, to empirically study the light source selection for palmprint recognition.

Section 4.1 introduces the data collection and database. Section 4.2 briefly reviews the three methods in this chapter and Section 4.3 gives the experimental results. Finally section 4.4 discusses the findings and concludes.

4.1 Data Collection

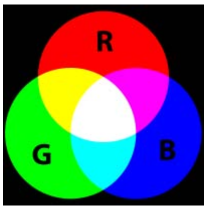

Figure 4.1 Additive Color Mixing: adding red to green yields yellow, adding all three primary colors together yields white.

It is known that red, green, and blue are the three primary colors, and the combination of them could result in many different colors in the visible spectrum as shown in Fig. 4.1. A multispectral palmprint data collection device which includes the three primary color illumination sources (LED light sources) is proposed, as introduced in Section 3.1. By using this device, we can simulate different illumination conditions. For example, when the red and green LEDs are switched on simultaneously, the yellow like light could be generated. Totally our device could collect palmprint images under seven different color illuminations: red, green, blue, cyan, yellow, magenta and white. Fig. 4.2 shows examples of the collected images under different illuminations. PUACPD (please refer to Section 1.4.3 for detail) is collected for recognition evaluation.

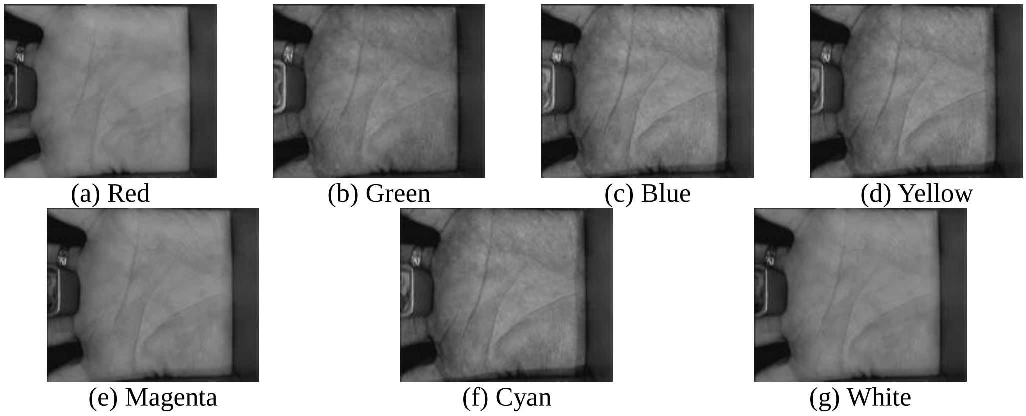

Figure 4.2 A sample of collected image of one palm with different illuminations.

After obtaining the multispectral cube, a local coordinate of the palmprint image is established [12] from the blue band (the ROI extraction accuracy on the other six bands is similar to blue one), and then a ROI is cropped from each band based on the local coordinate, Fig. 4.3 shows the extracted ROI from Fig. 4.2. For the convenience of analysis, we normalized these ROIs to a size of 128*128. To remove the global intensity and contrast effect, all images are normalized to have a mean of 128 and standard deviation of 20.

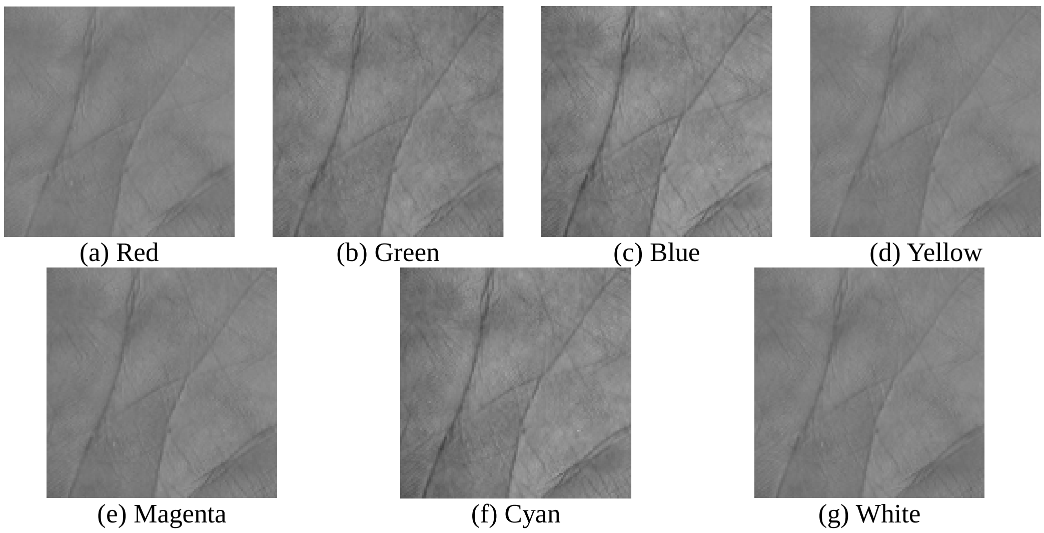

Figure 4.3 A sample of ROIs of one palm with different illuminations.

4.2 Review of feature extraction methods

4.2.1 Wide Line Detection

A palmprint image has mainly three kinds of features: principal lines (usually three dominant lines on the palm), wrinkles (weaker and more irregular lines) and crease (the ridge and valley structures like those in fingerprint) [12]. These principal lines and wrinkles could be extracted by a wide line detector directly [45, 135]. The thickness of the line is defined as:

$$L(x_0, y_0) = \begin{cases} g - m(x_0, y_0) \text{ if } m(x_0, y_0) < g \\ 0 \qquad\qquad \text{otherwise} \end{cases} \tag{4-1}$$

$$m(x_0, y_0) = \sum_{x_0 - r \le x \le x_0 + r,\, y_0 - r \le y \le y_0 + r} c(x, y, x_0, y_0) \tag{4-2}$$

$$c(x, y, x_0, y_0) = \omega_0 * \begin{cases} 0 \text{ if } I(x, y) > I(x_0, y_0) \\ 1 \text{ otherwise} \end{cases} \tag{4-3}$$

$$\omega_0 = \frac{\omega}{\sum_{x_0 - r \le x \le x_0 + r,\, y_0 - r \le y \le y_0 + r} \omega(x, y, x_0, y_0, r)} \tag{4-4}$$

$$\omega(x, y, x_0, y_0, r) = \begin{cases} 1 \text{ if } (x - x_0)^2 + (y - y_0)^2 \le r^2 \\ 0 \text{ otherwise} \end{cases} \tag{4-5}$$

where g is the geometric threshold and m is the weighed mask having similar brightness. ω is a circular constant weighing mask and ω_0 is the normalization of the circular mask.

To remove noise, a Gaussian smoothing is applied as a post-processing step. Then the response is binarized after thresholding:

$$\tilde{L}(x, y) = L(x, y) * g_\sigma(x, y) \text{ where } g_\sigma(x, y) = \frac{1}{2\pi\sigma^2} \exp(-\frac{x^2 + y^2}{2\sigma^2}) \tag{4-6}$$

$$B(x, y) = \begin{cases} 1 \text{ if } \tilde{L}(x, y) > t \\ 0 \text{ otherwise} \end{cases} \tag{4-7}$$

where σ is the scale of the Gaussian filter and t is a threshold. After binarization, the similarity between two palmprints is defined as the proportion of matched bits to the total bits of the two binary palmprint maps [45, 135]. As shown in Fig. 4.4, different parameters will generate different feature maps. In the experiments, we will compute the recognition accuracy on a group of parameters and select the best result of each illumination for final comparison.

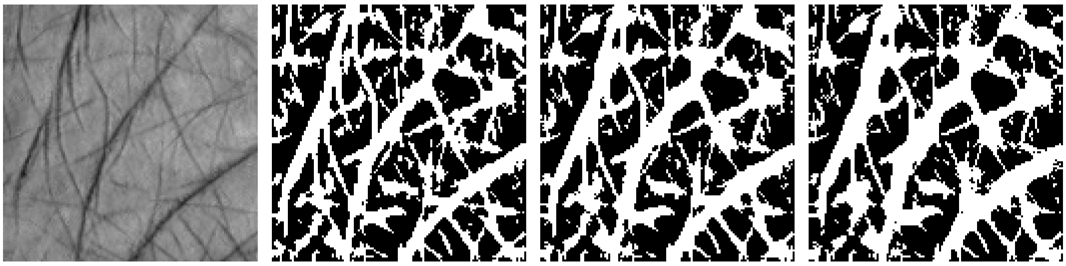

(a) A ROI sample (b) Extracted features by different parameters

Figure 4.4 A palmprint ROI sample and its extracted wide line features.

4.2.2 CompCode

As discussed in Section 3.1, the shape of Gabor filter is related with parameters, including ω and δ. If the shape of Gabor filter is changed, the extracted orientation map will change accordingly. Fig. 4.5 shows an example of the extracted orientation feature map, where different gray levels represent different orientation.

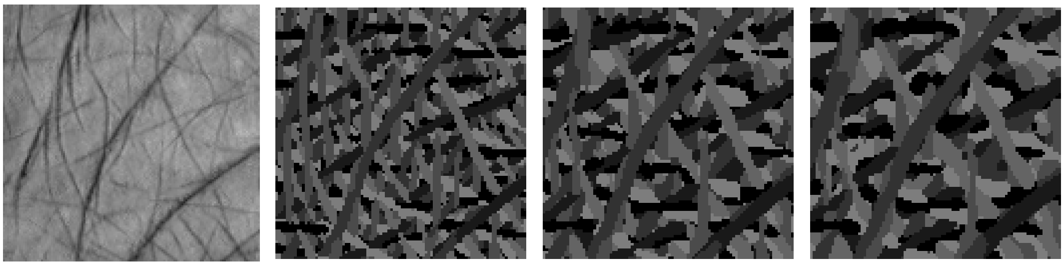

(a) A ROI sample (b) Extracted features by different parameters

Figure 4.5 A palmprint ROI sample and its extracted CompCode features.

4.2.3 $(2D)^2$PCA

Principal component analysis (PCA) is a widely used statistical analysis method, and $(2D)^2$PCA [136-137] is an extension of it, which can alleviate much the small sample size problem and better preserve the image local structural information. Suppose we have *M* subjects and each subject has *S* sessions in the training data set, i.e. *S* multispectral palmprint cube were acquired at different times for each subject. Then, we denote by X_{ms}^b (the original image matrix) the b^{th} band image for the m^{th} individual in the s^{th} session. The covariance matrices along the row and column directions are computed as:

$$G_1^b = \frac{1}{MS}\sum_{s=1}^{S}\sum_{m=1}^{M}(X_{ms}^b - \overline{X^b})^T(X_{ms}^b - \overline{X^b}), G_2^b = \frac{1}{MS}\sum_{s=1}^{S}\sum_{m=1}^{M}(X_{ms}^b - \overline{X^b})(X_{ms}^b - \overline{X^b})^T \quad (4\text{-}8)$$

where $\overline{X^b} = \frac{1}{MS}\sum_{s=1}^{S}\sum_{m=1}^{M} X_{ms}^b$.

The project matrix $V_1^b = [v_{11}^b, v_{12}^b, ..., v_{1k_1^b}^b]$ is composed of the orthogonal eigenvectors of G_1^b corresponding to the k_1^b largest eigenvalues, and the projection matrix $V_2^b = [v_{21}^b, v_{22}^b, ..., v_{2k_2^b}^b]$ consists of the orthogonal eigenvectors of G_2^b corresponding to the largest k_2^b eigenvalues. k_1^b and k_2^b can be determined by setting a threshold to the cumulant eigenvalues:

$$\sum_{j_c=1}^{k_1^b}\lambda_{1j_c}^b \Big/ \sum_{j_c=1}^{I_c}\lambda_{1j_c}^b \geq C_u, \sum_{j_r=1}^{k_2^b}\lambda_{2j_c}^b \Big/ \sum_{j_r=1}^{I_r}\lambda_{2j_c}^b \geq C_u \quad (4\text{-}9)$$

where $\lambda_{11}^b, \lambda_{12}^b, ..., \lambda_{1I_c}^b$ are the first I_c biggest eigenvalues of G_1^b, $\lambda_{21}^b, \lambda_{22}^b, ..., \lambda_{2I_r}^b$ are the first I_r biggest eigenvalues of G_2^b, and C_u is a pre-set threshold. For each given band b^{th}, the test image T^b is projected to $\widetilde{T^b}$ by V_1^b and V_2^b ($V_2^{bT} \times T^b \times V_1^b$), then Euclidean distance is used to measure the dissimilarity [136-137]. Fig. 4.6 shows the reconstructed image ($V_2^b \times \widetilde{T^b} \times V_1^{bT}$) by different C_u.

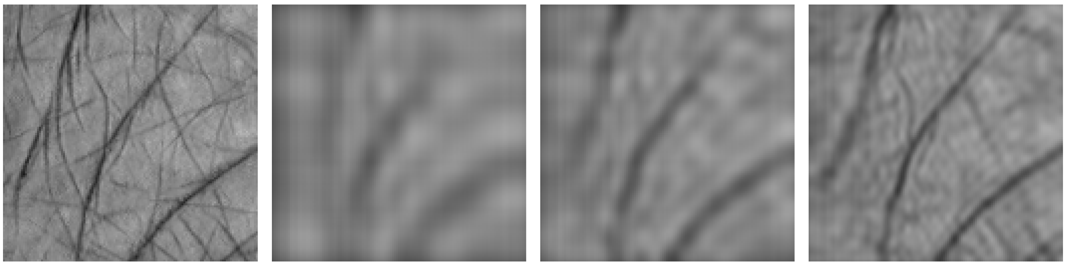

(a) A ROI sample (b) Extracted features by different parameters

Figure 4.6 A palmprint ROI sample with its reconstructed images.

4.3 Experimental Results

4.3.1 Palmprint Verification Results by Wide Line Detection

In this Chapter, PUACPD is used for recognition evaluation. To compute the verification accuracy for this section, each palmprint image is matched with all the other palmprint images in the database. A match is counted as a genuine if the two palmprint images are from the same palm; otherwise, it is counted as an impostor. The total number of matches is 17,997,000 and the number of genuine is 33,000. The EER is used to evaluate the accuracy.

As discussed in Section 4.2.1, there are four parameters which could influence the feature extraction, *r*, *t*, *g*, and σ. To reduce the possible parameter space, we fixed *g*=0.5 and *t*=0.1 [45, 135] and selected 5 different values for *r* and *t*, thus the total number of test settings is 25. The EER under different settings with different illuminations are plotted in Fig. 4.7 and the lowest EER for each light is listed in Table 4.1.

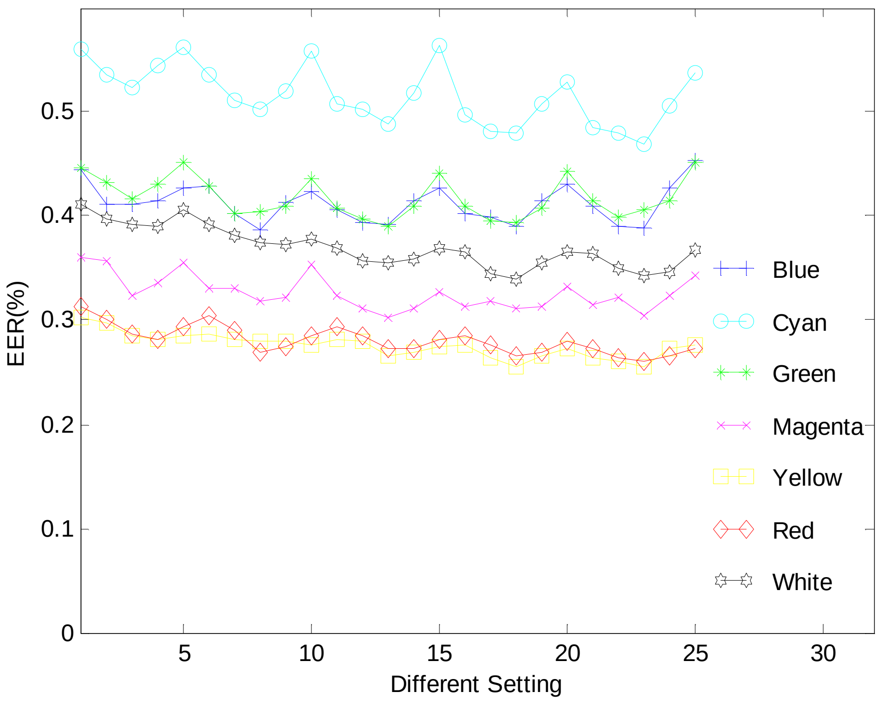

Figure 4.7 EER under different setting by Wide Line Detection.

Table 4.1 The lowest EER for each color by Wide Line Detection.

Color	EER (%)
Blue	0.3875
Cyan	0.4694
Green	0.3912
Magenta	0.3029
Yellow	0.2546
Red	0.2606
White	0.3396

4.3.2 Palmprint Verification Results by CompCode

As discussed in Section 4.2.2, there are two parameters, ω and δ could influence the extracted features. We selected 5 different values for ω and δ, respectively, and used the same test protocol as discussed in Section 4.3.1. The EER under different settings with different illuminations are plotted in Fig. 4.8 and the lowest EER for each light is listed in Table 4.2.

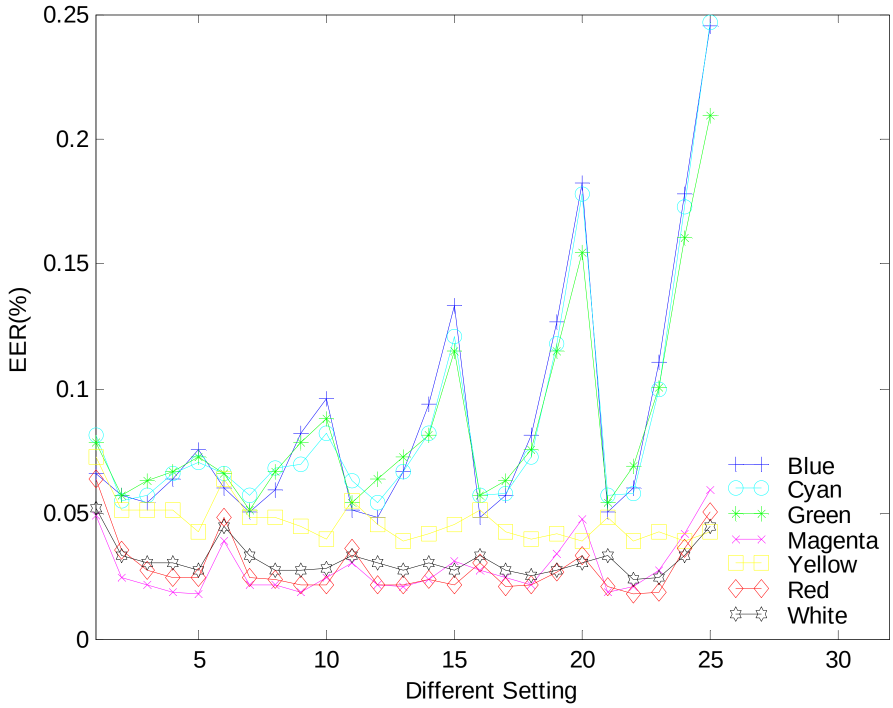

Figure 4.8 EER under different setting by CompCode.

Table 4.2 The lowest EER for each color by CompCode.

Color	EER (%)
Blue	0.0484
Cyan	0.0547
Green	0.0514
Magenta	0.0182
Yellow	0.0392
Red	0.0182
White	0.0241

4.3.3. Palmprint Identification Results by $(2D)^2$PCA

In this section, identification instead of verification is implemented. The whole database is partitioned into two parts, a training set and a test set. The training set is used to estimate the projection matrix and is taken as gallery samples. The test samples are matched with the training samples and the nearest neighborhood classification is employed. The ratio of the number of correct matches to the number of test samples, i.e. the recognition accuracy, is used as the evaluation criterion. To reduce the dependency of experimental results on training sample selection, we designed the experiments as follows. Firstly, the first three samples in the first session are chosen as the training set and the remaining samples are used as the test set. Secondly, the first three samples in the second session are chosen as training set, and the remaining samples are used as the test set. Finally, the average accuracy is computed.

As shown in Section 4.2.3, there is only one parameter, C_u, to control the feature extraction. The accuracy under different settings with different illuminations is plotted in Fig. 4.9 and the highest accuracy for each light is listed in Table 4.3.

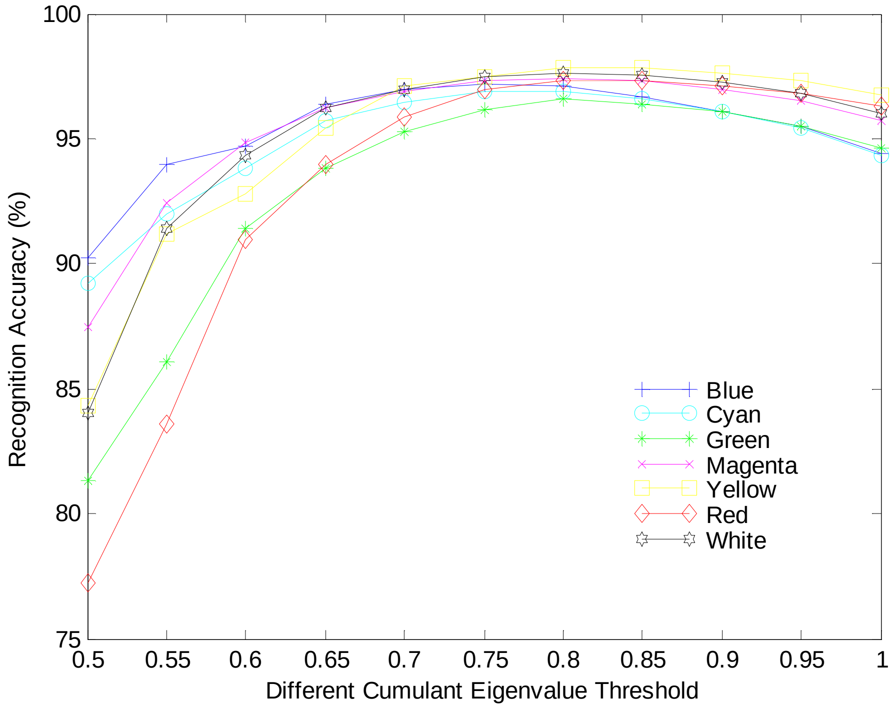

Figure 4.9 Recognition Accuracy under different C_u .

Table 4.3 The lowest EER for each color by $(2D)^2$PCA.

Color	EER (%)
Blue	97.2000
Cyan	96.8777
Green	96.6334
Magenta	97.4333
Yellow	97.8777
Red	97.3555
White	97.6334

4.4 Discussion and Conclusion

From Fig. 4.7-9 and Table 4.1-3, we could have three findings. First, no spectrum could compete with all the others for all settings. This is mainly because different light could enhance different features of palms, while these different features have different intensity distributions which are in favor of different parameters.

Second, among the three primary colors, Red has a little higher accuracy than blue and green. This is mainly because red could not only capture most of the palm line information, but also capture some palm vein structures as shown in Fig. 4.3. This additional palm vein information helps classify those palms with similar palm lines. It could also explain why the composite colors (magenta, yellow, white) could get better accuracy than cyan.

Last, white color could not get the best accuracy among the seven spectra. Yellow achieves the best result by the schemes of wide line detection and $(2D)^2$PCA, while magenta and red achieve the best result by the scheme of competitive coding. This finding could be explained as follows.

We assume that the imaged objects, i.e. palms, have a Lambertian surface [138]. The output of the monochrome CCD at pixel (x,y) can be given by:

$$I(x,y)=\int_{\lambda_{VS}}^{\lambda_{VE}}\rho(\lambda)\alpha(x,y,\lambda)s(x,y)e(\lambda)d\lambda \tag{4-10}$$

where $e(\lambda)$ is the spatially invariant illumination source of spectral distribution and λ represents the wavelength of the incident light. $\alpha(x,y,\lambda)$ denotes the albedo of the scene objects. $\rho(\lambda)$ is the spectral response of the sensor and $s(x,y)$ expresses the effect of the geometry. λ_{VS} and λ_{VE} are the limits of visible frequency spectrum. According to the additive color mixing, the intensity by the white illumination could be expressed by:

$$\begin{aligned}W(x,y)&=\int_{\lambda_{BS}}^{\lambda_{BE}}\rho(\lambda)\alpha(x,y,\lambda)s(x,y)e(\lambda)d\lambda+\int_{\lambda_{GS}}^{\lambda_{GE}}\rho(\lambda)\alpha(x,y,\lambda)s(x,y)e(\lambda)d\lambda\\&+\int_{\lambda_{RS}}^{\lambda_{RE}}\rho(\lambda)\alpha(x,y,\lambda)s(x,y)e(\lambda)d\lambda\approx B(x,y)+G(x,y)+R(x,y)\end{aligned} \tag{4-11}$$

where $\lambda_{BS}/\lambda_{GS}/\lambda_{RS}$ and $\lambda_{BE}/\lambda_{GE}/\lambda_{RE}$ are the limits of blue/green/red light frequency spectrum. $B(x,y)$, $G(x,y)$ and $R(x,y)$ represents the intensity by blue, green and red light, respectively.

As shown in Fig. 4.3, the palmprint images under blue and green illumination are more similar to each other than to the image under red illumination. A quantitive image quality index, complex wavelet structural similarity index (CW-SSIM) [121-122], is used here.

CW-SSIM is defined to measure the similarity of two images on wavelet frequency domain:

$$\tilde{S}(\mathbf{c}_x,\mathbf{c}_y)=\frac{2\left|\sum_{i=1}^{N}c_{x,i}c_{y,i}^{*}\right|+K}{\sum_{i=1}^{N}|c_{x,i}|^2+\sum_{i=1}^{N}|c_{y,i}|^2+K} \tag{4-12}$$

where c_x and c_y are the complex wavelet coefficents. In implementing the complex wavelet transform, a complex version of the “steerable pyramid” transform [139], which is a type of redundant wavelet transform that avoids aliasing in subbands, is used here.

c^* denotes the complex conjugate of c and K is a small positive constant. It has been shown that the CW-SSIM index is insensitive to luminance and contrast changes as well as small translation, rotation and distortion [121-122].

Eq. 4-12 could be rewritten as:

$$\tilde{S}(\mathbf{c}_x, \mathbf{c}_y) = \frac{2\sum_{i=1}^{N} |c_{x,i}||c_{y,i}| + K}{\sum_{i=1}^{N} |c_{x,i}|^2 + \sum_{i=1}^{N} |c_{y,i}|^2 + K} \cdot \frac{2\left|\sum_{i=1}^{N} c_{x,i} c_{y,i}^*\right| + K}{2\sum_{i=1}^{N} |c_{x,i}||c_{y,i}| + K} \tag{4-13}$$

Fig. 4.10 illustrates the similarity computation procedure. The first component in the right hand of the above equation is completely determined by the magnitudes of the coefficients. The maximum value 1 is achieved if and only if $|c_{x,i}| = |c_{y,i}|$ for all values of i. The second component is fully determined by the consistency of phase changes between $\mathbf{c}_x$ and $\mathbf{c}_y$. It achieves the maximum value 1 when the phase difference between $c_{x,i}$ and $c_{y,i}$ is a constant for i. And it is shown that the second component is a better measure of image structural similarity of palmprint images because the structural information of local image features is mainly contained in the relative phase patterns of the wavelet coefficients and a constant phase shift of all coefficients does not change the structure of local image features [120].

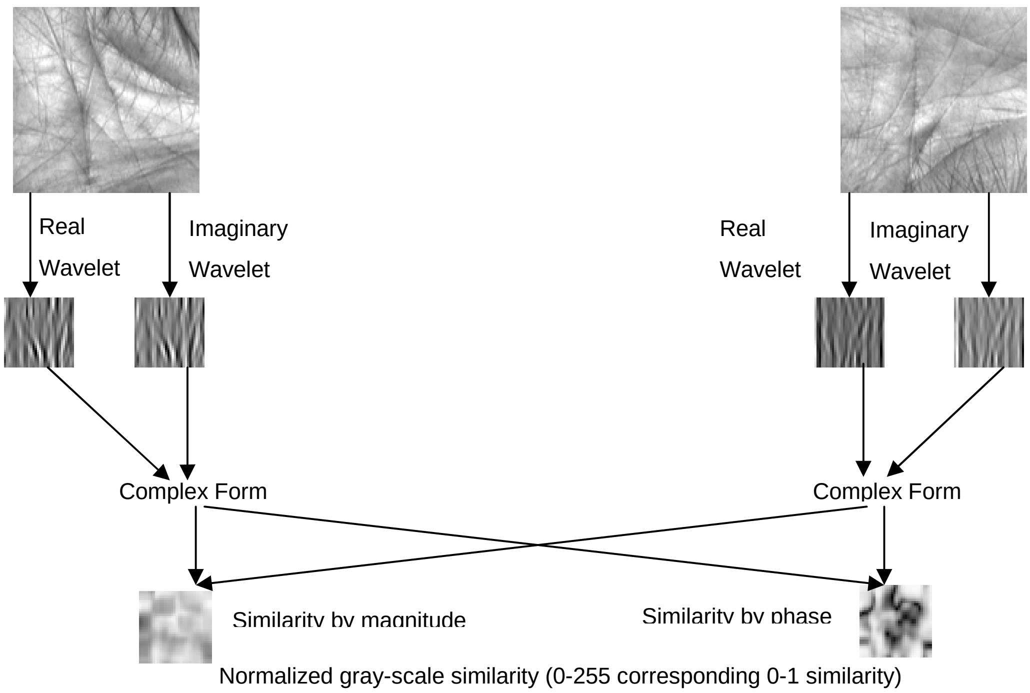

Figure 4.10 CS-SSIM computation procedure.

The modified CW-SSIM is defined as:

$$\tilde{S}_d(\mathbf{c}_x, \mathbf{c}_y) = \frac{\left|\sum_{i=1}^{N} c_{x,i} c_{y,i}^*\right| + K}{\sum_{i=1}^{N} |c_{x,i}||c_{y,i}| + K} \tag{4-14}$$

The average of CW-SSIM on three primary colors is shown in Table 4.4. It further validates that blue and green collect much redundant information, as the average similarity between blue and green is 0.95, while the average similarity between blue and red, and green and red are 0.83. The redundancy makes white color fail to capture more information than the yellow or magenta color, and sometimes the accuracy drops a little. This is also consistent with the finding of Fratric and Ribaric [140], fusion of blue and red channels gets better results than fusion of three channels.

Table 4.4 Average of CW-SSIM.

CW-SSIM	Blue	Green	Red
Blue	1	0.95	0.83
Green		1	0.83
Red			1

Palmprint recognition has been attracting lots of research attention in the past decade and many data collection devices have been proposed. For good image quality and high data capture speed, using cameras mounted with active lighting sources is the most popular device configuration. Almost all existing devices use white light as the illumination source but there was no systematic analysis on whether the white light is the optimal light source for palmprint recognition. This chapter made such an effort on answering this problem by establishing a large multispectral palmprint database using our developed device. With the database we empirically evaluated the recognition accuracies of palmprint images under seven different colors by three different methods. Our experimental results showed that the white color is not the optimal color for palmprint recognition and the yellow or magenta color could achieve higher accuracy than the white color.

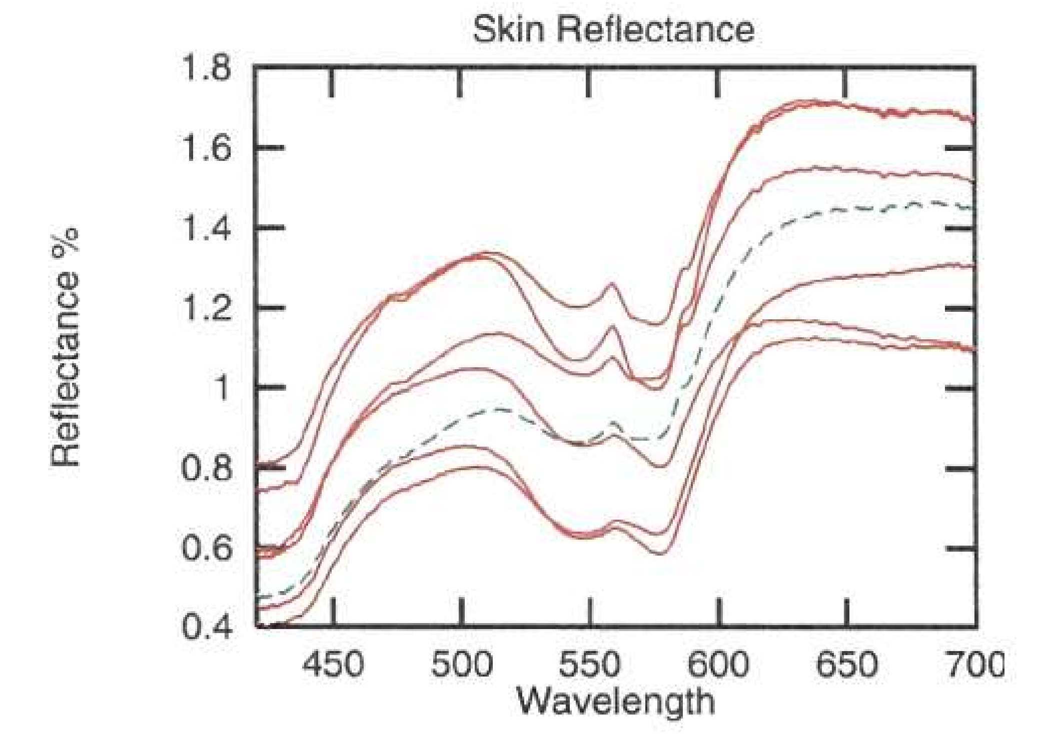

Figure 4.11 Skin reflectance of different subjects. [132]

However, so far our data were collected from East Asian residents (more specifically Chinese) only. Since the palm spectral properties of different groups may be different, as shown in Fig. 4.11, the finding of this work may not valid for other groups. In the future, more samples from other groups will be collected to investigate the best illumination conditions for palmprint recognition.

Chapter 5. Feature Band Selection for Online Multispectral Palmprint Recognition

Chapter 3 shows an apparatus and methods for multispectral palmprint recognition. The experimental results show that fusion of different spectra could improve the recognition accuracy significantly. Such as score level fusion of Blue (EER: 0.0515%) and NIR (EER: 0.0396%) could get much lower EER, 0.0151% (Refer to Table 3.19). Furthermore, examples show that liveness detection could be applied by analyzing multispectral images. Thus, the main disadvantage of traditional palmprint recognition could be addressed by multispectral imaging. Similar researches on fingerprint [87], face [88, 153], and iris [152] also show the superiority of multispectral imaging.

However, the two underlying key issues need to be addressed well before wide application of multispectral palmprint recognition. First, how many spectra are enough for discriminating different palms? Usually, more feature bands provide more information, thus higher accuracy could be expected. On the other hand, more feature bands require high cost on feature extraction and matching. Furthermore, because of redundancy between different spectra, more information may fail to increase the accuracy sometime. For example, score level fusion of Blue, Green and NIR get EER 0.0151% which is the same as that of Blue and NIR, 0.0151% (Refer to Table 3.19). Therefore, it is necessary to determine an optimal number of feature bands in multispectral palmprint system design. To our best knowledge, there are no public reports on this topic for biometric research. Second, how to choose these representative spectra for a given number of feature bands? After determining the number of feature bands, a group of bands could be selected by some rules, such as divergence [153], mutual information [154], and entropy [155]. The bands could also be found through exhaustive searching.

This chapter focuses on the first key issue. A clustering based method to determine the number of feature band from hyperspectral palmprint database is proposed. Section

5.1 introduces the data collection of hyperspectral palmprint cube. Section 5.2 reports the spectral *k*-means clustering algorithm and Section 5.3 shows the validation by verification experiment.

5.1 Hyperspectral Palmprint Cube Collection

To discover the optimal number of feature band for multispectral palmprint recognition, hyperspectral imaging [156] is used here. Hyperspectral imaging is a widely used technique in remote sensing [157]. The definition between hyperspectral and multispectral is usually defined as the number of spectral bands. Fig. 5.1 shows the difference between hyperspectral and multispectral imaging. Hyperspectral data could be a set of contiguous bands while multispectral data is a set of discrete bands.

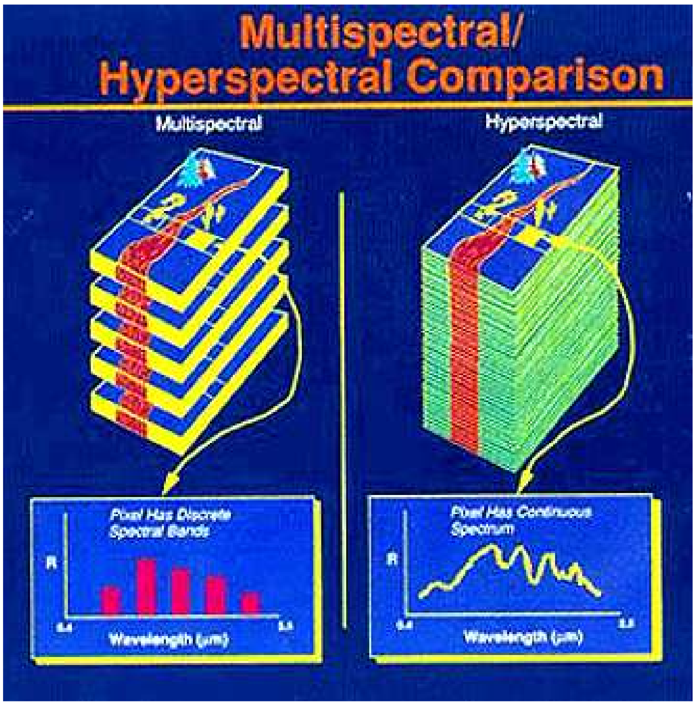

Figure 5.1 Hyperspectral vs Multispectral. [156]

A hyperspectral imaging system is set up to collect the palmprint images in consecutive spectral bands. The key components of the system include a Liquid Crystal Tunable Filter (LCTF), a high quality CCD, and two halogen lights.

The LCTF, model TOF-VIS, is made by Meadowlark Inc. Fig. 5.2 shows the LCTF with its transmission of different wavelengths. Its polarized transmission range is from 420nm-1100nm and its tuning resolution is 0.1nm. The full width at half max is 5nm, thus the object (i.e. palm) will be imaged at 69 spectral bands with a step-length of 10nm over spectrum range to maximize the image independence and to get higher spectral resolution. Although, there is correlation between different wavelengths which is difficult to be removed, the motivation of the chapter is to find minimal number of feature bands to fully represent the whole spectrum information.

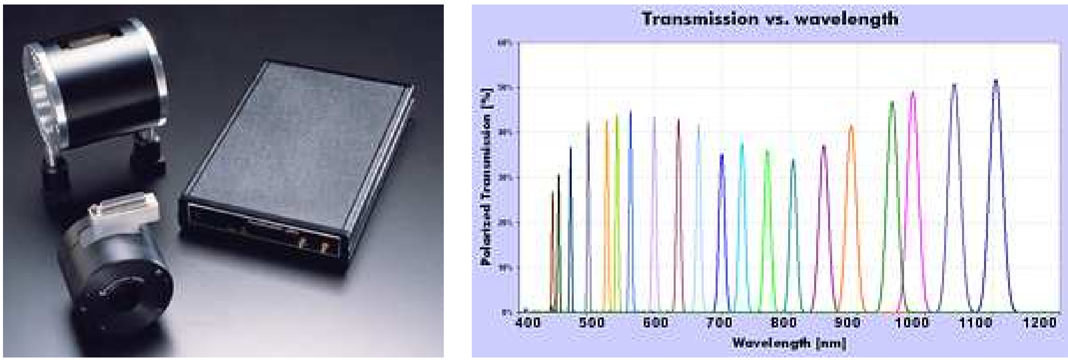

(a) (b)

Figure 5.2 LCTF with its transmission property. (a) TOF-VIS LCTF; (b) transmission vs wavelength.

A high quality CCD, Sensicam em made by the cooke corporation, is chosen in this work. Its resolution is 1004*1002 pixels. The spectral range is from 290nm to 1100nm. Fig. 5.3 shows the CCD with its spectral characteristic curve.

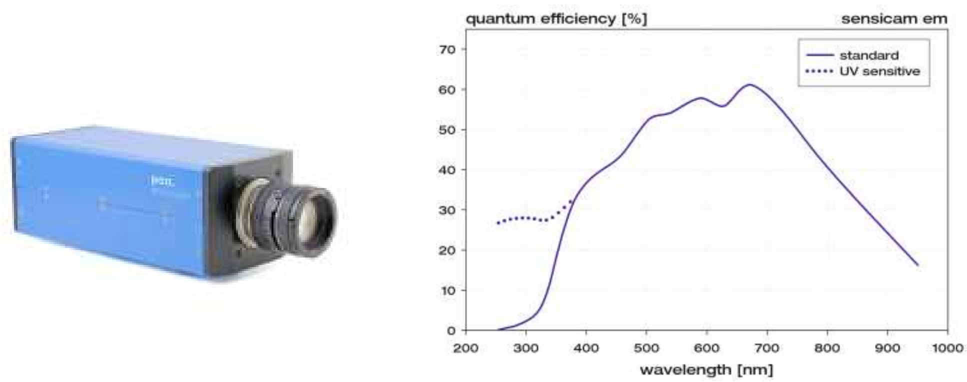

(a) (b)

Figure 5.3 CCD with its sensitivity curve. (a) Sensicam em CCD; (b) quantum efficency vs wavelength.

To provide uniform and strong enough illumination, two 500W Osram halogen lights as shown in Fig. 5.4 are selected.

Figure 5.4 500W Osram halogen light.

Fig. 5.5 illustrates the hyperspectral palmprint cube collection setting. In data collection, the users are asked to put their palms on the panel in front of the LCTF with the halogen lights power on. Several pads are used to reduce the degree of freedom of the palm. A hyperspectral image cube (with dimension 1004*1002*69) of the palm can be collected in a short time. PUHPD (please refer to Section 1.4.4 for detail) is collected for feature band selection.

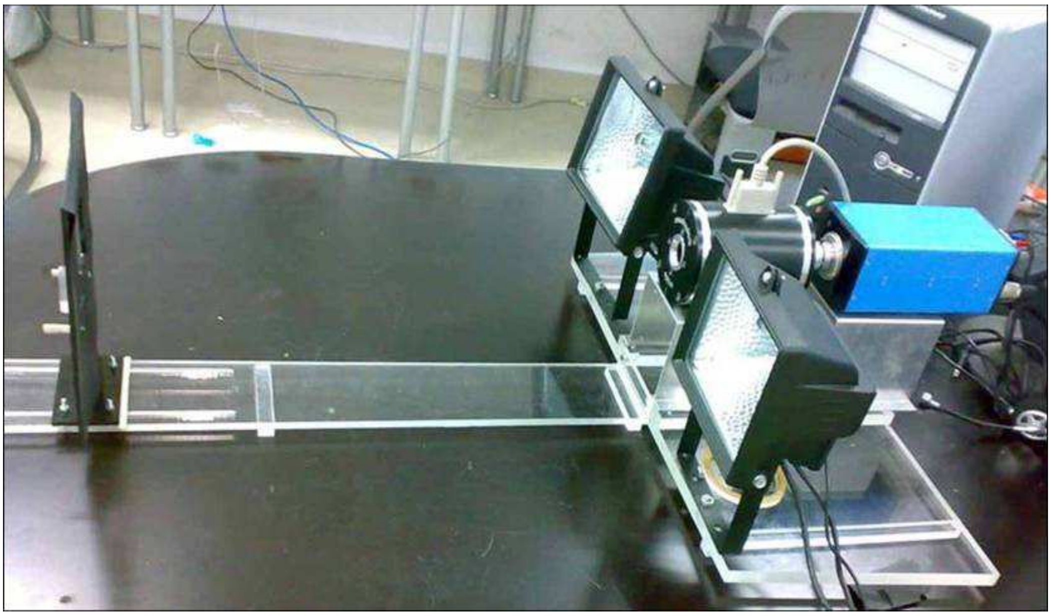

Figure 5.5 The hyperpsectral palmprint imaging system.

Fig. 5.6 shows partial of the hyperspectral palmprint cube.

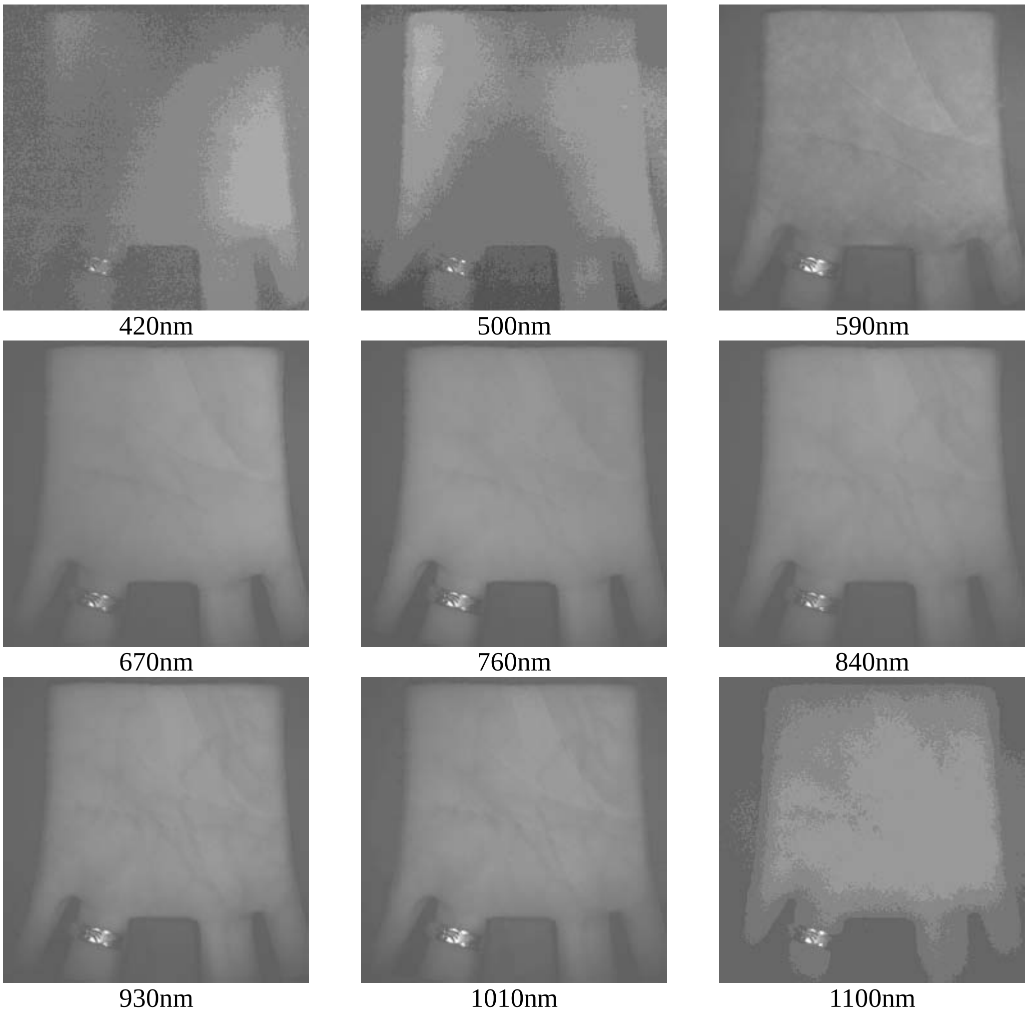

Figure 5.6 Partial of a sample of hyperspectral palmprint cube.

After obtaining the hyperspectral cube, a local coordinate of the palmprint image is established [12] in the center band (760nm), and then a ROI is cropped from each band based on the local coordinate. Fig. 5.7 illustrates the ROIs sample. For the convenience of analysis, these ROIs are normalized to a size of 128*128. To reduce the intensity effect, the ROIs are converted to have a mean intensity of 128 with a standard deviation of 20. As shown in Fig. 5.7, because of the low transmission of LCTF at short wavelength (please refer to Fig. 5.2), the image quality of the first several bands is not good. Meanwhile, since the CCD's response is not high enough at long wavelength (please refer to Fig. 5.3), the image quality at the last several bands are not good neither.

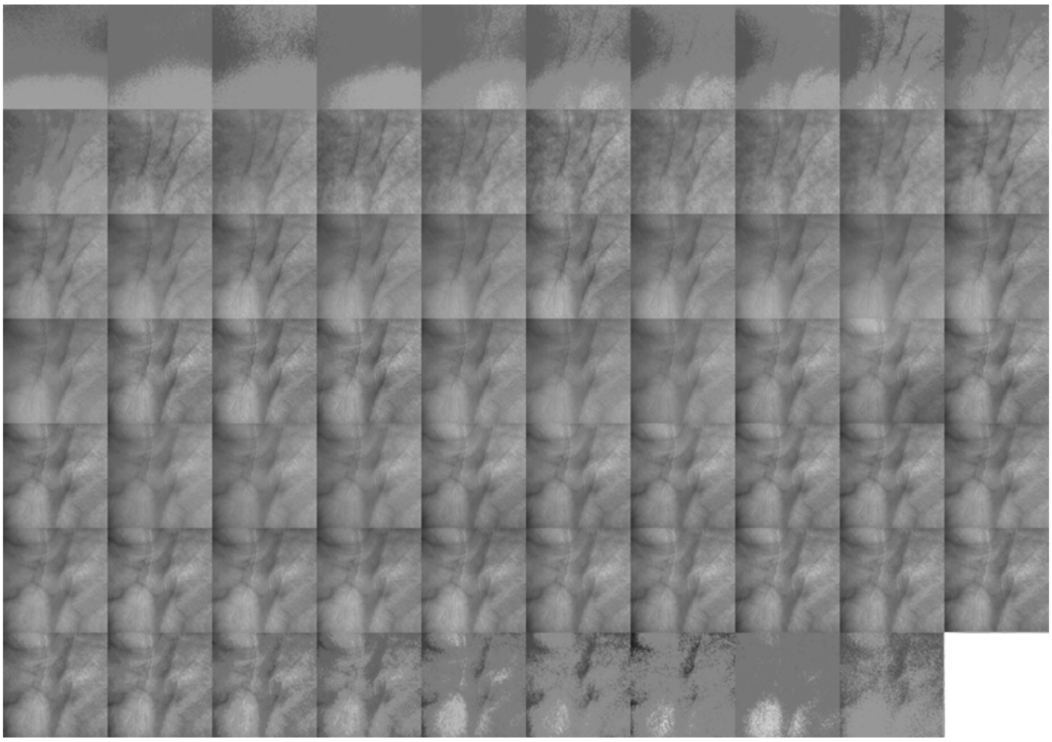

Figure 5.7 The ROIs extracted from sample of Figure 5.6. From left to right, top to down, the wavelength is increasing from 420nm to 1100nm with 10nm interval.

5.2 Feature Band Selection by Clustering

5.2.1 Review of *K*-Means Clustering

K-means clustering algorithm [158] is a basic and well known technique in pattern recognition. During the clustering, some points are clustered into separated classes or clusters according to the given clustering criterion. Fig. 5.8 shows an example of *k*-means. Fig. 5.8a shows three clusters which are generated by three separate Gaussian distribution. As *k* is a critical input parameter, different values will generate different clustering results. Fig. 5.8b-d show the clustering results for *k*=2, k=3 and *k*=4, respectively.

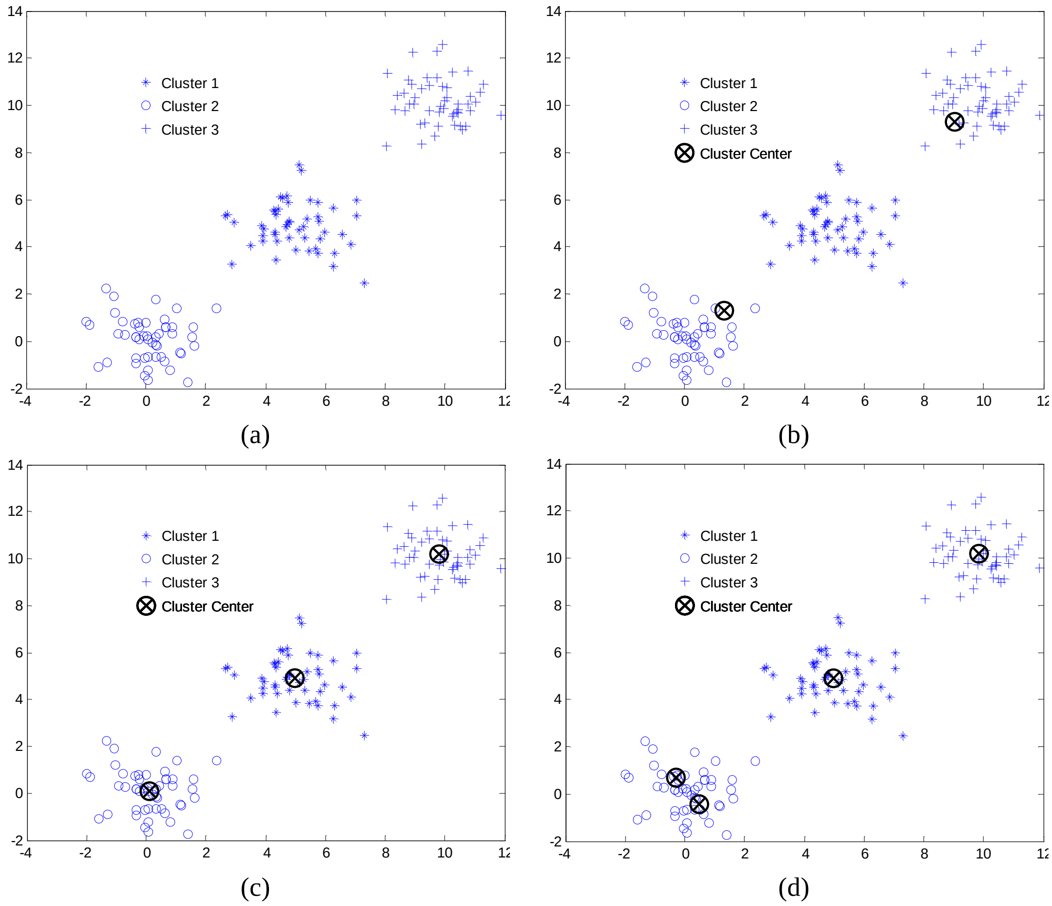

Figure 5.8 (a) Original data; (b) *K*-means result, *k*=2; (c) *K*-means result, *k*=3; (d) *K*-means result *k*=4.

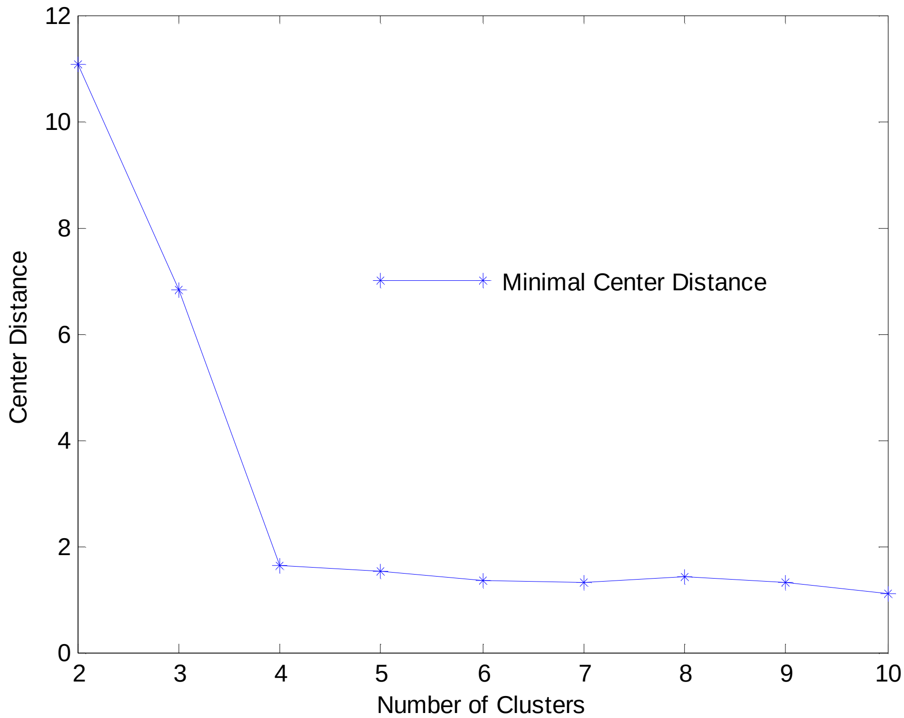

Figure 5.9 Number of clusters vs minimal center distance.

When the k is smaller or equal to the true number of clusters, the center distance is very big; while the k is larger than the true number of clusters, one cluster will be split into small clusters, the center distance becomes smaller and stable. The minimal center distance is defined as:

$$d_{\min}^{k} = \min_{\substack{1 \le i \le k \\ 1 \le j \le k \\ i \ne j}} (d_{i,j}) \tag{5-1}$$

$$d_{i,j} = d(c_i, c_j) \tag{5-2}$$

where d is Euclidean distance and k is the number of clusters.

Fig. 5.9 shows the $d_{\min}^{k}$ for different k values. As illustrated by Fig. 5.9, the distance drops quickly from k=2 to k=3. When k is bigger than 3, the distance changes slowly. The example shows that k-mean clustering could be used to discover the true number of clusters. Based on this finding, a spectral k-means clustering algorithm is proposed in the following.

5.2.2 Proposed Spectral *K*-Means Clustering

Based on the finding in Section 5.2.1, a spectral k-means clustering algorithm is proposed. Suppose we have N hyperspectral palmprint cubes with B spectrum, as the training set, Fig. 5.10 shows the pseudo-code of the algorithm:

1. Randomly get k initialized centers (wavelengths), x=0;
2. For any wavelength j (j=1,2,…,B), compute the distance between the wavelength with k centers, here the distance is compute as:

   $$D_{i,j} = \sum_{n=1}^{N} d_{i,j}^{n} = \sum_{n=1}^{N} d^{n}(c_i, w_j), i = 1, 2, ..., k$$

   where c is the center wavelength, w_j is the given wavelength, and d is the CW-SSIM distance defined in Section 4.4. x=x+1;
3. For each center, find the wavelengths which have the minimal distance among n centers. There are k clusters of wavelengths:

   $S_i = \{ j \mid \arg\min_i D_{i,j} = i \}, i = 1, 2, ..., k$
4. For any cluster, find the wavelength which has the minimal average distance with the remaining wavelengths in the cluster, this wavelength is updated as the new center:

   $c_i^{'} = \arg\min_{m \in S_i} \sum_{l=1}^{B} D_{l,m}, l \ne m, l \in S_i$
5. If the centers are not changed or x=T (T is a predefined iteration threshold), stops; otherwise, goes to step 2.

Figure 5.10 Pseudo-code of the proposed spectral k-means clustering.

In this thesis, N=2280, B=54 (The first 10 and last 5 feature bands are removed due to low signal to noise ratio as discussed before. The remaining 54 bands are 520nm-1050nm, with 10nm interval.) and T=100.

Because there is possibility that the clustering ends at local minimal instead of global minimal, for a given k, the clustering runs 1,000 times and the most frequent cluster centers are kept as the final result for the given k. Similar as Fig. 5.9, Fig. 5.11 shows minimal center distance for different numbers of clusters.

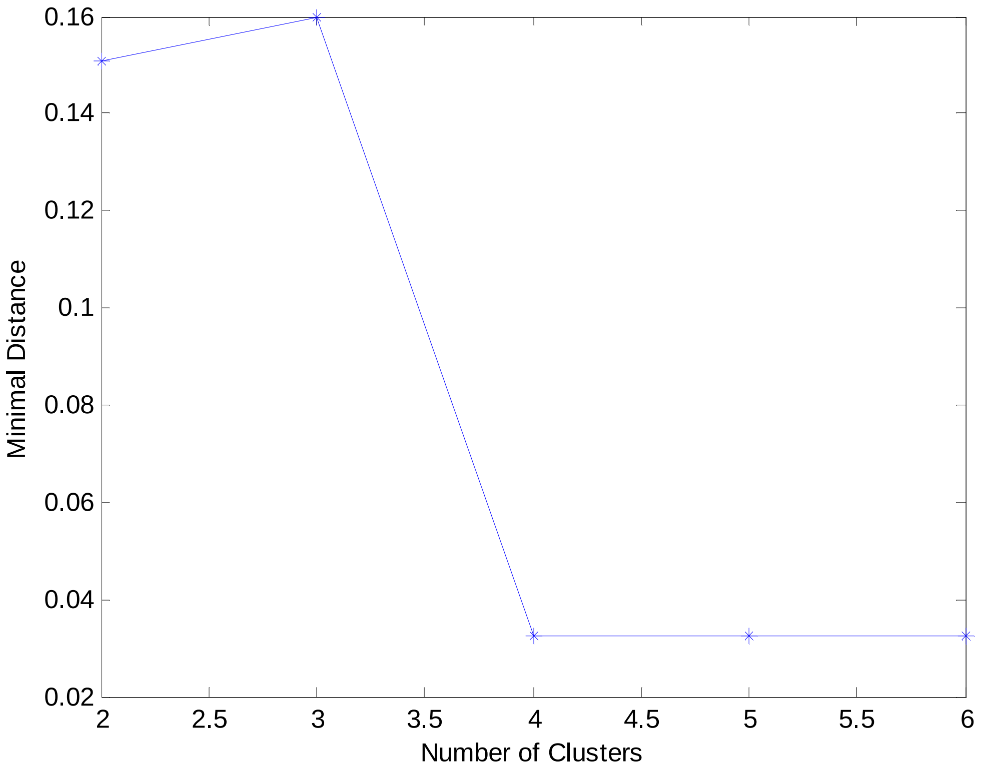

Figure 5.11 Minimal distance vs k.

Fig. 5.11 shows that three clusters may be enough to represent the 54 feature bands. The k=3 cluster result is listed in Table 5.1 and the distance map between different wavelength is plotted in Fig. 5.12. As can be seen from Fig. 5.12, there are roughly three dark blocks. According to the spectrum definition [159], the three clusters could be roughly named as visible spectrum without red, red spectrum and NIR spectrum.

Table 5.1 Clustering Result of spectral k-mean for k=3.

Cluster	Wavelengths
1	520 530 540 550 560 570 580 590 600 610
2	620 630 640 650 660 670 680 690 700 710 720 730 740 750 760 770 780
3	790 800 810 820 830 840 850 860 870 880 890 900 910 920 930 940 950 960 970 980 990 1000 1010 1020 1030 1040 1050

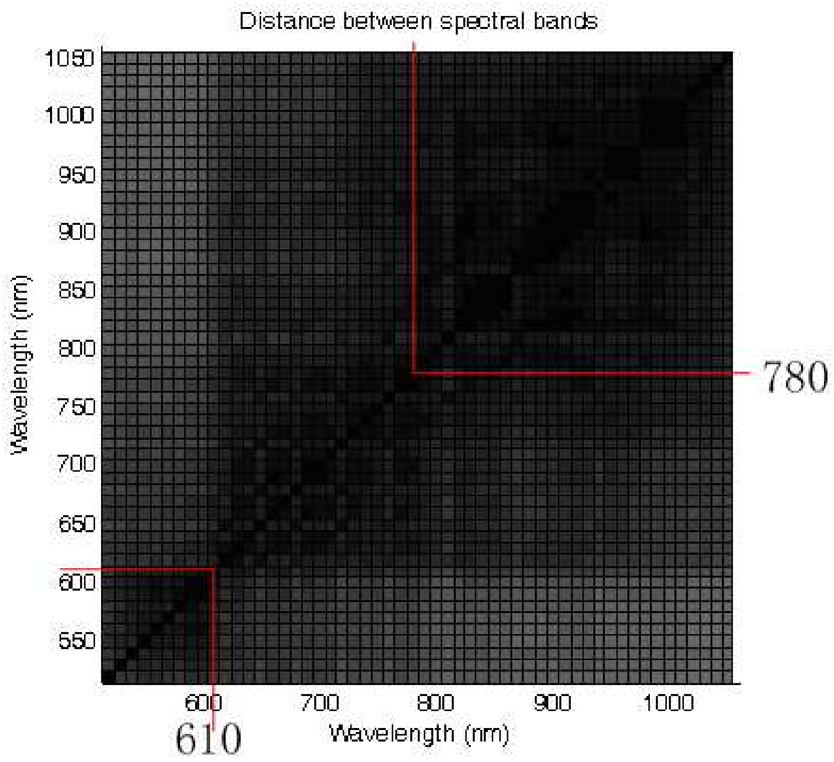

Figure 5.12 Distance map between different feature bands. The distance is convert from [0,1] to [0, 255] for display.

5.3 Experimental Validation

To demonstrate whether there is the optimal number of feature bands, verification experiment is implemented on PUHPD to validate it. Here, CW-SSIM based verification is used as it is less sensitive to scale, rotation and translation variation for palmprint verification [121].

One cube of each palm in the first session is randomly selected as the gallery sample, and all the cubes in the second session are used as probe samples. For any feature band, the image distance between each sample in the gallery set and sample in the probe set is computed. Totally, there are 1,000,160 (380*2632) matching distances for each feature band. Among them, 2,632 distances are genuine matching distances while the remaining are impostor matching distances. To get unbiased result with training gallery selection, the gallery set is selected three times independently. Then, one cube of each palm in the second session is randomly selected as the gallery sample, and all the cubes in the first session are used as probe samples. We use the same test protocol, for each wavelength, and get 991,040 (380*2608) matching distances for each feature band. Among them, 2,608 distances are genuine matching distances. Similarly, the gallery set is selected three times independently. Thus, totally six verification trials are implemented. In the following, the average of the six trials is listed as experimental results. Fig. 5.13 illustrates the EER with different wavelengths. The lowest EER is achieved by 790nm with EER=0.2220%. The error rate is much larger than the reported result in Section 4. This is caused by two reasons, first since the user is asked to put their palm vertically rather than horizontally, the degree of freedom is much higher than the traditional palmprint data collection; second, to speed up the comparison and reduce the feature size, the image is decomposed into 6 orientations rather than 16 orientations [120] in complex wavelet of CS-SSIM.

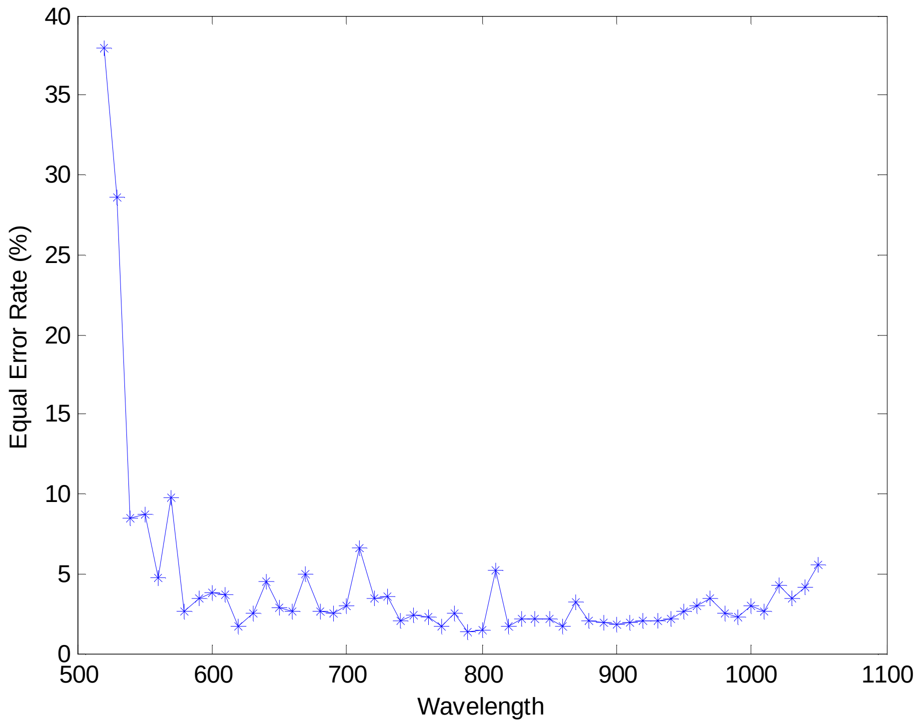

Figure 5.13 Wavelength vs EER.

To find the optimal combination for a given number of feature bands, many algorithms could be used to search for the combination, such as divergence [153], mutual information [154], and entropy [155]. Here, exhaustive search is implemented as it has less possibility to miss the true optimal combination. Sum score level fusion [94] is used as the fusion technique on the dataset. The lowest EER for each combination is listed in Table 5.2.

Table 5.2 Fusion result for different number of feature bands.

Number of feature bands	Optimal Combination	EER (%) (Mean±Std)
1	790nm	0.2220±0.0652
2	580nm, 770nm	0.1039±0.0431
3	580nm, 760nm, 990nm	0.0780±0.0344
4	580nm, 620nm, 760nm ,940nm	0.0727±0.0430

Table 5.2 shows more feature bands, and higher accuracy. Such as, fusion of 2 bands could reduce the EER from 0.222% to 0.1039%. However, the improvement from

3 bands to 4 bands is very small, only 0.0053%. Using statistical analysis [160], the difference between fusion of 4 bands and 3 bands is not statistically significant. And as shown in Table 5.1, 580nm, 760nm and 990nm come from three different clusters. These findings are consistent with the findings in the above section.

5.4 Discussion and Conclusion

In this chapter, a spectral k-means clustering algorithm is proposed to cluster hyperspectral palmprint cubes. The clustering could be used to determine an optimal number of feature bands. The result shows that three feature bands may be enough to represent the palmprint features. Based on score level fusion and exhaustive searching on all fusion candidates, three feature bands could get much better results than two bands and it can get comparable results with four bands. This finding validates the effectiveness of the proposed clustering algorithm and it is empirically demonstrated that three feature bands is a good option for real multispectral palmprint applications. The finding will be applied to the design of our future multispectral palmprint system.

However, similar as the discussion in Chapter 4, the database is limited by Chinese persons only, whether the finding is applicable to other groups needs further investigation.

Chapter 6. Improvement of CompCode

In the above multispectral palmprint analysis, one of the state-of-the-art palmprint recognition algorithms, CompCode, is used for feature extraction and matching. If the performance of CompCode could be improved, better multispectral recognition is expected.

CompCode with other orientation based methods as shown in Fig. 6.1 has three main issues, including filter design, coding for filtering responses, and distance measure. Many researchers has discussed filter design before, for example, Wu et al. devised a self designed filter (POC) [53], Jia et al. proposed to use Radon transform (RLOC) [54] and Yue et al. investigated the filter orientation effect [141]. In fact, the main difference between these three methods (CompCode, POC and RLOC) lies in the filter design. Compared with filter design, coding of filter response and distance measure is less studied. To address these two issues, a new coding scheme, BOCV is discussed in Section 6.1 and a unified distance measurement is proposed in Section 6.2.

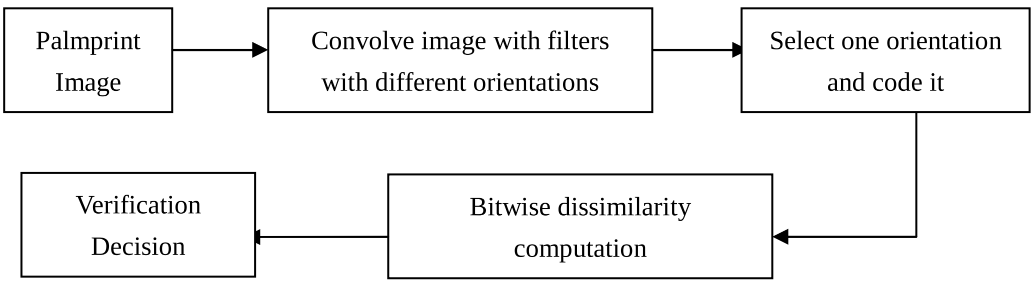

Figure 6.1 Major framework of orientation coding-based palmprint verification algorithm.

6.1 BOCV for Palmprint Verification

Among various coding schemes for palmprint recognition, the orientation based coding methods [52-54] are state-of-the-art ones and they have merits of high accuracy, robustness to illumination variation and fast implementation, etc. Since the orientation of palm lines is stable and can provide enough discriminatory information for personal identification, many palmprint coding schemes, including CompCode [52], POC [53], RLOC[54], were proposed. These algorithms use different filters or masks, such as Gabor filter (CompCode), self designed mask (POC), and modified finite Radon transform (RLOC), to estimate the orientation feature of each local region. A common rule, the “competition” rule, is shared by these algorithms: several filters or masks with different orientation were convolved with the image, and then the “dominant” orientation was determined with some criterion. By simply coding the orientation map of the palmprint, high accuracy palmprint identification could be implemented with high speed matching.

However, the line structures in palmprint image are very complex. Multiple lines may intersect at some regions, so some structural information may be lost if only one orientation is used to represent the local feature. Fig. 6.2a and Fig. 6.2b show an example area where two lines intersect. Fig. 6.2c plots the curve of Gabor filtering response [52] versus orientation for the local area in Fig. 2b. We can see two valleys, which imply two main orientations in this area. If only one orientation is kept, much valuable discriminatory information will be lost.

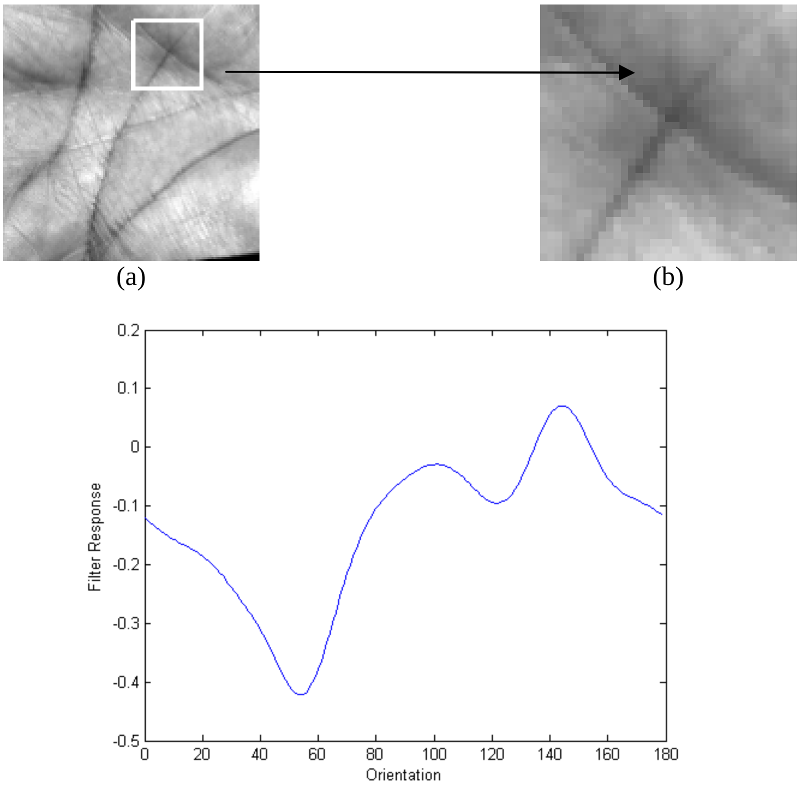

(a) (b)

(c)

Figure 6.2 (a) A palmprint image; (b) cropped and enlarged image with two intersected lines; (c) Gabor filtering responses versus orientation.

In addition, the extracted “dominant” orientation is sensitive to rotation. Fig. 6.3 shows an example. If we rotate Fig. 6.3a only by 5^0 counter-clockwise, the extracted orientation of the local area will change from 120^0 to 90^0, i.e. 30^0 difference.

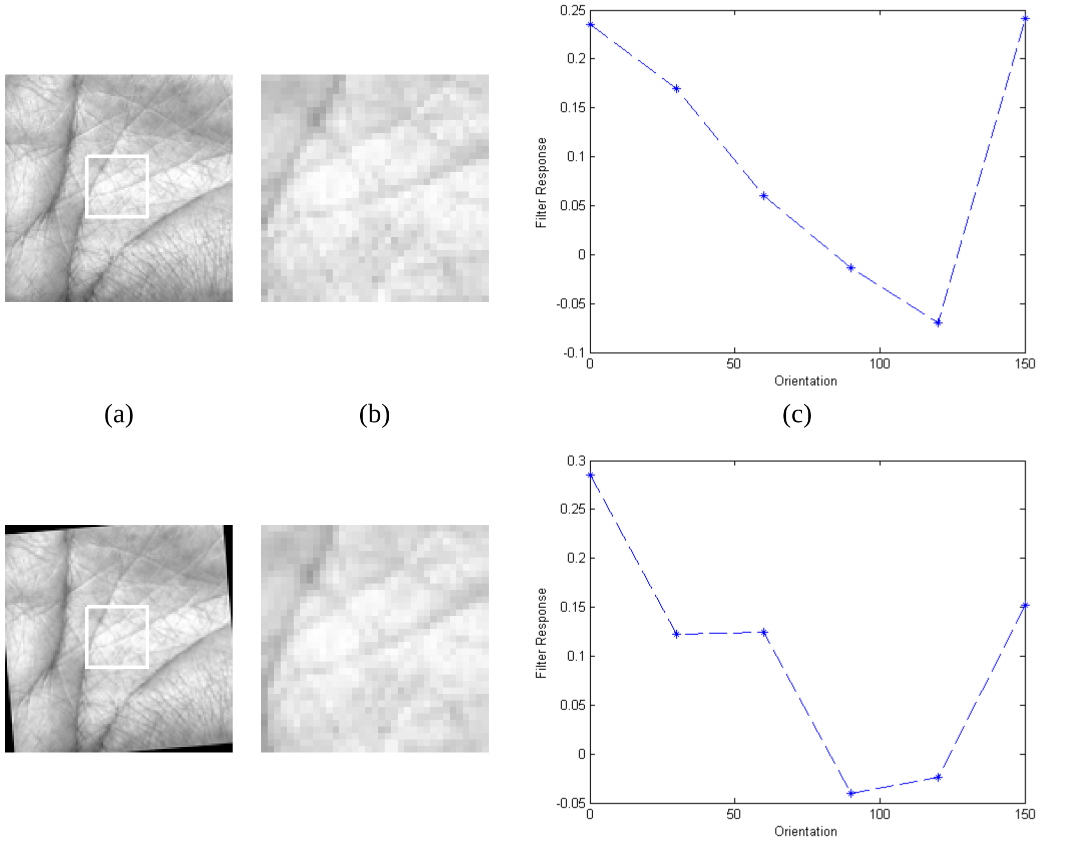

(a) (b) (c)

(d) (e) (f)

Figure 6.3 (a) is a palmprint image and (d) is the 5^0 rotation of it; (b) and (e) are the cropped and enlarged images of (a) and (d); (c) and (f) are the curves of Gabor filtering responses versus six orientations for (b) and (e) respectively.

To circumvent the above problems in traditional orientation coding schemes, a new feature representation algorithm is proposed in this section, namely BOCV. Instead of extracting only one orientation from the filtering responses, all the orientation information is preserved by concatenating the responses as a vector. Then, the response vector is binarized by thresholding. There are two main advantages of BOCV over the traditional orientation based methods. First, the discriminatory ability is enhanced because more line orientation information is preserved. Second, it is more robust to small rotation. Taking Fig. 6.3 as an example, we see that the “dominant” direction is very sensitive to rotation. A 5^0 rotation of the image will lead to a 30^0 change of the dominant direction (from 120^0 to 90^0). However, if all the directions are coded, it is possible that Fig. 6.3c and Fig. 6.3f have the same code. For instance, the Gabor filtering responses above 0 are coded as “0”, and the responses below 0 are coded as “1”. Then the codes for both Fig. 6.3c and Fig. 6.3f are “000110”. They have the same representation after small rotation.

6.1.1 Definition of BOCV

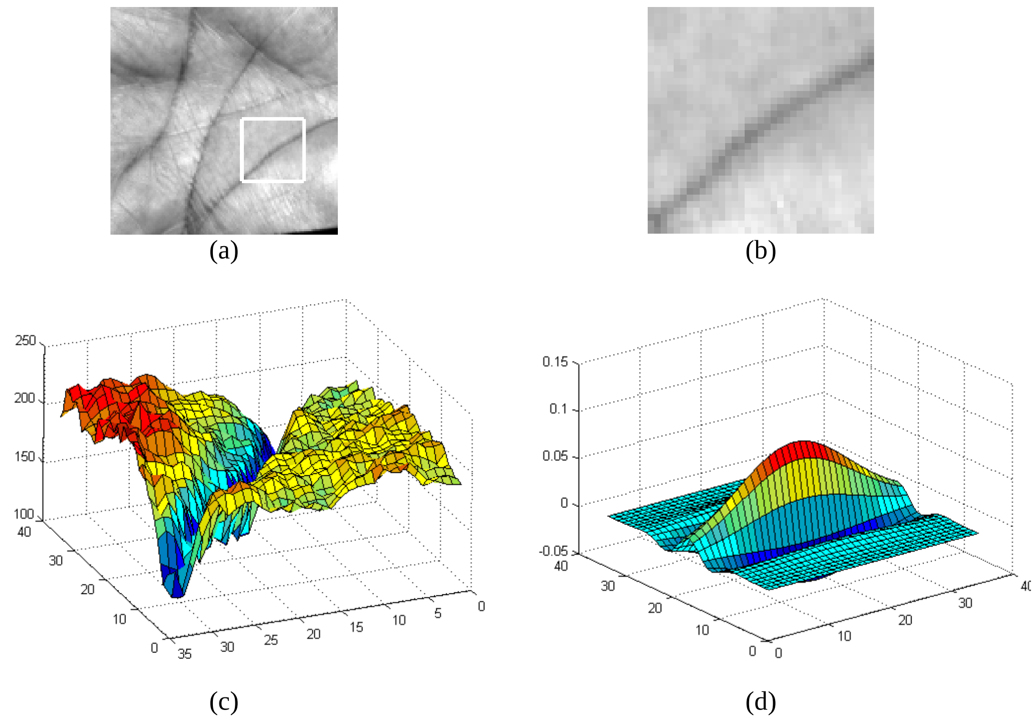

Figure 6.4 (a) A palmprint image; (b) cropped and enlarged image of (a); (c) Intensity value distribution of (b); (d) Gabor filter with θ=0.

Usually, the cross section of palm lines is Guassian-shaped. Fig. 6.4 shows an example of palm line intensity value distribution, while Fig. 6.4d shows the real part of a Gabor filter, which has similar (but upside-down) shape to Fig. 6.4c. The Gabor filter can be regarded as a line detector or matched filter to detect palm lines [142]. If the Gabor filtering response vector is normalized to L_2-norm unity as in Eq. 6.1, the filter response at each orientation can be treated as a confidence measure of the feature occurring at that orientation [143].

$$G_j(x,y)=\frac{G_j^{'}(x,y)}{\sqrt{\sum_{i=0}^{5}G_i^{'}(x,y)^2}} \qquad (6\text{-}1)$$
$$G_j^{'}(x,y)=I(x,y)*\psi_R(x,y,\omega,\theta_j),\theta_j=j\pi/6, j=\{0,1,2,3,4,5\}$$

For each local region, a 6-dimensional vector can be calculated by concatenating the normalized responses along 6 directions, namely the Orientation Co-occurrence Vector (OCV). The distance between two OCVs, P and Q, can be computed by using the L_1-norm:

$$D(P,Q)=\frac{\sum_{y=1}^{M}\sum_{x=1}^{N}\sum_{j=0}^{5}\left|P_j(x,y)-Q_j(x,y)\right|}{M*N} \qquad (6\text{-}2)$$

where P_i and Q_i are the i^{th} dimension planes of P and Q respectively.

However, because the orientation features are represented by float numbers, it is time consuming to use OCV for dissimilarity computation. To speed up the matching time, a 6-bit binarized vector, called BOCV, is defined by thresholding each orientation's filter response:

$$P_j^b(x,y) = \begin{cases} 1, if \ \ G_j'(x,y) < T_j \\ 0, else \end{cases} \tag{6-3}$$

The threshold T_j could be set as 0, which is simple and intuitive but could lead to good results. It can also be chosen according to the filter response distribution which could further improve the accuracy. In this chapter, we set $T_j = 0$, $j = \{0,1,2,3,4,5\}$, as it is intuitive and simple and widely used in palmprint [12, 51] and iris recognition [144]. Fig. 6.5 shows an example of the extracted BOCV.

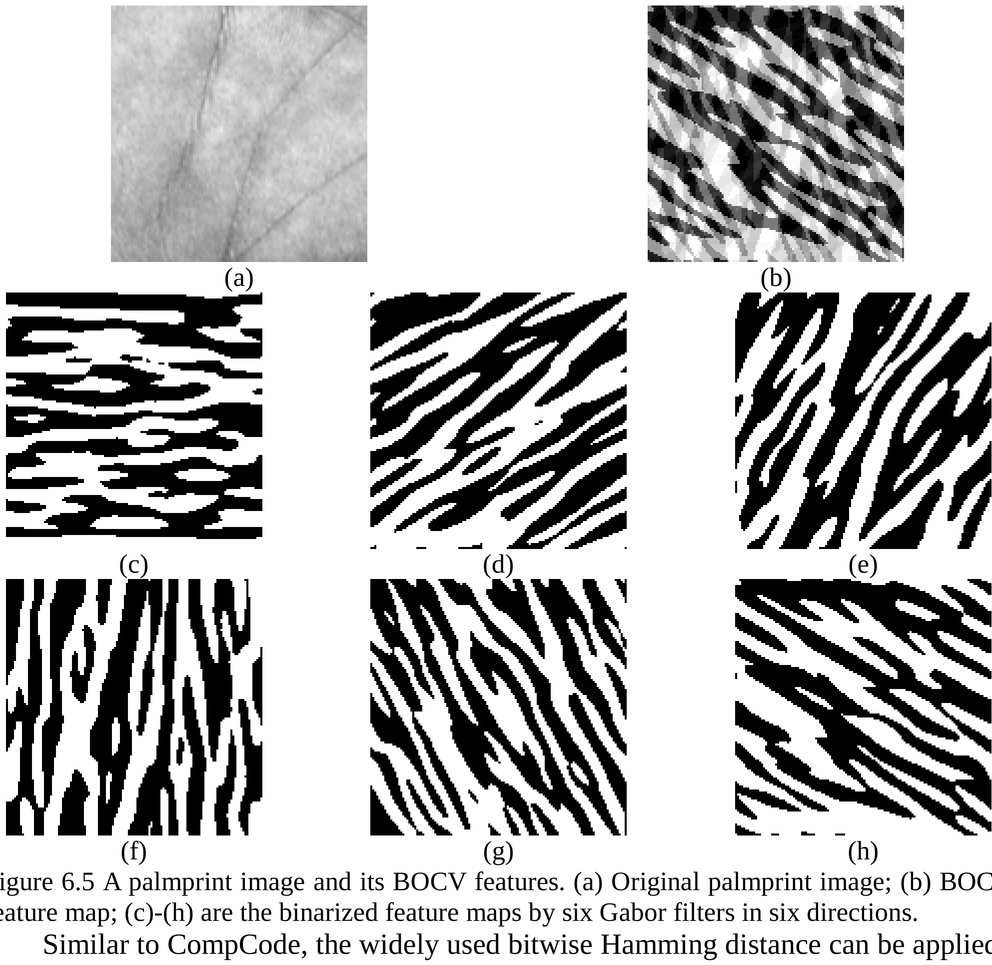

Figure 6.5 A palmprint image and its BOCV features. (a) Original palmprint image; (b) BOCV feature map; (c)-(h) are the binarized feature maps by six Gabor filters in six directions.

Similar to CompCode, the widely used bitwise Hamming distance can be applied to BOCV for matching:

$$D(P^b, Q^b) = \frac{\sum_{y=1}^{M}\sum_{x=1}^{N}\sum_{j=0}^{5}(P_j^b(x,y) \otimes Q_j^b(x,y))}{6 * M * N} \tag{6-4}$$

Obviously, D is between 0 and 1, and for a perfect matching the distance will be 0. In practice, we will shift the BOCV map along different directions in a small range to find the smallest distance between two maps. If the distance is smaller than a certain level, the two palmprints will be classified into the same class.

6.1.2 Experimental Results

6.1.2.1 Experimental Results on PUPD [127]

I) Test Protocol

To compute the verification accuracy in PUPD, each palmprint image is matched with all the other palmprint images in the database. A match is counted as a genuine if the two palmprint images are from the same palm; otherwise, it is counted as an impostor. The total number of matches is 30,042,876 and the number of genuine is 74,068. The EER is used to evaluate the accuracy. And the decidability index d' [144] (the index measures how well the genuine and impostor distributions are separated) is used for reference.

$$d' = \frac{|\mu_1 - \mu_2|}{\sqrt{(\sigma_1^2 + \sigma_2^2)/2}} \tag{6-5}$$

where μ_1 (μ_2) is the mean value of genuine (impostor) and σ_1 (σ_2) is the standard deviation of genuine (impostor) distances.

A ROI extraction procedure similar to that in [12] is used to extract the ROI of size 128*128. To reduce the influence of imperfect ROI extraction, we shift the feature maps vertically and horizontally in a small range for matching. The minimal distance obtained by shift matching is taken as the final distance. The shift range is set as [-4, 4] in the following experiments.

II) Determination of the Number of Gabor Filters

Although those orientation based coding algorithms [52-54] have been widely used, the relationship between the number of employed directional filters (i.e. the number of quantized orientations) and the recognition accuracy has not been well discussed. CompCode [52], POC [53] and RLOC [54] use 6, 4, and 6 filters respectively, but the authors did not clearly show why such numbers were used and whether the number was optimal. Intuitively, using more filters may obtain higher accuracy but increase the computational cost. Thus it is necessary to analyze the determination of the optimal number of filters, which could result in high accuracy and fast implementation. In the following, this issue will be discussed.

First, we use 2, 4, 6, 8, 10, 12, 14 and 16 Gabor filters with π/2, π/4, π/6, π/8, π/10, π/12, π/14 and π/16 interval of $[0,\pi)$ to extract BOCV features and implement verification using bitwise Hamming distance. The computed EER and d' are plotted in Fig. 6.6. We see that the EER is relatively high when the number of Gabor filters is smaller than 6. When the number is bigger than 6, the EER is much lower but fluctuates rather than monotonically decreases with the number of filters. Although d' increases as the number increases, the curve is flat when the number is greater than 6. Thus 6 can be regarded as the optimal number balancing between the accuracy and time consumption. This finding is also in accordance with the neuro-physiological discovery: simple cells are sensitive to specific orientation with approximate bandwidth of π/6 [145].

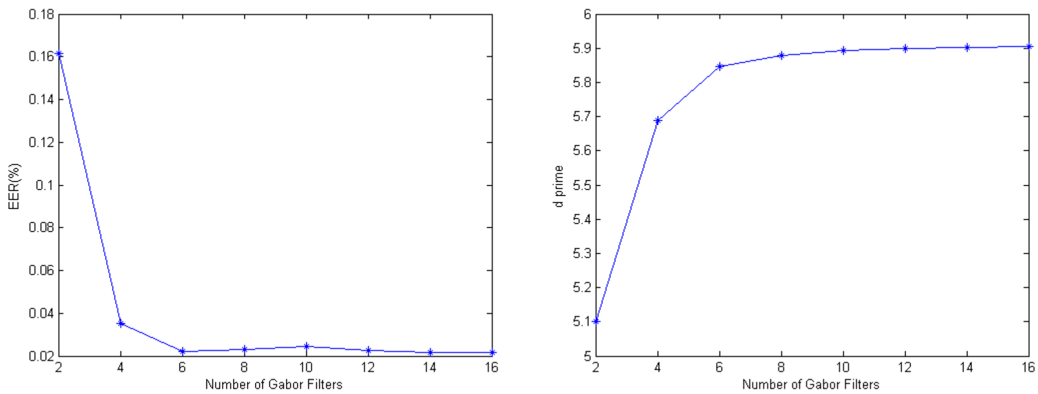

(a) (b)

Figure 6.6 EER and d' of BOCV using different number of Gabor filters. a) EER vs. number of Gabor filters; b) d' vs. number of Gabor filters.

The main reason that why increasing the number of filters could not further reduce the EER is the feature redundancy. To illustrate it, we can calculate the average rate of identical features between adjacent bit planes as follows:

$$Sb(P) = \frac{\sum_{y=1}^{M}\sum_{x=1}^{N}\sum_{i=0}^{n-1} !(P_i^b(x,y) \otimes P_{\mathrm{mod}(i+1,n)}^b(x,y))}{n*M*N} \tag{6-6}$$

where P^b is an extracted BOCV map, $\mathrm{mod}(x,y)$ is the modulus of x divided by y, n is the number of Gabor filters, and "!" is a bitwise NOT operator.

The curve of average rates on the whole database versus the number of Gabor filters is plotted in Fig. 6.7. We can see that as the number of Gabor filters increases, the percentage of identical bits between adjacent planes also increases. Assume that the binary values in each plane follow Bernoulli trials. If two planes are uncorrelated, then the percentage of identical bits should be 50%. However, Fig. 6.7 shows that as the number of Gabor filters increases, the correlation between adjacent bit planes increases, so that using more Gabor filters could not increase much the discriminatory information.

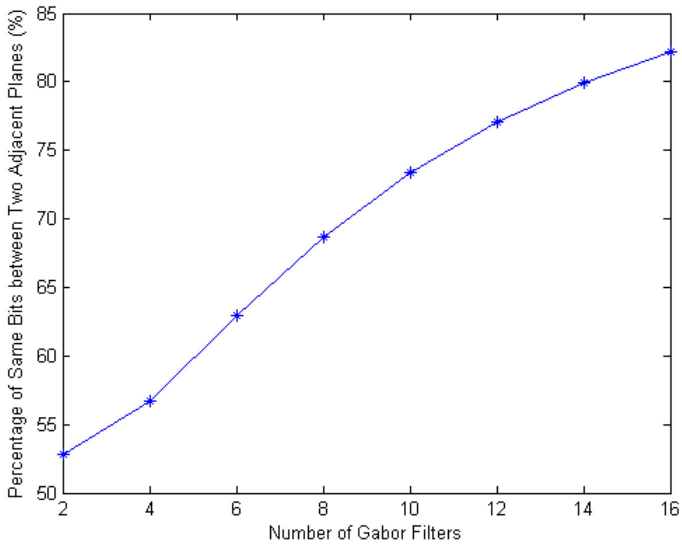

Figure 6.7 Average rate of the identical features between two adjacent planes vs. the number of Gabor filters.

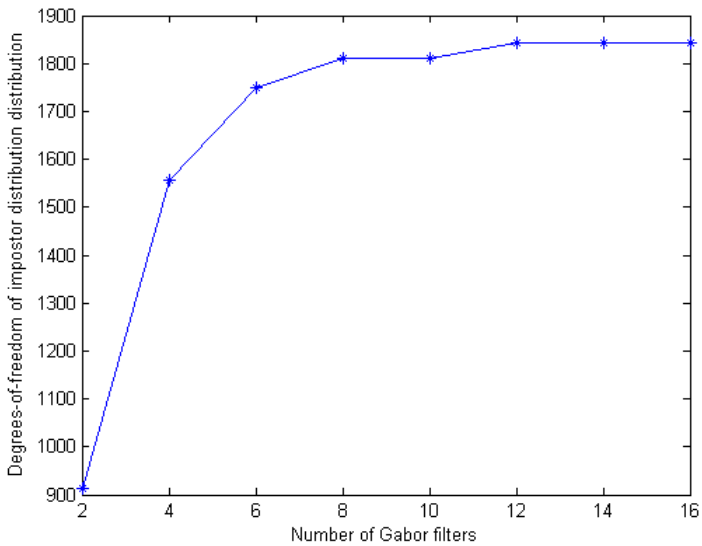

Figure 6.8 Degrees-of-freedom of impostor distance distribution vs. number of Gabor filters.

Assuming the comparison (exclusive OR) between two BOCVs from two different palms follows a Bernoulli trial, the full distribution of impostor distance corresponds to a fractional binomial, whose degrees-of-freedom could be simulated as [144]:

$$N = p(1-p)/\sigma^2 \tag{6-7}$$

where p is the mean of impostor distance distribution, σ is the standard deviation of impostor distance distribution. Fig. 6.8 shows the degrees-of-freedom using different numbers of filters. It shows similar trend to that of d' in Fig. 6.6b. The discriminatory information bits increase rapidly when the number of filters is less than 6, while it increases little when the number is greater than 6. On the other hand, finer quantization may increase the genuine distance due to noise and rotation. Fig. 6.9 shows an example. If six Gabor filters are used, the 6-bit codes of the two ROIs are both 000110. However, if eight filters are used, the 8-bit codes of the two ROIs are 01011110 and 00011110 respectively. Based on the above analysis, in all the experiments in the following, the number of Gabor filters is set as 6.

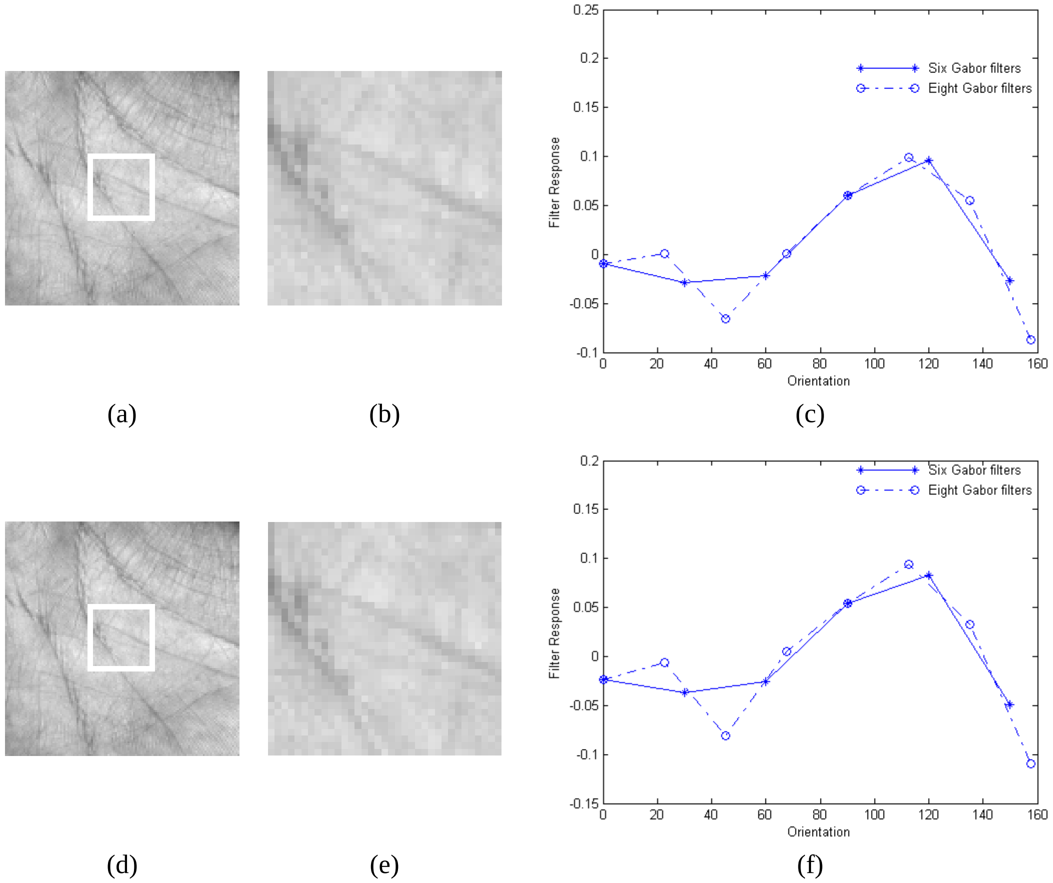

Figure 6.9 An example to show finer quantization may increase genuine distance. (a)-(b) Two ROIs of two sample images from the same palm; (c)-(d) cropped and enlarged images of (a)-(b); (e)-(f) filter responses using six and eight Gabor filters.

III) The Robustness to Rotation

As shown in Fig. 6.3, the extracted “dominant” orientation by CompCode is sensitive to small rotation, while the proposed BOCV scheme is not so sensitive. To further show that BOCV is more robust to rotation than CompCode, two experiments are performed in this section. In the first experiment, we rotate a ROI image by 2^0, 4^0, 6^0, 8^0 and 10^0 clockwise, as shown in Fig. 6.10. The matching distances between the images by CompCode and BOCV are listed in Table 6-1.

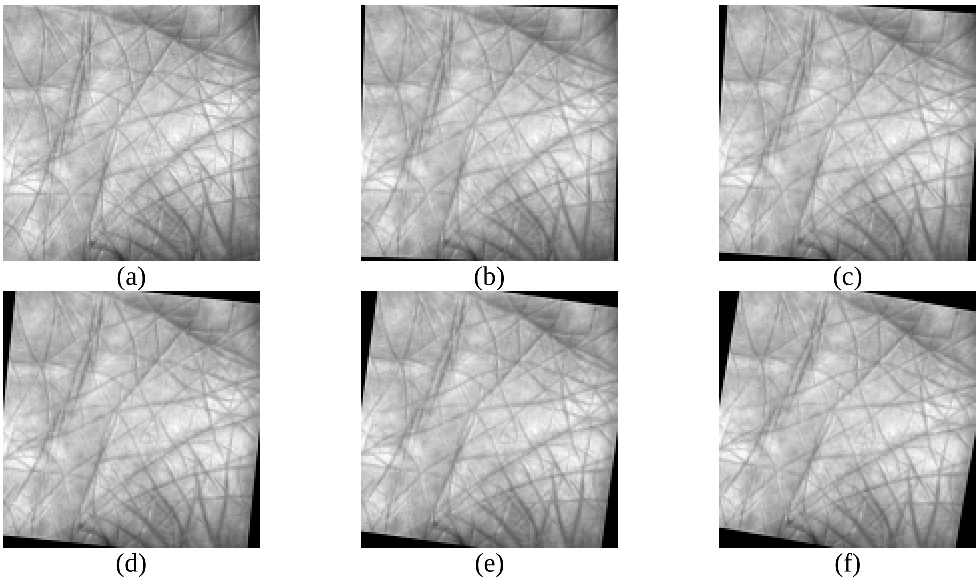

Figure 6.10 An original image and its rotated images. (a) original image; (b)~(f) are the rotated images of (a) by 2^0, 4^0, 6^0, 8^0 and 10^0 clockwise, respectively.

Table 6.1 Matching distances between the images in Fig. 6.10.

CompCode /BOCV	(a)	(b)	(c)	(d)	(e)	(f)
(a)	0	0.1974 /0.1393	0.3337 /0.2635	0.4281 /0.3744	0.4775 /0.4475	0.4959 /0.4858
(b)		0	0.1842 /0.1389	0.3243 /0.2699	0.4155 /0.3688	0.4700 /0.4449
(c)			0	0.1924 /0.1398	0.3379 /0.2560	0.4333 /0.3579
(d)				0	0.1868 /0.1232	0.3465 /0.2493
(e)					0	0.1970 /0.1342

From Table 6-1, we can see that the matching distances by BOCV are smaller than those by CompCode. This validates that BOCV will give more robust recognition results when there are small alignment or registration errors of the palmprint images. To further validate BOCV's robustness to small rotation, another experiment is performed. Each image in the database is rotated randomly by a degree within a range [-d, d], where d={1, 2, 3, 4, 5, 6}. By using the test protocol described in Section 4.1, the calculated EER curves are plotted in Fig. 6.11. We can see that the EER values by BOCV are always lower than those by CompCode at all the rotation degrees.

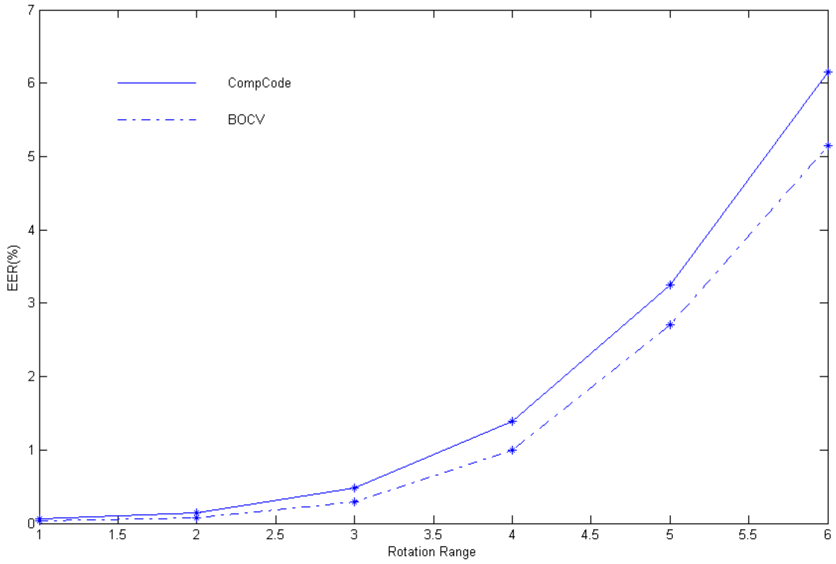

Figure 6.11 EER vs. Rotation by CompCode and BOCV.

IV) Palmprint Verification Result

Fig. 6.12 plots the ROC curves by different methods and Table 6-2 shows the accuracy rates for comparison. Some optimizations have been made on ROI extraction and matching, so the experimental results for RLOC and CompCode are better than the previous publications [52-53]. For POC and RLOC, The original distance for POC [53] and RLOC is used. Because BOCV could keep more directional information than CompCode, POC and RLOC, it could get the best results.

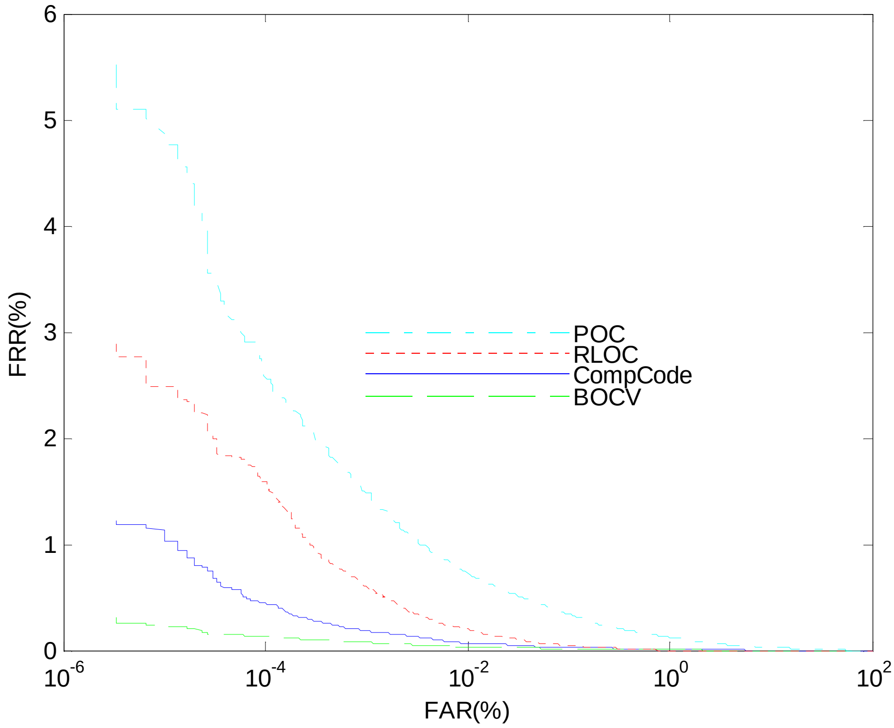

Figure 6.12 ROC curves by different methods for PUPD.

Table 6.2 Verification accuracy by different methods for PUPD.

	EER (%)	d'	FRR (when FAR=3.3x10^{-6}%)
POC	0.2341	3.1053	5.5247
RLOC	0.0593	7.2594	2.8946
CompCode	0.0379	5.4122	1.2273
BOCV	0.0220	5.8477	0.3011

V) Feature Size vs. Speed

In the proposed BOVC, 6 bits are used to represent orientations for each pixel. To speed up matching during verification, the feature is down-sampled to 32*32, thus the feature size is 768bytes in total for one image, twice the CompCode. The system is implemented using Visual C++6.0 on a Windows XP, T6400 CPU (2.13GHz) and 2GB Ram PC. The execution time for ROI extraction, feature extraction and matching is about 138ms, 40ms, and 0.33ms respectively. The total execution time of verification is less than 0.5 seconds, which is fast enough for real-time application. As the speed of matching is fast, it can be easily extended to identification system.

6.1.2.2 Experimental Results on CASIAPD [146]

I) Test Protocol

The same test protocol and matching scheme stated above is used in this section. There were 13,710,466 (2 poor quality images were excluded from our experiment, so the actual number of pictures is 5,237) matches with 20,567 being genuine.

II) Palmprint Verification Result

Table 6.3 lists the verification accuracy and Fig. 6.13 plots the ROC curves. The experimental result is similar as in PUPD. BOCV could get the highest recognition accuracy.

Table 6.3 Verification accuracy by different methods for CASIAPD.

	EER (%)	d'	FRR (when FAR=7.3x10^{-6}%)
POC	0.8547	3.4326	10.4634
RLOC	0.5670	7.2439	3.8411
CompCode	0.5475	5.1873	7.8913
BOCV	0.3891	5.7459	2.7909

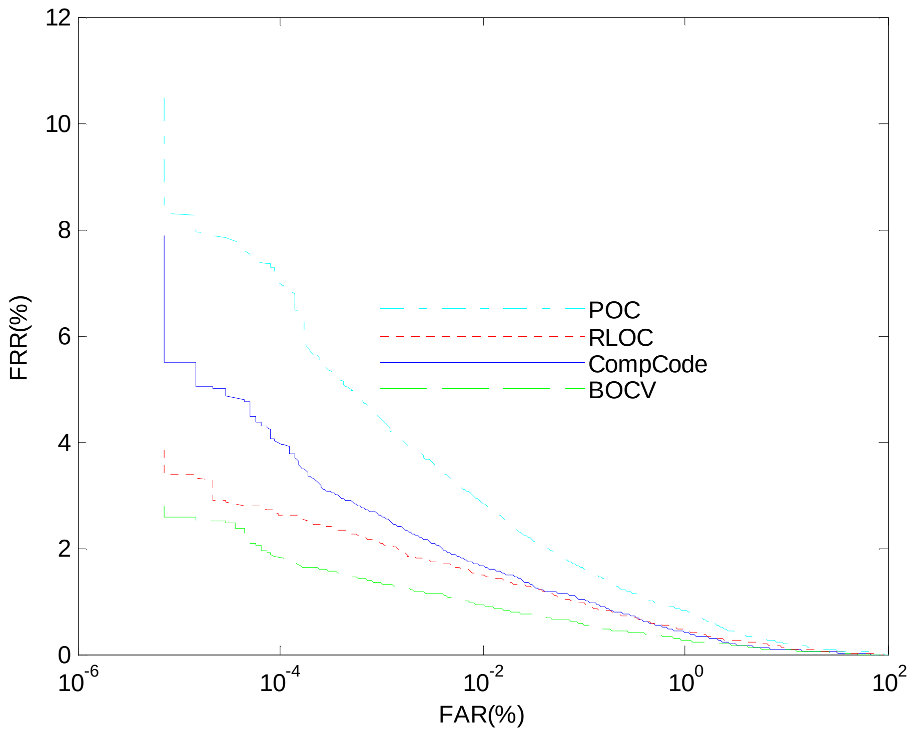

Figure 6.13 ROC curves by different methods for CASIAPD.

6.2 A Unified Distance Measurement for Palmprint Verification

Currently, there are three kinds of orientation based palmprint verification algorithms, including CompCode, POC, and RLOC. CompCode [52] measures the dissimilarity between two features by angular distance (SUM_XOR). POC [53] uses integer Hamming distance, which could be implemented by OR_XOR distance. RLOC [54] compared with OR_XOR distance with a proposed distance, pixel-to-area. SUM_XOR and OR_XOR could be implemented by bitwise operation and thus could achieve fast matching for large scale applications. Although, pixel-to-area could get better results than OR_XOR or SUM_XOR, it is difficult to be implemented by bitwise operation, which may impede its applications. In [147], Kong claimed that the angular distance is superior to the Hamming distance but without any experimental support, little work has been done to date to compare the two distance measures. And even if it does turn out that angular distance has higher verification accuracy than the Hamming distance, it is possible that these two distance measures are complementary and the combination of them would outperform either one of them.

In this section, a unified distance measure is proposed. Then it shows that the angular and the Hamming distance measures (SUM_XOR and OR_XOR) can be regarded as the special cases of the proposed measure. The principles for determining the parameters of the unified distance are also discussed and the experimental results show that the same feature extraction and coding methods using the unified distance measure can achieve lower EER than the original distance measures. It is also empirically validated that OR_XOR could get better results than SUM_XOR in many cases.

6.2.1 The Unified Distance Measurement

6.2.1.1 Review of SUM_XOR and OR_XOR

Orientation code matches using two kinds of distance measure, SUM_XOR (angular distance) and OR_XOR (Hamming distance). In CompCode [19], the angular distance between two features is defined as:

$$D_{SUM\_XOR}(P,Q) = \frac{\sum_{y=0}^{M}\sum_{x=0}^{N}\sum_{i=1}^{3} P_i^b(x,y) \otimes Q_i^b(x,y)}{3*M*N} \tag{6-8}$$

where *P* and *Q* are two CompCode features. P_i^b or Q_i^b is the i^{th} bit plane of *P* or *Q* and $\otimes$ is bitwise exclusive OR (XOR). For each pixel, the angular distance is the sum of the three XOR results on each bit. Thus the angular distance can be called the SUM_XOR distance.

In [53], the distance between two POCs (In CompCode, Kong *et al.* encoded the dominant orientation {0, $\pi/6$, $\pi/3$, $\pi/2$, $2\pi/3$, $5\pi/6$} using 3 bits {000, 001, 011, 111, 110, 100} for efficient palmprint representation and matching. Such a coding could also be used in the POC and RLOC schemes) is defined as follows:

$$D_{Hamming}(P,Q) = \frac{H(P,Q)}{M*N} \tag{6-9}$$

where $H(P, Q)$ is defined as the number of pixels at which the values of *P* and *Q* are different. Using the bit representation as CompCode, the distance could be rewritten as:

$$D_{OR\_XOR}(P,Q) = \frac{\sum_{y=0}^{M}\sum_{x=0}^{N}(P_0^b(x,y)\otimes Q_0^b(x,y))\,|\,(P_1^b(x,y)\otimes Q_1^b(x,y))\,|\,(P_2^b(x,y)\otimes Q_2^b(x,y))}{M*N} \tag{6-10}$$

For each pixel, the distance defined in Eq. 6-10 actually performs the OR operation on the three XOR results on each bit. It is called the OR_XOR distance. RLOR uses a similar distance measure [54].

6.2.1.2 Relation between SUM_XOR and OR_XOR

In the past, research on how to represent palmprint features has attracted a lot of attention, and some work have been done on investigating the relationship between different feature extraction algorithms [55]. In contrast, little such work has been done on the distance measures. SUM_XOR and OR_XOR have been widely adopted for fast matching of orientation codes, while few comparative studies have been made to investigate the difference and relations between them. In [147], Kong claimed that SUM_XOR is superior to OR_XOR but without any experimental evidence. Even SUM_XOR could achieve higher verification accuracy, it is still possible that OR_XOR and SUM_XOR would be complementary and hence the combination of them would outperform any one of them.

Suppose $P(x,y)$ and $Q(x,y)$ are two 3-bit features extracted from the same location of two images. Using the SUM_XOR distance, there are four possible results when we compare $P(x,y)$ with $Q(x,y)$: zero-, one-, two- or three-bit difference. Denote by ***a***, ***b***, ***c*** and ***d*** the numbers of pixels where the zero-, one-, two- and three-bit differences occur, respectively. We define the unified distance between *P* and *Q* is:

$$D_U(P,Q) = \frac{(1+K)*b+(2+K)*c+(3+K)*d}{(3+K)(a+b+c+d)} \tag{6-11}$$

where *K* is a parameter of the unified distance measure.

It can be shown that OR_XOR and SUM_XOR are two special cases of the proposed unified distance measure. The SUM_XOR distance (angular distance) defined in Eq. 6-8 could be written as:

$$D_{SUM\_XOR}(P,Q) = \frac{b+2c+3d}{3(a+b+c+d)} \tag{6-12}$$

Clearly the SUM_XOR distance is a special case of the unified distance with *K*=0. Similarly, the OR_XOR distance defined in Eq. 6-9 could be written as

$$D_{OR\_XOR}(P,Q) = \frac{b+c+d}{a+b+c+d} = \lim_{K\to+\infty} D_U(P,Q) \tag{6-13}$$

Thus, the OR_XOR distance can also be regarded as a special case of the unified distance with *K*=+∞. By adjusting the *K* value, we can get more appropriate weights on ***a***, ***b***, ***c*** and ***d***, and thus expect that the unified distance measure would achieve a higher verification performance.

6.2.1.3 Selection of Parameter *K*

In this section, we discuss some principles to determine the value of parameter K based on the score level fusion theory [94]. OR_XOR and SUM_XOR can be treated as two classifiers. Given two templates P and Q, the outputs of these two classifiers are $D_{SUM\_XOR}(P,Q)$ and $D_{OR\_XOR}(P,Q)$. If we adopt the weighted sum rule to combine the classification outputs $D_{SUM\_XOR}(P,Q)$ and $D_{OR\_XOR}(P,Q)$, the fusing result would be:

$$D_C(P,Q) = D_{SUM\_XOR}(P,Q) + wD_{OR\_XOR}(P,Q) \tag{6-14}$$

where w>0 is the weight on OR_XOR. The fusing result can be given as:

$$D_C(P,Q) = \frac{(1+3w)b + (2+3w)c + (3+3w)d}{3(a+b+c+d)} \tag{6-15}$$

$$D_C(P,Q) = \frac{3+K}{3} D_U(P,Q), \text{ when } K = 3w \tag{6-16}$$

It is obvious that the unified distance measure is a proportional to the weighted sum of OR_XOR and SUM_XOR with $K = 3w$. In real application, the selection of K, like in many other score level fusion [94] techniques, is not a trivial issue. It could be relied on the individual modal's accuracy [134], or be done by using a small portion of the data as training set to tune the parameter [15]. Usually, the weight is strongly related with the data set and the feature map's discrimination. For example, if OR_XOR has better results than SUM_XOR on a given data set, the optimal value of K should be bigger than 3 (w>1); otherwise, it will be smaller than or equal 3 (w<=1).

6.2.1.4 Computational Complexity

The proposed unified distance preserves the fast matching property and could be implemented in bit-wise operation. In this subsection, we compare the computational complexity of OR_XOR, SUM_XOR and the unified distance measure.

Suppose P and Q are of M*N pixels and there are three bits for each pixel. According to Eq. 6-8, SUM_XOR needs 3*M*N times XOR operations and 3*M*N times SUM operations. While OR_XOR in Eq. 6-10 requires the same number of XOR operations, 2*M*N times OR operations and M*N times SUM operations. Usually, the bit-wise operation OR is much faster than integer-wise SUM operation. So OR_XOR is a little faster than SUM_XOR.

For the unified distance measures, Eq. 6-11 could be rewritten as:

$$D_U(P,Q)=\frac{-Ka+b+2c+3d}{(3+K)a+b+c+d}+\frac{K}{3+K}=\frac{D_U^{'}(P,Q)}{3+K}+\frac{K}{3+K} \tag{6-17}$$

$$D_U^{'}(P,Q)=\frac{-K*a+b+2c+3d}{a+b+c+d} \tag{6-18}$$

Since K is a constant value, it will not influence the distance relationship. For example, if $D_U(A,B)>D_U(A,C)$, then $D_U^{'}(A,B)>D_U^{'}(A,C)$. So Eq. 6-17 and Eq. 6-18 could be regarded as the equivalent form for recognition.

Eq. 6-18 could be implemented in bit-wise operation as:

$$\begin{aligned} D_U^{'}(P,Q) &= \frac{-K*a+b+2c+3d}{a+b+c+d} \\ &= \frac{-K*\sum_{y=1}^{M}\sum_{x=1}^{N}(P_0^b(x,y)\otimes Q_0^b(x,y))\,|\,(P_1^b(x,y)\otimes Q_1^b(x,y))\,|\,(P_2^b(x,y)\otimes Q_2^b(x,y))}{M*N} \\ &+ \frac{\sum_{y=1}^{M}\sum_{x=1}^{N}\sum_{i=1}^{3}P_i^b(x,y)\otimes Q_i^b(x,y)}{M*N} \end{aligned} \tag{6-19}$$

It needs 3*M*N times XOR operations, 2*M*N times OR operations and 4*M*N times SUM operations. Though the complexity is little higher than SUM_XOR and OR_XOR, the unified distance measure is still fast enough for real time applications.

6.2.2 Experimental Results

The same test protocol and database as Section 6.1.2 is used in this section. And EER is used for accuracy evaluation.

6.2.2.1 Experimental Results on PUPD

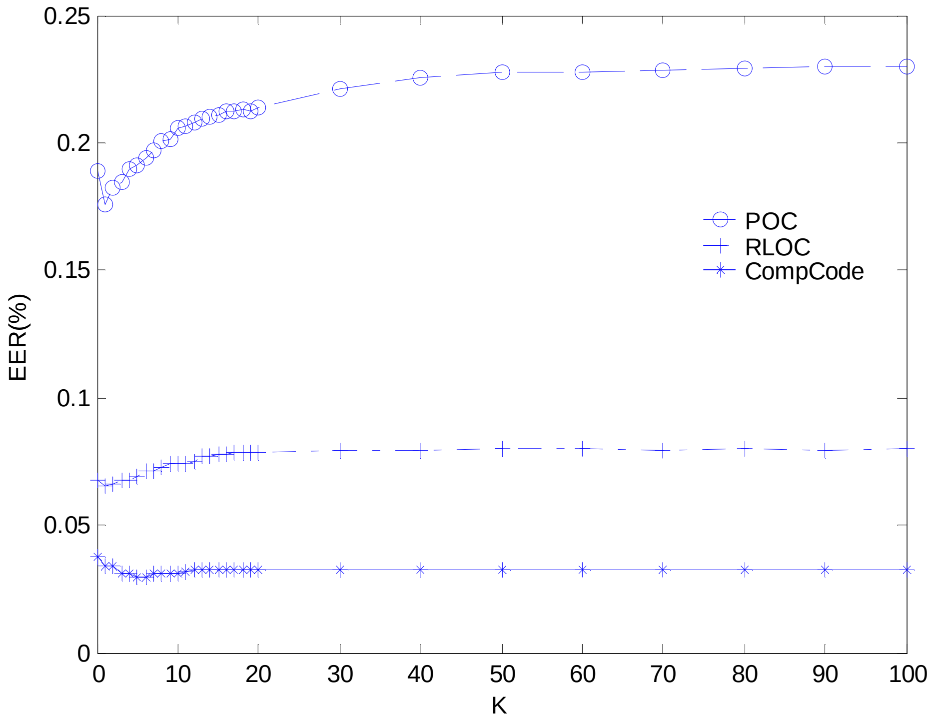

Figure 6.14 EER vs *K* for PUPD.

Fig. 6.14 shows the EERs using different *K* values. As shown in Fig. 6.14, the EER drops to a minimal point when *K* is small, then it increases and gradually stabilizes. This is because OR_XOR and SUM_XOR have different properties. Fusing those increases accuracy when *K* is small but as *K* increases, the accuracy will change gradually to that of OR_XOR. Fig. 6.15 shows an example. Using original SUM_XOR and OR_XOR distance, the same palm images will be wrongly classified because the distance is bigger than that of the different palm images. If we use a different *K* value, it will easy to distinguish the same palm images from different palm images.

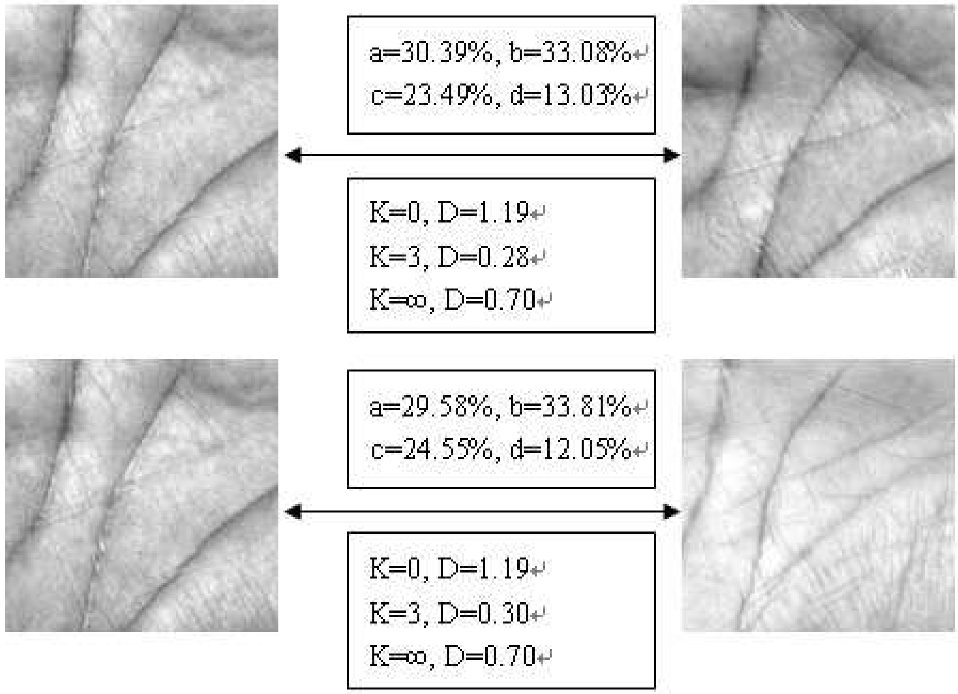

Figure 6.15 The matching results with different *K* values. CompCode is applied on the three images.

Table 6.4 lists part of the EERs with optimal *K* values. Compared with the original distance (Italic number) used in each method, the optimal *K* value (shown in bracket) reduces the EER by up to 22% (0.0379→0.0298), 25% (0.2341→0.1761) and 20% (0.0820→0.0656) for CompCode, POC and RLOC, respectively. There is no a common optimal *K* value for the unified distance. As discussed in Section 6.2.1.3 this value is related to the performance of SUM_XOR and OR_XOR. For example, when EER of SUM_XOR is lower than that of OR_XOR, smaller *K* will get superior results. Negative *K* value will drop the performance significantly, and this is intuitive because bigger ***a*** should occur on genuine more frequently and it plays an important role for discrimination. We also found that in this database, SUM_XOR is better than OR_XOR. This finding is consistent with the claim by Kong [147], i.e. angular distance is superior to Hamming distance.

Table 6.4 Verification accuracy by different methods for PUPD.

EER (%)	CompCode	POC	RLOC
0 (SUM_XOR)	*0.0379*	0.1887	0.0678
Optimal *K*	0.0298 (*K*=5)	0.1761 (*K*=1)	0.0656 (*K*=1)
+∞ (OR_XOR)	0.0325	*0.2341*	*0.0820*

6.2.2.2 Experimental Results on CASIADP

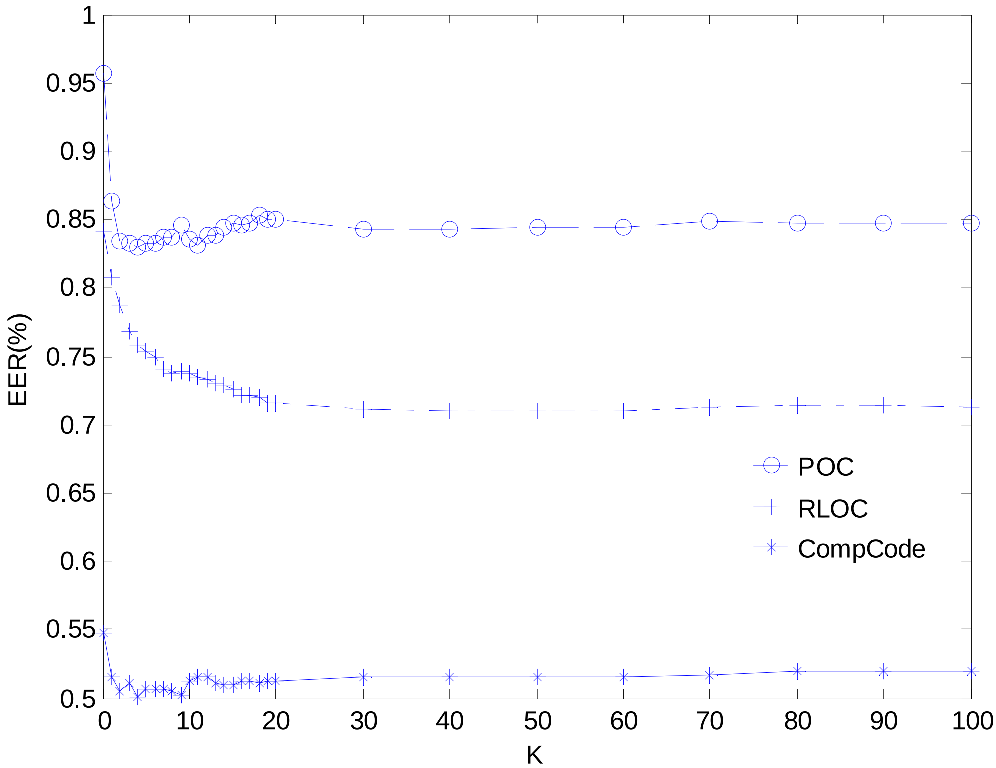

Figure 6.16 EER vs *K* for CASIPD.

Table 6.5 Verification accuracy by different methods for CASIAPD.

EER (%)	CompCode	POC	RLOC
0 (SUM_XOR)	*0.5475*	0.9575	0.8407
Optimal *K*	0.5006 (*K*=4)	0.8294 (*K*=4)	0.7092 (*K*=50)
+∞ (OR_XOR)	0.5190	*0.8547*	*0.7138*

Fig. 6.16 shows the EERs using different *K* value and Table 6.5 lists part of the EERs with optimal *K* values. Similar to Fig. 6.14, the EER drops to a minimal point, and then it increases and gradually stabilizes. The optimal *K* value could reduce the EER compared with original distance metric. Unlike the results in PUPD, OR_XOR gets better results than SUM_XOR for all feature extraction methods. This finding shows that it is hard to draw a conclusion that the angular distance is superior to the Hamming distance.

6.2.2.3 Matching Speed

Table 6.6 shows the matching speed of different distance measures by average execution times. The ordinal relationship is accord with our computational complexity discussion in Section 6.2.1.4. The experiment is implemented using Visual C++6.0 on a PC with Windows XP, E6650 CPU (2.33GHz) and 4GB Ram. Although the proposed unified distance takes a little longer than OR_XOR, it could increase the accuracy and still fast enough for most of applications. For example, for a 1 to10,000 identification comparison, the matching using the proposed distance takes about 0.7 second. Compared with Table 6.2 and Table 6.4, pixel-to-area distance (0.0593%) [54] could get better results than OR_XOR (0.820%) distance for RLOC, which shows the superiority of pixel-to-area distance. However, as shown in Table 6.6, it is very time consuming, about 20 times longer than OR_XOR. Thus it is not applicable for large scale identification applications.

Table 6.6 Average time spending by different methods.

Measure	Average Time (ms)
SUM_XOR (Eq. 6-8)	0.058
OR_XOR (Eq. 6-10)	0.052
Unified distance (Eq. 6-19)	0.070
Pixel-to-area [54]	1.178

6.3 Discussion and Conclusion

A novel feature extraction scheme, BOCV, is proposed for palmprint verification. The BOCV scheme could keep more orientation information for complex palmprint lines and is more robust to small rotations than the conventional CompCode. The relationship between orientation quantization and accuracy is also investigated, and it is found that 6 is an optimal number of orientation quantization in terms of accuracy and complexity. Experimental results demonstrated the effectiveness of this scheme. Using the same Gabor filters as in CompCode, the proposed BOCV could reduce the EER from 0.0379% to 0.0220% for PUPD, and from 0.5475% to 0.3891% for CASIAPD. The proposed BOCV can be extended to other orientation based feature extraction algorithms, such as POC and RLOC.

After analyzing the two distance metrics, a unified distance for orientation-based coding is proposed. The two widely used distance metrics are two special cases of the proposed distance. The proposed distance measure was evaluated on two large public databases. The palmprint verification results showed that the proposed unified distance achieves lower EER than each of the two previously used distances on both databases. It is also empirically found that OR_XOR is not inferior to SUM_XOR but has a faster matching speed. However, OR_XOR has one limitation. It may not be suitable for long binary vector comparison, for example, it can only get 0.0552% EER on PUPD (SUM_XOR achieves 0.0220%) database by BOCV feature. This is because the feature length per pixel of BOCV is 6 bits, which is 2 times longer than CompCode.

The accuracy of CASIAPD is much lower than that of PUPD. This is mainly caused by three reasons. First, the size of the database of CASIAPD is much larger than PUPD, which brings difficulties for classification. Second, there are no pegs to restrict postures and positions of palms during CASIAPD data collection, which brings large degree of freedom. Finally, the image quality of CASIAPD is not as good as that of PUPD. As shown Fig. 6.17, lots of detailed palmprint information is lost in CASIAPD.

(a) (b)

Figure 6.17 (a) A sample palmprint of PUPD [127], and (b) A sample palmprint of CASIAPD [146].

Although OLOF [55] is not designed as an orientation estimator, it can be used to represent a line's orientation like the CompCode does. Suppose there is a straight dark line in a white background as shown in Fig. 6.18a. Fig. 6.18a is rotated counterclockwise by different angles, e.g. from 1 to 180 degree with 1 degree interval (referring to Fig. 6.18b ~ Fig. 6.18f for examples). The associated integer value for CompCode and OLOF are plotted in Fig. 6.19. It can be seen that there is clear correlation between CompCode and OLOF for this simple line image.

(a) (b) (c) (d) (e) (f)

Figure 6.18 An image with a straight line and its rotated image. (a) is the original image and (b)~(f) are the 30, 60, 90, 120 and 150 degree counterclockwise rotated versions of (a).

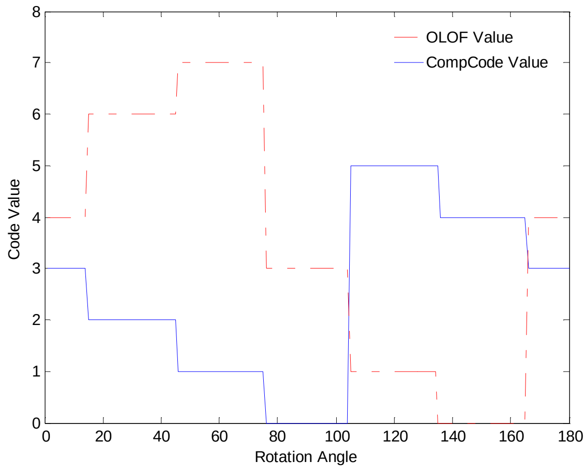

Figure 6.19 Rotation angle vs. Coding value of OLOF and CompCode..

For real palmprint images, however, the structure is much more complex. For example, in a local region, there may be non-straight lines, weak lines and even multiple lines. But there is still weak correlation between OLOF and CompCode [148]. So, OLOF could be regarded as a kind of orientation feature extraction, thus the proposed feature extraction scheme and unified distance measurements could be applicable to OLOF also.

Chapter 7. Conclusion and Future Work

This thesis has studied several aspects of online multispectral palmprint recognition, including the data collection apparatus and three kinds of recognition schemes. Pros and cons of three recognition schemes have been evaluated and it shows that score level fusion is more suitable for high secure orientated applications while image level fusion is fit for high speed applications. Using the developed multispectral palmprint device, palmprint recognition under several lights, including blue, cyan, green, magenta, yellow, red and white, have been empirically studied. Based on a large database and three different kinds of recognition methods, it is empirically shown that the white light may not be the optimal light for palmprint recognition, at least for Chinese people.

Using a hyperspectral palmprint database, the open issue of feature band number selection for multispectral palmprint recognition is studied. A k-means feature band clustering algorithm is proposed to determine the optimal number of feature bands for multispectral palmprint recognition. The experimental results show that 3 bands could convey much of palmprint information.

Original palmprint recognition algorithm is the foundation of multispectral palmprint recognition. If original recognition algorithm is improved, better multispectral palmprint recognition could be expected. The framework of orientation based palmprint recognition is reviewed and two improved algorithms, a new feature representation and a unified matching distance measurement, have been proposed.

In conclusion, the main contributions of this thesis are as follows:

7.1 Main Contributions

- A high speed and accurate multispectral palmprint acquisition device: The device developed is composed of four illuminations: near infrared, blue, green and red. It could collect four palmprint images by these four illuminations in a short time, more specifically, less than one second. Since some pegs are used to restrict the movement of the palm, the registration procedure, which is time consuming, is not required.
- A wavelet based image level fusion was applied on multispectral palmprint recognition: Multispectral palmprint could be regarded as a kind of multimodal biometrics and there are different kinds of fusion methods. Wavelet based image level

fusion is one of the most popular. It is applied on the self built large multispectral palmprint database. Its pros and cons were analyzed and discussed.

- A novel feature level fusion for multispectral palmprint recognition: The new feature level fusion method can represent useful and less redundant features from any two spectra for real time applications. It requires less storage than matching score level fusion while gets comparable results.
- A novel matching score level fusion for multispectral palmprint recognition: In common score level fusion, the relationship between different modals is unexplored. Thus, redundant features may be overemphasized. The proposed score level fusion, derived from set theory, could reduce the overlapping effect and thus get better accuracy.
- Empirically validating whether the white light is the optimal light for palmprint recognition: The white light is the widely used light source for palmprint recognition, although no systematical work is studied. By the proposed multispectral palmprint acquisition and based on the additive color theory, seven palmprint images under blue, green, red, cyan, magenta, yellow and white colors were collected. It is empirically found that the white light is not the optimal light source for palmprint recognition, at least for Chinese people.
- A novel cluster based feature band number selection for multispectral palmprint recognition: Band number selection is an open issue for multispectral palmprint recognition. An optimal feature band number could reduce the device and computation cost. It is the first attempt to address this issue. A large hyperspectral palmprint database was built first. By analyzing the relationship between cluster centers and the number of classes, it is found that 3 bands may be enough for multispectral palmprint recognition. The finding is also validated empirically.
- A novel palmprint feature extraction method: In contrast to selecting one dominant orientation by several filters for a local region, the Binary Orientation Co-occurrence Vector (BOCV) extracts a binary vector to represent information for all orientations. Since more information is kept, BOCV could get better results than the orientation based methods. Furthermore, BOCV is more robust to the rotation effect. The optimal orientation number for BOCV was empirically studied and analyzed.
- A unified distance measurement for orientation based palmprint feature: There are two widely used distances, OR_XOR and SUM_XOR, for orientation based palmprint feature comparison. No work validates which one is more appropriate for palmprint recognition and their relationship is left to be addressed. In the proposed measurement, these two distances are the special cases. Once the parameter in the unified distance is

selected appropriately, the proposed distance could get better results than either distance.

7.2 Future Work

The thesis has studied several issues in palmprint recognition and multispectral palmprint recognition. A few directions could extend current work and improve the accuracy and robustness of palmprint recognition, especially multispectral palmprint recognition:

- Specific multispectral palmprint recognition algorithm: Chapter 3 discusses three kinds of multispectral palmprint recognition methods, however all these algorithms are derived from original palmprint recognition which is dealing with 2D palmprint image only. In the future, we plan to apply methods on multispectral palmprint cube, 3-dimensional data, directly, such as tensor based subspace learning methods [150] and quaternion analysis [151].
- Palmprint recognition on different human groups: Chapter 4 studies the light influence, and finds that different lights may enhance different features and gets different accuracy. However, the samples are limited by Chinese people only, while different group has different skin properties, whether the findings are applicable to other groups needs further exploration and is the future work.
- Feature band selection for different human groups: Chapter 5 selects feature band for multispectral palmprint recognition using hyperspectral palmprint cube. Similar as Chapter 4, the database is built from Chinese people only, so the effectiveness of the selected bands needs further validation on different groups.
- Application of improvement of CompCode on multispectral palmprint recognition: Chapter 6 discusses two directions of improvement over original palmprint recognition. The application of these modifications on multispectral palmprint recognition is our future work.
- Improvement of image level fusion: Chapter 3 investigates the wavelet based image level fusion. However, the experimental results show that application of Haar wavelet is not suitable for multispectral palmprint recognition. In the next stage, we plan to investigate other wavelet bases and other image level fusion techniques for multispectral palmprint recognition.
- Other applications of multispectral palmprint images: As the spectral property of different wavelength is different, some wavelengths have deeper penetration while others enhance skin appearance. These different information could provide a more

comprehensive profile of hand and maybe useful for medical diagnosis, for example, wound status detection [161].

- Liveness detection by multispectral palmprint images: This thesis has shown some samples regarding anti-spoof attacks. However, the sample is limited by printed paper. In the future, we plan to collect more faked palms, including palms made from different materials, and amputation or corpus palms. The analysis on these faked palms will improve the robustness of the system.
- Applications of the proposed feature band clustering: Multispectral imaging has many potential applications in biometrics, including fingerprint, iris, and face. Although there are some works on study multispectral analysis, the underlying feature band selection is paid less attention. We would like to build hyperspectral cube for other biometric traits and apply the proposed algorithm to discover the optimal number of feature bands.

Bibliography

[1] D. Zhang, Palmprint authentication, Kluwer Academic Publishers, Boston, 2004.

[2] M. Cannon, M. Byrne, D. Cotter, P. Sham, C. Larkin and E. O'Callaghan, Further evidence for anomalies in the hand-prints of patients with schizophrenia: a study of secondary creases, *Schizophrenia Research*, vol. 13, pp. 179-184, 1994.

[3] Palmistry, http://en.wikipedia.org/wiki/Palmistry.

[4] Y. Zhou, Y. Zeng, L. Zhen and W. Hu, Application and development of palm print research, *Technology and Health Care*, vol.10, pp. 383-390, 2002.

[5] N. Duta, A. K. Jain and K. V. Mardia, Matching of palmprints, *Pattern Recognition Letters*, vol. 23, pp. 477-485, 2002.

[6] W. Shu and D. Zhang, Automated personal identification by palmprint, *Optical Engineering*, vol. 38, pp. 2359-2362, 1998.

[7] D. Zhang and W. Shu, Two novel characteristics in palmprint verification: datum points invariance and line feature matching, *Pattern Recognition*, vol. 32, pp. 691-702, 1999.

[8] E. Tabassi, C. L. Wilson and G. I. Watson, Fingerprint image quality, NISTIR 7151, 2004.

[9] A. K. Jain and J. Feng, Latent palmprint matching, *IEEE Transactions on Pattern Analysis and Machine Intelligence*, vol. 31, pp. 1032-1047, 2009.

[10] Palm Print Recognition, http://www.biometricscatalog.org/NSTCSubcommittee/Documents/Palm%20Print%20Recognition.pdf

[11] NEC's Automated Palmprint System Identifies Hit and Run Suspect for San Francisco Police Department, http://www.thefreelibrary.com/NEC's+Automated+Palmprint+System+Identifies+Hit+and+Run+Suspect+for...-a077297068

[12] D. Zhang, W. Kong, J. You and M. Wong, Online Palmprint Identification, *IEEE Transactions on Pattern Analysis and Machine Intelligence*, vol. 25, pp. 1041-1050, 2003.

[13] A. Kong, D. Zhang and M. Kamel, A survey of palmprint recognition, *Pattern Recognition*, vol. 42, pp. 1408-1418, 2009.

[14] C. Lin, T. Chuang and K. Fan, Palmprint verification using hierarchical decomposition, *Pattern Recognition*, vol. 38, pp. 2639-2652, 2005.

[15] S. Ribaric and I. Fratric, A biometric identification system based on Eigenpalm and Eigenfinger features, *IEEE Trans. on Pattern Analysis and Machine Intelligence*, 27, pp. 1698-1709, 2005.

[16] T. Connie, A. T. B. Jin, M. G. K. Ong, and D. N. C. Ling, An automated palmprint recognition system, *Image and Vision Computing*, vol. 23, pp. 501-515, 2005.

[17] C. Han, H. Cheng, C. Lin and K. Fan, Personal authentication using palm-print features, *Pattern Recognition*, vol. 36, pp. 371-381, 2003.

[18] S. Ribarić, D. Ribarić and N. Pavešić, Multimodal biometric user-identification system for network-based applications, *IEE Proc.-Vis. Image Signal Process.*, vol. 150, pp. 409-416, 2003.

[19] L. Nanni and A. Lumini, Ensemble of multiple palmprint representation, *Expert Systems with Applications*, vol. 36, pp. 4485-4490, 2009.

[20] X. Pan and Q. Ruan, Palmprint recognition using Gabor feature-based $(2D)^2$PCA,

Neurocomputing, vol. 71, pp. 3032-3036, 2008.
[21] X. Pan and Q. Ruan, Palmprint recognition with improved two-dimensional locality preserving projections, *Image and Vision Computing*, vol. 26, pp. 1261-1268, 2008.
[22] G. K. O. Michael, T. Connie, and A. B. J. Teoh, Touch-less palm print biometrics: novel design and implementation, *Image and Vision Computing*, vol. 26, pp. 1551-1560, 2008.
[23] Y. Han, Z. Sun, F. Wang, and T. Tan, Palmprint recognition under unconstrained scenes, *Asian Conference on Computer Vision*, LNCS 4844, pp. 1-11, 2007.
[24] J. Double, M. Revenu and O. Lepetit, Robust grayscale distribution estimation for contactless palmprint recognition, *First IEEE International Conference on Biometrics: Theory, Applications, and Systems*, pp. 1-6, 2007.
[25] C. Han, A hand-based personal authentication using a coarse-to-fine strategy, *Image and Vision Computing*, vol. 22, pp. 909-918, 2004.
[26] J.-G. Wang, W.-Y. Yau, A. Suwandy and E. Sung, Person recognition by fusing palmprint and palm vein images based on “Laplacianpalm” representation, *Pattern Recognition*, 41, pp. 1514-1527, 2008.
[27] J. Wu, Z. Qiu, and D. Sun, A hierarchical identification method based on improved hand geometry and regional content feature for low-resolution hand images, *Signal Processing*, 88, pp. 1447-1460, 2008.
[28] A. Kumar, D. C.M.Wong, H. Shen, and A. K. Jain, Personal verification using palmprint and hand geometry biometric, *International Conference on Audio- and Video-Based Biometric Person Authentication*, pp. 668–675, 2003.
[29] C. Su, Palm-print recognition by matrix discriminator, *Expert systems with applications*, vol. 36, pp. 10259-10265, 2009
[30] M. K. H. Leung, A. C. M. Fong and S. C. Hui, Palmprint verification for controlling access to shared computing resources, *IEEE Pervasive computing*, vol. 6, pp. 40-47, 2007.
[31] Y. Han, T. Tan, Z. Sun and Y. Hao, Embedded Palmprint Recognition System on Mobile Devices, *International Conference on Biometrics*, LNCS 4642, pp.1184-1193, 2007.
[32] M. Wong, D. Zhang, W.-K. Kong, and G. Lu, Real-time palmprint acquisition system design, *IEE Proc.-Vis. Image Signal Process.*, 152, pp. 527-534, 2005.
[33] W. Li, D. Zhang and Z. Xu, Palmprint identification by Fourier transform, *International Journal of Pattern Recognition and Artificial Intelligence*, vol. 16, pp. 417-432, 2002.
[34] X. Wu, K. Wang and D. Zhang, HMMs based palmprint identification, *International Conference on Biometric Authentication*, LNCS3072, pp. 775-781, 2004.
[35] A. Kumar and D. Zhang, Integrating shape and texture for hand verification, *International Conference on Image and Graphics*, pp. 222-225, 2004.
[36] C. Poon, D. C. M. Wong and H. C. Shen, A new method in locating and segmenting palmprint into region-of-interest, *International Conference on Pattern Recognition*, pp. 533-536, 2004.
[37] W. Zuo, D. Zhang and K. Wang, An assembled matrix distance metric for 2DPCA-based image recognition, *Pattern Recognition Letters*, vol. 26, pp. 210-216, 2006.
[38] J. You, W. Li and D. Zhang, Hierarchical palmprint identification via multiple feature extraction, *Pattern Recognition*, vol. 35, pp. 847-859, 2002.
[39] X. Wu, K. Wang, D. Zhang, Fuzzy directional element energy feature (FDEEF) based palmprint identification, *International Conference on Pattern Recognition*, pp. 95-98, 2002.
[40] X. Wu, D. Zhang and K. Wang, Palm line extraction and matching for personal authentication, *IEEE Transactions on Systems, Man, and Cybernetics - Part A: Systems and Humans*, vol. 36, pp. 978-987, 2006.
[41] F. Li and M. K. H. Leung, Hierarchical identification of palmprint using line-based hough transform, *International Conference on Pattern Recognition*, pp. 149-152, 2006.

[42] Y. Wang and Q. Ruan, Palm-line extraction using steerable filters, *International Conference on Signal Processing*, pp. 16-20, 2006.

[43] X. Wu, K. Wang and D. Zhang, Palmprint recognition using directional line energy feature, *International Conference on Pattern Recognition*, pp. 475-478, 2004.

[44] D. Huang, W. Jia and D. Zhang, Palmprint verification based on principal lines, *Pattern Recognition*, vol. 41, pp. 1316-1328, 2008.

[45] L. Liu, D. Zhang and J. You, Detecting wide lines using isotropic nonlinear filtering, *IEEE Transactions on Image Processing*, vol. 16, pp. 1584-1595, 2007.

[46] L. Liu and D. Zhang, Palm-line detection, *International Conference on Image Processing*, pp. 269-272, 2005.

[47] L. Liu and D. Zhang, a novel palm-line detector, *International Conference on Audio- and Video-based Biometric Person Authentication*, pp. 563-571, 2005.

[48] M. Qi, Y. Lu, H. Li, R. Wang and J. Kong, A novel hand-based personal identification approach, *International Conference on Adaptive and Natural Computing Algorithms*, LNCS 4432, pp. 309-317, 2007.

[49] X. Wu, K. Wang and D. Zhang, A novel approach of palm-line extraction, *International Conference on Image and Graphics*, pp. 230-233, 2004.

[50] J. G. Daugman, High confidence visual recognition of persons by a test of statistical independence, *IEEE Transactions on Pattern Analysis and Machine Intelligence*, vol. 15, pp. 1148-1161, 1993.

[51] A. Kong, D. Zhang and M. Kamel, Palmprint identification using feature-level fusion, *Pattern Recognition*, vol. 39, pp. 478-487, 2006.

[52] A. Kong and D. Zhang, Competitive coding scheme for palmprint verification, *International Conference on Pattern Recognition*, pp. 520-523, 2004.

[53] X. Wu, K. Wang and D. Zhang, Palmprint authentication based on orientation code matching, *International Conference on Audio- and Video-based Biometric Person Authentication*, pp. 555-562, 2005.

[54] W. Jia, D. Huang and D. Zhang, Palmprint verification based on robust line orientation code, *Pattern Recognition*, vol. 41, pp. 1504-1513, 2008.

[55] Z. Sun, T. Tan, Y. Wang and S. Z. Li, Ordinal palmprint representation for personal identification, *IEEE Computer Society Conference on Computer Vision and Pattern Recognition*, pp. 279-284, 2005.

[56] Z. Guo, D. Zhang, L. Zhang and W. Zuo, Palmprint Verification using Binary Orientation Co-occurrence Vector, *Pattern Recognition Letters*, vol. 30, no. 13, pp. 1219-1227, 2009.

[57] X. Wu, K. Wang and D. Zhang, Palmprint texture analysis using derivative of Gaussian filters, *International Conference on Computational Intelligence and Security*, pp. 751-754, 2006.

[58] G. Lu, D. Zhang and K. Wang, Palmprint recognition using eigenpalms features, *Pattern Recognition Letters*, vol. 24, pp. 1463-1467, 2003.

[59] X. Wu, D. Zhang and K. Wang, Fisherpalms based palmprint recognition, *Pattern Recognition Letters*, vol. 24, pp. 2829-2838, 2003.

[60] T. Connie, A. Teoh, M. Goh and D. Ngo, Palmprint recognition with PCA and ICA, *Image and Vision Computing New Zealand*, pp. 227-232, 2003.

[61] D. Hu, G. Feng and Z. Zhou, Two-dimensional locality preserving projections (2DLPP) with its application to palmprint recognition, *Pattern Recognition*, pp. 339-342, 2007.

[62] J. Yang, D. Zhang, J. Yang and B. Niu, Globally maximizing, locally minimizing: unsupervised discriminant projection with applications to face and palm biometrics, *IEEE Transactions on Pattern Analysis and Machine Intelligence*, vol. 29, pp. 650-664, 2007.

[63] Y. Yan and Y. Zhang, Discriminant projection embedding for face and palmprint recognition, *Neurocomputing*, vol. 71, pp. 3534-3543, 2008

[64] J. S. Noh and K. H. Rhee, Eigen palmprint authentication system using dimension reduction of singular vector, *Fuzzy Systems and Knowledge Discovery*, pp. 1169-1177, 2006.

[65] L. Zhang, Q. Gao and D. Zhang, Directional Independent Component Analysis with Tensor Representation, *IEEE Conference on Computer Vision and Pattern Recognition*, pp. 1-7, 2008.

[66] M. Laadjel, A. Bouridance, F. Kurugollu and S. Boussakta, Palmprint recognition using Fisher-Gabor feature extraction, *International Conference on Acoustics, Speech and Signal Processing*, pp. 1709-1712, 2008.

[67] Y. Yao, X. Jing and H. Wong, Face and palmprint feature level fusion for single sample biometrics recognition, *Neurocomputing*, vol. 70, pp. 1582-1586, 2007.

[68] X. Jing, Y. Yao, D. Zhang, J. Yang and M. Li, Face and palmprint pixel level fusion and kernel DCV-RBF classifier for small sample biometric recognition, *Pattern Recognition*, vol. 40, pp. 3209-3224, 2007.

[69] M. Ekinci and M. Aykut, Gabor-based kernel PCA for palmprint recognition, *Electronics Letters*, vol. 43, pp. 1077-1079, 2007.

[70] Z. Zhao, D. Huang and W. Jia, Palmprint recognition with 2DPCA+PCA based on modular neural networks, *Neurocomputing*, vol. 71, pp. 448-454, 2007.

[71] W. Jia, B. Ling, K. Chau and L. Heutte, Palmprint identification using restricted fusion, *Applied Mathematics and Computation*, vol. 205, pp. 927-934, 2008.

[72] W. Jia, D. Huang, D. Tao and D. Zhang, Palmprint identification based on directional representation, *International Conference on Systems, Man and Cybernetics*, pp. 1562-1567, 2008.

[73] M. Aykut and M. Ekinci, Kernel principal component analysis of Gabor features for palmprint recognition, *International Conference on Biometrics*, pp. 685-694, 2009.

[74] A. Uhl and P. Wild, Personal recognition using single-sensor multimodal hand biometrics, *International Conference on Image and Signal Processing*, pp. 396-404, 2008.

[75] A. Kumar and D. Zhang, Personal authentication using multiple palmprint representation, *Pattern Recognition*, vol. 38, pp. 1695-1704, 2005.

[76] X. Wang, H. Gong, H. Zhang, B. Li and Z. Zhuang, Palmprint identification using boosting local binary pattern, *International Conference on Pattern Recognition*, pp. 503-506, 2006.

[77] L. Zhang and D. Zhang, Characterization of palmprint by wavelet signatures via directional context modeling, *IEEE Transactions on Systems, Man, and Cybernetics-Part B: Cybernetics*, vol. 34, pp. 1335-1347, 2004.

[78] J. S. Noh and K. H. Rhee, Palmprint identification algorithm using Hu invariant moments, *Fuzzy Systems and Knowledge Discovery*, pp. 91-94, 2005.

[79] S. Wang and Y. Xu, A new palmprint identification algorithm based on Gabor filter and moment invariant, *IEEE Conference on Cybernetics and Intelligent Systems*, pp. 491-496, 2008.

[80] P. H. Hennings-Yeomans, B. V. K. V. Kumar and M. Savvides, Palmprint classification using multiple advanced correlation filters and palm-specific segmentation, *IEEE Transactions on Information Forensics and Security*, vol. 2, pp. 613-622, 2007.

[81] A. Kumar and D. Zhang, Personal recognition using hand shape and texture, *IEEE Transactions on Image Processing*, vol. 15, pp. 2454-2461, 2007.

[82] X. Pan and Q. Ruan, Palmprint recognition using Gabor-based local invariant features, *Neurocomputing*, vol.72, pp. 2040-2045, 2009.

[83] K. Ito, T. Aoki, H. Nakajima, K. Kobayashi and T. Higuchi, A phase-based palmprint recognition algorithm and its experimental evaluation, *International Symposium on Intelligent Signal Processing and Communications*, pp. 2669-2672, 2006.

[84] X. Yu and M. K. h. Leung, Shape recognition using curve segment Hausdorff distance,

International Conference on Pattern Recognition, pp. 441-444, 2006.

[85] W. Li, J. You and D. Zhang, Texture-based palmprint retrieval using a layered search scheme for personal identification, *IEEE Transactions on Multimedia*, vol. 7, pp. 891-898, 2005.

[86] A. W. K. Kong, Palmprint identification based on generalization of IrisCode, Ph. D Thesis, University of Waterloo, Canada, 2007. http://uwspace.uwaterloo.ca/handle/10012/2708

[87] R.K. Rowe, K. A. Nixon and S. P. Corcoran, Multi spectral Fingerprint Biometrics, *Proceedings of Information Assurance Workshop*, pp.14-20, 2005.

[88] R. Singh, M. Vatsa and A. Noore, Hierarchical fusion of multispectral face images for improved recognition performance, *Information Fusion*, vol. 9, pp. 200-210, 2008.

[89] J. H. Park and M. G. Kang, Multispectral iris authentication system against counterfeit attack using gradient-based image fusion, *Optical Engineering*, vol. 46, pp. 117003-1~117003-14, 2007.

[90] R. K. Rowe, U. Uludag, M. Demirkus, S. Parthasaradhi and A. K. Jain, A Multispectral whole-hand biometric authentication system, *Proceedings of Biometric Symposium, Biometric Consortium Conference*, Baltimore, September 2007.

[91] L. Likforman-Sulem, S. Salicetti, J. Dittmann, J. Ortega-Garcia, N. Pavesic, G. Gluhchev, S. Ribaric and B. Sankur, Final report on the jointly executed research carried out on signature, hand and other modalities, 2007. http://www.cilab.upf.edu/biosecure1/public_docs_deli/BioSecure_Deliverable_D07-4-4_b2.pdf.pdf

[92] Y. Hao, Z. Sun, T. Tan, and C. Ren, Multispectral palm image fusion for accurate contact-free palmprint recognition, *International Conference on Image Processing*, 2008, pp. 281-284.

[93] Y. Hao, Z. Sun and T. Tan, Comparative studies on multispectral palm image fusion for biometrics, Asian Conference on Computer Vision, 2007, pp. 12-21.

[94] A. A. Ross, K. Nadakumar and A. K. Jain, Handbook of Multibiometrics, Springer, 2006.

[95] N. Poh and S. Bengio, How Do Correlation and Variance of Base-Experts Affect Fusion in Biometric Authentication Tasks, *IEEE Transactions on Signal Processing*, vol. 53, pp. 4384-4396, 2005.

[96] X. Wu, D. Zhang, K. Wang and N. Qi, Fusion of palmprint and iris for personal authentication, Advanced Data Mining and Applications, pp. 466-475, 2007.

[97] I. A. Kadadiaris, G. Passalis, G. Toderici, M. N. Murtuza, Y. L. Lu, N. Karampatziakis, and T. Theoharis, Three-dimensional face recognition in the presence of facial expression: an annotated deformable model approach, *IEEE Transactions on Pattern Analysis and Machine Intelligence*, vol. 29, pp. 640-649, 2007.

[98] P. Yan and K. W. Bowyer, Biometric recognition using 3D ear shape, *IEEE Transactions on Pattern Analysis and Machine Intelligence*, vol. 29, pp. 1297-1308, 2007.

[99] S. Malassiotis, N. Aifanti and M. G. Strintzis, Personal authentication using 3D finger geometry, *IEEE Transactions on Information Forensics and Security*, vol. 1, pp. 12-21, 2006.

[100] D. Zhang, G. Lu, W. Li and N. Luo, Person authentication using 3D palmprints, SPIE Newsroom, http://spie.org/documents/Newsroom/Imported/1180/1180-2008-06-16.pdf

[101] D. Zhang, V. Kanhangad, N. Luo and A. Kumar, Robust palmprint verificsation using 2D and 3D features, *Pattern Recognition*, vol. 43, pp. 358-368, 2010.

[102] V. Kanhangad, D. Zhang and L. Nan, A multimodal biometric authentication system based on 2D and 3D palmprint features, *SPIE Biometric Technology for Human Identification V*, vol. 6944, pp. 69440C–69440C-9, 2008.

[103] A. Kong, D. Zhang and M. Kamel, Three measures for secure palmprint

identification, *Pattern Recognition*, vol. 41, pp. 1329-1337, 2008.

[104] A. Kong, K. Cheung, D. Zhang, M. Kamel and J. You, An analysis of BioHashing and its variants, *Pattern Recognition*, vol. 39, pp. 1359-1368, 2006.

[105] A. W. K. Kong, D. Zhang and M. Kamel, Analysis of brute-force break-ins of a palmprint authentication system, *IEEE Transactions on Systems, Man and Cybernetics-Part B: Cybernetics*, vol. 36, pp. 1201-1205, 2006.

[106] T. Connie, A. Teoh, M. Goh and D. Ngo, PalmHashing: a novel approach for cancelable biometrics, *Information Processing Letters*, vol. 93, pp. 1-5, 2005.

[107] X. Wu, D. Zhang and K. Wang, A palmprint cryptosystem, *International Conference on Biometrics*, pp. 1035-1042, 2007.

[108] A. Kumar and A. Kumar, A palmprint-based cryptosystem using double encryption, *Proceeding SPIE*, Vol. 6944, Defense & Security Symposium, pp. 69440D-69440d-9, 2008.

[109] X. Wu, D. Zhang, K. Wang and B. Huang, Palmprint classificaiton using principal lines, *Pattern Recognition*, vol. 37, pp. 1987-1998.

[110] L. Fang, M. K. H. Leung, T. Shikhare, V. Chan and K. F. Choon, Palmprint classification, *IEEE International Conference on Systems, Man and Cybernetics*, pp. 2965-2969, 2006.

[111] A. Jain, R. Bolle and S. Pankanti (eds), Biometrics: Personal Identification in Network Society, Boston: Kluwer Academic, 1999.

[112] D. Zhang, Automated Biometrics - Technologies and Systems, Boston: Kluwer Academic Publishers, 2000.

[113] H. L. Lee and R. E. Gaensslen (ed.), Advances in Fingerprint Technology, Second ed., CRC Press, 2001.

[114] NIST report on the United States Congress, Summary of NIST Standards for Biometric Accuracy, Temper, Resistance, and Interoperability, 2001.

[115] Biometrics, http://en.wikipedia.org/wiki/Biometrics.

[116] W. Zhao, R. Chellappa, P. J. Phillips and A. Rosenfeld, Face recognition: a literature survey, *ACM Computing Surveys*, vol. 35, pp. 399-458, 2003.

[117] J. P. Campbell, Speaker recognition: a tutorial, *Proceedings of the IEEE*, vol. 85, pp. 1437-1462, 1997.

[118] R. Sanchez-Reillo, C. Sanchez-Avila and A. Gonzalez-Marcos, Biometric identification through hand geometry measurements, *IEEE Transactions on Pattern Analysis and Machine Intelligence*, vol. 22, pp. 1168-1671, 2000.

[119] A. K. Jain, A. Ross and S. Prabhakar, An introduction to biometric recognition, *IEEE Transactions on Circuits and Systems for Video Technology*, vol. 14, pp. 4-20, 2004.

[120] L. Zhang, Z. Guo, Z. Wang and D. Zhang, Palmprint verification using complex wavelet transform, *International Conference on Image Processing*, pp.417-420, 2007.

[121] Z. Wang and E. P. Simoncelli, Translation insensitive image similarity in complex wavelet domain, *IEEE International Conference on Acoustics, Speech, & Signal Processing*, pp. 573-576, 2005.

[122] M. P. Sampat, Z. Wang, S. Gupta, A. C. Bovik and M. K. Markey, Complex wavelet structural similarity: A new image similarity index, *IEEE Transactions on Image Processing*, to appear.

[123] D. J. Gawkrodger, Dermatology: An Illustrated Colour Text, 3rd ed., Elsevier Health Sciences, 2002.

[124] V. P. Zharov, S. Ferguson, J. F. Eidt, P. C. Howard, L. M. Fink and M. Waner, Infrared Imaging of Subcutaneous veins, *Lasers in Surgery and Medicine*, vol. 34, pp. 56-61, 2004

[125] G. Pajares and J. M. de la Cruz, A wavelet-based image fusion tutorial, *Pattern Recognition*, vol. 37, pp. 1855-1872.

[126] S. Mallat, A wavelet tour of signal processing, Academic Press, 1999.

[127] PolyU Palmprint Database: http://www.comp.polyu.edu.hk/~biometrics

[128] W. Zuo, F. Yue, K. Wang, and D. Zhang, Multiscale Competitive Code for Efficient Palmprint Recognition, *International Conference on Pattern Recognition*, pp. 1-4, 2008.

[129] Y. Lee and K. Hwang, Skin thickness of Korean adults, *Surgical and Radiologic Anatomy*, vol. 24, pp. 183–189, 2002.

[130] S. A. C. Schukers, Spoofing and anti-spoofing measures, Information Security Technical Report 7(4), pp. 56-62, 2002.

[131] D. Zhang, V. Kanhangad, N. Luo and A. Kumar, Robust palmprint recognition using 2D and 3D features, *Pattern Recognition*, vol. 43, pp. 358-368, 2009.

[132] E. Angelopoulou, The reflectance spectrum of human skin, Technical report, Department of Computer & Information Science, University of Pennsylvania, 1999.

[133] R. C. Gonzalez and P. Wintz, Digital image processing, 2nd Edition, Addison-Wesley Publishing Company, New York, 1987.

[134] R. Snelick, U. Uludag, A. Mink, M. Indovina and A. Jain, Large-scale evaluation of multimodal biometric authentication using state-of-the-art systems, *IEEE Trans. Pattern Analysis and Machine Intelligence*, vol. 27, pp. 450-455, 2005.

[135] L. Liu, Wide line detector and its applications, Ph. D thesis, the Hong Kong Polytechnic University, 2007.

[136] D. Zhang and Z. Zhou, $(2D)^2$PCA: 2-Directional 2-Dimensional PCA for Efficient Face Representation and Recognition, *Neurocomputing*, vol. 69, pp. 224-231, 2005.

[137] W. Zuo, D. Zhang, and K. Wang, Bidirectional PCA With Assembled Matrix Distance Metric for Image Recognition, *IEEE Transactions on Systems, Man, and Cybernetics - Part B: Cybernetics*, vol.36, 2006.

[138] J. Kittler, and M. T. Sadeghi, Physics-based decorrelation of image data for decision level fusion in face verification, *Multiple Classifier Systems*, LNCS 3077, pp. 354-363, 2004.

[139] E. P. Simoncelli, W. T. Freeman, E. H. Adelson, and D. J. Heeger, Shiftable multi-scale transforms, *IEEE Trans Information Theory*, vol. 38, pp. 587–607, 1992.

[140] I. Fratric and S. Ribaric, Colour-based palmprint verification - An experiment, *The 14th IEEE Mediterranean Electrotechnical Conference*, pp. 890-895, 2008.

[141] F. Yue, W. Zuo, D. Zhang and K. Wang, Orientation selection using modified FCM for competitive code-based palmprint recognition, *Pattern Recognition*, vol. 42, pp. 2841-2849, 2009.

[142] J.H. Van Deemter and J.M.H. Du Buf, Simultaneous detection of lines and edges using compound Gabor filters, *Pattern Recognition and Artificial Intelligence*, vol. 14, 757-777, 2000.

[143] M. Varma and A. Zisserman, A statistical approach to texture classification from single images, *International Journal of Computer Vision*, vol. 62, 61-81, 2005.

[144] J. Daugman, The importance of being random: statistical principles of iris recognition, *Pattern Recognition*, vol. 36, 279-291, 2003.

[145] T.S. Lee, Image representation using 2D Gabor wavelet, *IEEE Trans. on Pattern Analysis and Machine Intelligence*, vol. 18, 959-971, 1996.

[146] CASIA Palmprint Image Database V1.0: http://www.cbsr.ia.ac.cn

[147] A. Kong, Pamprint Identification Based on Generalization of IrisCode, Ph.D Thesis, University of Waterloo, 2007.

[148] Z. Guo, W. Zuo, L. Zhang and D. Zhang, Palmprint verification using consistent orientation coding, to appear in *International Conference on Image Processing*, 2009.

[149] D. Tao, X. Li, X. Wu, S. J. Maybank, General tensor discriminant analysis and Gabor features for gait recognition, *IEEE Transactions on Pattern Analysis and Machine Intelligence*, vol. 29, pp. 1700-1715, 2007.

[150] P. Yan and K. W. Bowyer, Ear biometrics using 2D and 3D images, *IEEE Computer Society Conference on Computer Vision and Pattern Recognition, Workshops*, pp. 121-129, 2005.

[151] C. Jones III and A. L. Abbott, Color face recognition by hypercomplex Gabor analysis, *International Conference on Automatic Face and Gesture Recognition*, pp. 126-131, 2006.

[152] C. Boyce, A. Ross, M. Monaco, L. Hornak and X. Li, Multispectral iris analysis: a preliminary study, *IEEE Computer Society Conference on Computer Vision and Pattern Recognition, Workshops*, pp. 51-59, 2006.

[153] H. Chang, Y. Yao, A. Koschan, B. Abidi and M. Abidi, Spectral range selection for face recognition under various illuminations, *International Conference on Image Processing*, pp. 2756-2759, 2008.

[154] B. Guo, S. R. Gunn, R. I. Damper and J. D. B. Nelson, Band selection for hyperspectral image classification using mutual information, *IEEE Geoscience and Remote Sensing Letters*, vol. 3, pp. 522-526, 2006.

[155] H. Wang and E. Angelopoulou, Sensor band selection for multispectral imaging via average normalized information, *Journal of Real-time Image Processing*, vol. 1, pp. 109-121, 2006.

[156] Hyperspectral imaging, Wikipedia, http://en.wikipedia.org/wiki/Hyperspectral_imaging.

[157] C. I. Chang, Hyperspectral imaging: techniques for spectral detection and classification, Kluwer Academic/Plenum Publishers, 2003.

[158] R. O. Duda, P. E. Hart and D. G. Stork, Pattern classification, John Wiley & Sons, 2001.

[159] Visible spectrum, Wikipedia, http://en.wikipedia.org/wiki/Visible_spectrum.

[160] W. Mendenhall, R.J. Beaver & B.M. Beaver, Probability and Statistics, Thomson, Brooks/Cole, 2003.

[161] G. L. Hansen, E. M. Sparrow, J. Y. Kokate, K. Y. Leland and P. A. Laizzo, Wound status using color image processing, IEEE Transactions on Medical Imaging, vol. 16, no.1, pp. 78-96, 1997.

[162] Z. Pan, G. Healey, M. Prasad, and B. Tromberg, Face recognition in hyperspectral images, IEEE Transactions on Pattern Analysis and Machine Intelligence, vol. 25, no. 12, pp. 1552-1560, 2003.

[163] G. Bebis, A. Gyaourova, S. Singh, and I. Pavlidis, Face recognition by fusing thermal infrared and visible imagery, Image and Vision Computing, vol. 24, no. 7, pp. 727-742, 2006.

[164] H. Chang, A. Koschan, B. Abidi, and M. Abidi, Fusing continuous spectral images for face recognition under indoor and outdoor illuminations, Machine vision and applications, vol. 21, no. 2, pp. 201-215, 2008.

[165] D. A. Socolinsky, Multispectral face recognition, Handbook of biometrics, A. K. Jain, P. Flynn, and A. A. Ross eds, pp. 293-314, 2008

[166] H. Chang, Y. Yao, A. Koschan, B. Abidi, and M. Abidi, Improving face recognition via narrowband spectral range selection using Jeffrey divergence, IEEE Transactions on Information Forensics and Security, vol. 4, no.1, pp. 111-122, 2009.

[167] Z. Pan, G. Healey, and B. Tromberg, Hyperspectral face recognition under unknown illumination, Optical Engineering, vol. 46, no. 7, pp. 0772201, 2007.

[168] R. K. Rowe, K. A. Nixon, and P. W. Bulter, Multispectral fingerprint image acquisition, Advances in Biometrics Sensors, Algorithms, and Systems, N. K. Ratha and V. Govindaraju eds., pp. 3-23, 2007.

[169] R. K. Rowe, and K. A. Nixon, Fingerprint enhancement using a multispectral sensor, Proc. SPIE, vol. 5779, pp. 81, 2005.

[170] J. Daugman, Biometric decision landscapes, Technical Report

(UCAM-CL-TR-482), University of Cambridge.